

Michael Kröger

**Device and Process Technology for
Full-Color Active-Matrix OLED Displays**



Cuvillier Verlag Göttingen

Device and Process Technology for Full-Color Active-Matrix OLED Displays

Von der Fakultät für Elektrotechnik, Informationstechnik, Physik
der Technischen Universität Carolo-Wilhelmina zu Braunschweig

zur Erlangung der Würde eines
Doktor-Ingenieurs (Dr.-Ing.)
genehmigte

Dissertation

von
Dipl.-Ing. Michael Kröger
aus Gütersloh

eingereicht am: 08. Mai 2007
mündliche Prüfung am: 24. Mai 2007

Berichterstatter: Prof. Dr.-Ing. W. Kowalsky
Prof. Dr. rer. nat. A. Hangleiter

2007

Bibliografische Information Der Deutschen Bibliothek

Die Deutsche Bibliothek verzeichnet diese Publikation in der Deutschen Nationalbibliografie; detaillierte bibliografische Daten sind im Internet über <http://dnb.ddb.de> abrufbar.

1. Aufl. - Göttingen : Cuvillier, 2007

Zugl.: (TU) Braunschweig, Univ., Diss., 2007

978-3-86727-421-0

© CUVILLIER VERLAG, Göttingen 2007

Nonnenstieg 8, 37075 Göttingen

Telefon: 0551-54724-0

Telefax: 0551-54724-21

www.cuvillier.de

Alle Rechte vorbehalten. Ohne ausdrückliche Genehmigung des Verlages ist es nicht gestattet, das Buch oder Teile daraus auf fotomechanischem Weg (Fotokopie, Mikrokopie) zu vervielfältigen.

1. Auflage, 2007

Gedruckt auf säurefreiem Papier

978-3-86727-421-0

Vorwort

Diese Arbeit entstand während meiner Tätigkeit als wissenschaftlicher Mitarbeiter am Institut für Hochfrequenztechnik an der Technischen Universität Braunschweig. Bevor ich zur Arbeitsgruppe "Hochfrequenz und Photonik" stiess, hatte sich diese schon als Leuchtturm in der deutschen Forschungslandschaft und darüber hinaus etabliert. Meine Neugierde ist in den Jahren wohl auf fruchtbaren Boden gefallen, anders lässt es sich nicht erklären, dass ich dem an Fragestellungen reichen Thema der organischen Halbleiterelektronik und dem akademischen Arbeiten auch in Zukunft weiter verhaftet bin.

Daher gilt mein erster Dank Prof. Dr.-Ing. Wolfgang Kowalsky, Leiter des Instituts für Hochfrequenztechnik, unter dessen Anleitung diese Arbeit entstanden ist, und der für die einmalige technische Ausstattung am Institut verantwortlich gemacht werden muß. Er ließ mich durch eigenverantwortliches wissenschaftliches Arbeiten Selbstvertrauen in die eigenen Fähigkeiten entwickeln, um zugleich bei Problemen ausserhalb meines Horizonts hilfreich einzugreifen.

Ebenso möchte ich mich bei Prof. Dr. rer. nat. Andreas Hangleiter, Leiter des Instituts für Angewandte Physik, bedanken, dass er sich kurzfristig dazu bereit erklärt hat, dem Zweitgutachten für diese Arbeit höchste Priorität einzuräumen. Weiter schulde ich Prof. Dr. rer. nat. Achim Enders, Leiter des Instituts für Elektromagnetische Verträglichkeit, meinen Dank, der trotz eines vollen Terminkalenders Zeit fand, den Prüfungsvorsitz und die damit verbundenen Verpflichtungen zu übernehmen.

Zu besonderem Dank verpflichtet bin ich meinem Gruppenleiter Dr. rer. nat. Hans-Hermann Johannes, der mit zwei Büros und mehreren tausend Kilometern Dienstweg zwischen Campus Nord und Schleinitzstrasse einen großen Anteil an dem kollegialen und produktiven Miteinander innerhalb seiner Arbeitsgruppe hat, und in fast allen Lagen aufmunternde Worte findet.

Ein herzliches Danke möchte ich auch den Projektpartnern "meiner" BMBF-Projekte widmen. Hervorzuheben sind Dr.-Ing. Uwe Hoffmann und Dr. rer. nat. Marcus Bender der Applied Materials GmbH in Alzenau sowie Dr.-Ing. Marc Hüske der LPKF Laser & Electronics AG in Garbsen für die ständige Bereitschaft, mir im Bereich "unglaublich grosse Vakuum-Beschichtungsanlagen" beziehungsweise "unglaublich schnelle und präzise Lasertechnik" und die für meine Arbeit implizierten Fragestellungen weiter zu helfen. Ebenso wurde so manches Projekttreffen erst durch Gespräche fernab vom Geschäftlichen mit Sinn beladen.

Viele der von mir präsentierten Ergebnisse wären ohne die Mithilfe der ehemaligen Studenten Sami Hamwi, Matthias Haupt, Thomas Reichenbacher, Atef Saanouni, Stephan Schmale, Mohammed Ihab Schukfeh und Florian Werner nicht erzielt worden. Stephan möchte ich

ausserdem als langjährigen und sehr zuverlässige studentischen Mitarbeiter bei zahlreichen Projekten besonders danken. Sami hat durch sein Geschick und seine Experimentierfreude wesentlich zum Verständnis der Ladungsträgerseparation in dotierten organischen Halbleitern beigetragen.

Da ich weder genug Feinmotorik noch den Sachverstand besaß, um die für meine Arbeit notwendigen mechanischen Komponenten selbst zu fertigen, konnte ich mich nur glücklich schätzen, in den Mitarbeitern der feinmechanischen Werkstatt Bernhard Brandmeyer, Frank Denecke, Olaf Flechtner, Jürgen Härtlein, Rick Papies und Niels Peikert kompetente Ansprechpartner zu finden, welche meine technischen Zeichnungen regelmässig in Edelstahl, Aluminium und Kupfer meisselten. Olaf wünsche ich auf diesem Weg zu Wasser, zu Rad und zu Fuß weiterhin regelmässig Bestzeiten.

Mein ausgesprochener Dank gilt Diane Lack, die mit unermüdlichem Einsatz unzählige ITO-Proben hergestellt und charakterisiert hat. Diane setzt Standards in der Substratpräparation, was jedem schmerzlich bewußt wird, der während ihres wohlverdienten Urlaubs zum dilettieren gezwungen ist. In diesem Zusammenhang möchte ich auch Ursula Heydecke nennen, die nicht nur die Konstante in jeder Gleichung am Institut für Hochfrequenztechnik - Kaffee und Tee gibt es täglich nach Voranmeldung von 15:30 bis 16:00 in Ihrem Sozialraum genannten Vorzimmer - ist, sondern mit Hunderten von Leitfähigkeitsmessungen auch Ihren Anteil an dieser Arbeit hat und mir sicherlich verzeiht, dass ich den einen Ölwechsel immer schuldig geblieben bin.

Da ich "Ullas Kaffeerrunde" schon angesprochen habe, möchte ich darüber hinaus das kollegiale Miteinander am Institut loben. Mir werden unzählige Anekdoten aus den letzten Jahren, sei es der Staffelmarchathon, das "Derby", durchzockte Nächte und Wochenenden oder gesellige ;-) Junggesellenabschiede, in lebhafter Erinnerung bleiben. Marc, Sören, Kai, Lars, Matthias, Artur, Norman, Eike, Thomas, Patrik: Ich hoffe, ich konnte meinen Teil dazu beitragen.

Selten promoviert es sich allein. Meine Dissertation beinhaltet daher auch Anregungen und Ideen meiner Büro- und Laborgenossen. Namentlich erwähnen möchte ich Hendrik Blei, der entscheidend zur Entwicklung des laser-induzierten lokalen Transfers beigetragen hat und der immer für ein "Almond" zu haben war. Jens Meyer hat sich inzwischen als dritter "Invertierter" etabliert. Ohne seine Mithilfe wäre meine Dissertation um mindestens ein Kapitel, und ich um viele persönliche Erfahrungen ärmer. Letzten beiden sowie Steffen Mozer sei an dieser Stelle für die rasche Korrektur der Rohfassung gedankt. Gedankt sei ausserdem Torsten Rabe. Sei es, ob wir zusammen als Diplomanden an die OMBD genagelt wurden, am selben Tag angefangen haben, oder trotz verschiedener Themen die gleichen

Erfahrungen gemacht haben, sicher ist, dass die gemeinsame Zeit am IHF mir in guter Erinnerung bleiben wird. Als letztem im Kreise meiner Arbeitskollegen danke ich Thomas Dobbertin, der fachlich als grosses Vorbild vorangegangen ist. Danke für Dein Vertrauen, Deine Ehrlichkeit und dass ich in jeder Lage auf Dich zählen konnte. Ich bin dankbar, Dich meinen Freund nennen zu dürfen.

Meine Eltern haben mich in all den Jahren mehr als nur finanziell unterstützt: Sie haben mir die Freiheit gelassen, mir meinen Weg selbst zu suchen anstatt ihn mir vorzuzeichnen, und die Sicherheit gegeben, die ich benötigte, um rasch voranzuschreiten. Es ist schwer, angemessene Worte dafür zu finden.

Abschließend möchte ich mich bei meiner Frau Silke, die viele Selbstzweifel und Launen gerade zum Ende der Promotion mit viel gutem Willen ertragen, mit Verzicht auf gemeinsame Zeit bezahlt und mich trotzdem geheiratet hat. Ein bisschen verrückt musst Du schon sein. Ich hoffe, Du bleibst so!

Braunschweig, Mai 2007

Michael Kröger

Kurzfassung

Organische Leuchtdioden (engl.: organic light emitting diode, OLED) faszinieren durch spezielle Eigenschaften, wie z.B. eine extrem flache Bauweise, eine weite Abstrahlcharakteristik und einen geringen Energieverbrauch. Dies macht die OLED Technologie für eine potenzielle Nutzung im Bereich hochwertiger Anzeigelemente interessant. Für niedrigauflösende Kleinanzeigen, wie sie in Mobiltelefonen zum Einsatz kommen, werden OLED-Anzeigen bereits heutzutage verwendet. Um im Bereich hochauflösender großformatiger Bildschirme mit den etablierten Technologien (LCD, PDP) konkurrieren zu können, müssen aktive Treiberelemente in die Bildschirmfläche integriert werden. Solche Aktiv-Matrix-Schaltungen sind in der Regel opak und verlangen daher nach einer Lichtauskopplung durch den Deckkontakt. An diesem Punkt setzt die Entwicklung invertierter organischer Leuchtdioden (IOLEDs) an. Der Begriff "invertiert" spielt in diesem Zusammenhang auf eine im - Vergleich zu historisch gesehen konventionellen OLEDs - inverse Depositionsreihenfolge an. Die Skalierung der im Forschungsbetrieb verwendeten Abscheideprozesse auf im Produktionsbetrieb verwendbare Prozesse stellt weitere Herausforderungen auf dem Weg zu kommerziellen vollfarbigen AM-OLED-Anzeigen. Im Fokus der vorliegenden Arbeit steht daher die Realisierung effizienter invertierter OLEDs und die Entwicklung skalierbarer Depositions- und Strukturierungsprozesse.

Durch den Einsatz von hocheffizienten phosphoreszenten Emittersystemen kann der Wirkungsgrad von invertierten OLEDs deutlich gesteigert werden. Dies setzt voraus, dass Löschungsprozesse, welche durch thermische Rekristallisation, strahlungslosen Energietransfer in Nähe der Kathode oder nicht-strahlende Umwandlung von angeregten Grenzflächenzuständen ausgelöst werden, mittels einer optimierten Bauteilarchitektur minimiert werden. Unter Verwendung von elektrisch dotierten Injektionsschichten werden maximale Effizienzen von 59 cd/A und 21 lm/W sowie eine maximale Leuchtdichte von mehr als 100.000 cd/m² erzielt. Die Verkopplung mehrerer Emissionsschichten durch Ladungsträger-erzeugende Zwischenschichten (engl.: charge generation layer, CGL) ermöglicht eine weitere Steigerung der photometrischen Effizienz (invertierter) organischer Leuchtdioden auf bis zu 92 cd/A. Effektive CGL-Strukturen haben die Form 1-TNATA:F₄-TCNQ/BPhen:Li mit jeweils mindestens 5 nm Schichtdicke. Der Mechanismus der Ladungsträgerseparation wird mittels eines Tunnelmodells erklärt.

Da die transparente Anode in invertierten OLEDs auf die bereits deponierten organischen Schichten mittels Kathodenzerstäubung (engl.: Sputtering) abgeschieden wird, geschieht dies bei Raumtemperatur und geringen Leistungsdichten, um einer Schädigung der organischen Materialien vorzubeugen. Wenn ein geringer Sauerstoff-Anteil der Sputteratmosphäre hinzu gegeben wird, kann eine elektrische Leitfähigkeit von ca. 2300 S/cm bei einer op-

tischen Transparenz von mehr als 85 % erzielt werden. Um die Abscheidung von dotierten Emissionsfilmen in einer produktionsnahen Inline-Anlage zu ermöglichen, wird eine prototypische lineare Koverdampfungszelle eingesetzt. Dabei ist es möglich die Verdampfungskeulen zweier Materialien auf einer Achse ideal zu überlagern. Über einer beschichteten Fläche von 100 mm mal 120 mm beträgt die Schichtdickenhomogenität für beide Materialien nahezu $\pm 5\%$ vom Mittelwert. Die üblicherweise verwendete Strukturierung organischer Dünnsfilme mittels Schattenmasken genügt den Genauigkeitsanforderungen mit zunehmender Maskengröße immer weniger. Als mögliches Strukturierungsverfahren für große Substrate wird der laser-induzierte lokale Transfer (LIL) vorgestellt. Die Abhängigkeit der erzielten Strukturgrößen von den Prozessparametern wird mittels einer analytischen Näherung beschrieben. Es werden minimale Strukturabmessungen von ca. $60\text{ }\mu\text{m}$ erreicht.

Abstract

Organic light emitting diodes fascinate due to unique properties like an extremely thin design, wide viewing angle and low energy consumption. For these reasons, OLED technology appears to be a promising technology for high-end display units. Today, organic light emitting diodes are already applied for low resolution applications as - for instance - mobile phone and automotive sub-displays. For being a serious competitor in the high-resolution large-area display market, active-matrix driving circuits have to be integrated onto the display substrate. Since the circuitry is most likely to be opaque, the light has to be emitted rather from the top than through the substrate. This is, where inverted organic light emitting diodes step into the spotlight. The term "inverted" refers to a reversed deposition sequence compared to conventional bottom-emitting OLEDs. Up-scaling of laboratory deposition processes to high-volume production means further challenges on the way to commercial full-color AM-OLED displays. The present study focuses on the realization of highly efficient IOLEDs and the development of scalable deposition and patterning processes.

Utilizing highly phosphorescent emitter materials boosts the efficiency of inverted IOLEDs. As a precondition, luminescence quenching via thermal recrystallization of the host material, energy transfer to image dipoles on the cathode's surface or radiationless decay of interfacial exciplexes has to be minimized by an optimized device structure. Combining this optimized device structure with doped charge injection layers yields superb efficiencies of 59 cd/A and 21 lm/W as well as a maximum brightness of more than 100000 cd/m². Coupling of several emission units by so called charge generation layers (CGL) enables a further increase of the current efficiency. An inverted OLED with two EMUs reaches a current efficiency of up to 92 cd/A. Effective CGL-structures are made of a pn-heterojunction of at least 5 nm thick 1-TNATA:F₄-TCNQ/BPhen:Li layers. The mechanism is explained by tunneling of electrons through a narrow depletion zone at the pn-interface.

Sputtering of ITO on top of the sensitive organic layers is performed at room temperature and low intensity to prevent from sputter induced damage of the organic layers. When mixing a small fraction of oxygen into the argon sputtering atmosphere, an electric conductivity of about 2300 S/cm and an optical transparency of 85 % can be achieved. For enabling the deposition of phosphor-doped emission layers within an inline system, a prototype co-evaporation source is used. As the outlet hole for both materials are aligned on a common axis, ideal superposition of the sublimation beams is possible. The thickness uniformity across a 100 x 120 mm² large substrate was nearly $\pm 5\%$ of the average. So far, micropatterning of organic materials was performed by shadow masking, which is certainly limited to medium substrate sizes. The laser induced local transfer (LILT) is presented as possible

patterning technology for large substrate sizes. The dependence of the pattern resolution on the process parameters is given by an approximated model description. Minimum feature sizes of about $60\text{ }\mu\text{m}$ are achieved.

Contents

1. Introduction	1
1.1. organic light emitting diodes	1
1.2. OLED-displays	2
1.2.1. passive-matrix OLED displays	2
1.2.2. active-matrix OLED displays	3
1.2.3. production issues	5
1.3. goals and outline of this study	5
2. Charge injection, transport and recombination	7
2.1. π -conjugated small molecules	7
2.2. charge transport	9
2.3. charge injection	13
2.3.1. interface engineering	14
2.3.2. doped charge transport layers	18
2.4. luminescent properties of organic dyes	20
2.4.1. photoexcitation	20
2.4.2. charge carrier recombination	22
3. Device preparation and characterization	25
3.1. device preparation	25
3.2. electro-optical characterization	27
4. Phosphorescent IOLEDs	29
4.1. deposition induced luminescence quenching in phosphorescent IOLEDs	29
4.2. cathode-induced quenching in phosphorescent IOLEDs	32
4.3. multicolor IOLED stack	34
4.4. influence of interfacial exciplex states	38
4.5. highly efficient IOLEDs with doped injection layers	41
5. The stacking approach	44
5.1. stacked organic light emitting diodes	45

5.2.	field-induced charge separation at doped organic/organic heterointerfaces . .	46
5.2.1.	doping profile	47
5.2.2.	low temperatures	48
5.2.3.	thickness dependence	49
5.2.4.	Kelvin Probe measurements	52
5.2.5.	energy level alignment	54
5.3.	stacked inverted organic light emitting diodes	56
6.	Advanced process technology	59
6.1.	inline system for sputtering of indium tin oxide	59
6.1.1.	ITO sputtering onto organic thin films	62
6.1.2.	inline sputtering system: setup	63
6.1.3.	dependence of electrical and optical properties on plasma excitation and oxygen flow	64
6.2.	linear co-evaporation source for organic materials	68
6.2.1.	concept	68
6.2.2.	thickness and doping profile	71
6.3.	micropatterning of organic materials	74
6.3.1.	laser induced local transfer - LILT	75
6.3.2.	LILT - experimental setup	76
6.3.3.	physical description of the LILT process	78
6.3.4.	LILT - process development	87
6.3.5.	possibilities and limitations	98
7.	Conclusion	102
A.	molecular structures	106
	Bibliography	108

1. Introduction

Organic light emitting diodes (OLED) represent an important emerging technology for flat panel displays and solid state lighting [1,2]. The fast-paced development of mobile electronic devices demands for thin, light-weight and power-efficient display panels. So far, the need for mobile or desktop flat panel displays (FPD) was mainly satisfied by liquid crystal displays (LCD), which are further expected to take over the market leadership in the large panel segment within the near future. OLED technology promises further weight and power savings, a larger viewing angle, higher brightness levels and an increased contrast ratio, but still lacks in terms of reliability and suitable mass production equipment. This work contributes to the development of device and process technology for high-resolution full color OLED displays.

1.1. organic light emitting diodes

First reports on organic electroluminescence in vacuum-deposited or spin-coated thin film devices [3,4] excited intensive research activities on organic light emitting devices within the last two decades. One of the decisive achievements compared to earlier reports [5] was, that a significant light output could be measured at very low operating voltages of about 10 V or less. The proposed OLED structure complies with the functional schematic displayed in figure 1.1.

The significant difference to prior work is, that a heterostructure consisting of a mainly

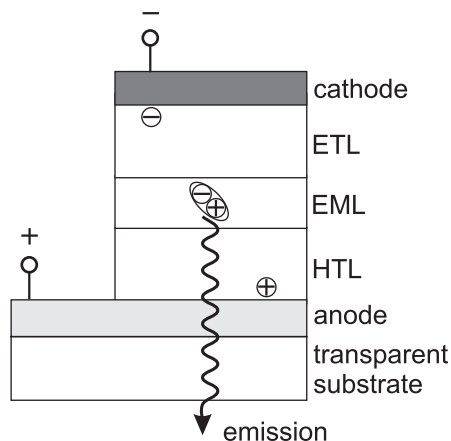


Figure 1.1.: Working principle of organic light emitting diodes, as proposed in reference [3].

electron transporting material and a mainly hole transporting material is employed. When an external voltage is applied, electrons are injected from the metallic cathode into the electron transporting layer (ETL). Correspondingly, the transparent indium tin oxide (ITO) anode injects holes into the hole transporting layer (HTL). Often a dye-doped ETL or HTL is employed as emission layer (EML). Recombination of charge carriers occurs within the EML at the heterointerface between the ETL and HTL and leads to the formation of excitons. The radiative decay of excited states can be observed by the light, which is emitted through the transparent substrate. Today, highly efficient OLEDs employ phosphorescent emitter materials and yield external quantum efficiencies of up to 29 % [6].

1.2. OLED-displays

In the past two decades, research on organic light emitting diodes was driven by the idea of realizing outstanding flat panel displays. In principle, two possible ways of realizing OLED displays can be pursued. The first generation of commercially available OLED displays employed a passive-matrix (PM) driving scheme. These displays are used in low information content sub-displays for mobile or automotive applications. Currently, the next generation of OLED displays is developed, which are driven by an active-matrix (AM) backplane. Both driving schemes shall be briefly outlined.

1.2.1. passive-matrix OLED displays

In a passive-matrix OLED display, single pixels are defined by the intersection of patterned anode rows and cathode columns. Usually the anode consists of a transparent conductive oxide (TCO), for example indium tin oxide (ITO), which can be patterned by photolithography and wet-chemical etching. Since the organic materials are very sensitive to solvents and etching agents, the cathode columns cannot be patterned via photo-lithography. The patterning task is therefore solved by evaporating the metal cathode either through a thin shadow mask or onto a pre-patterned photoresist layer with deeply undercut edges at which the organic layers and the metal film separates into columns [7,8].

During operation, only one anode row is addressed at once and the brightness level of each pixel of this row is determined by the current, which is imposed onto the corresponding cathode column. Leakage currents, which may lead to crosstalk between different rows, are suppressed by applying a reverse bias onto all rows except the one, which is currently addressed. In the described multiplexing scheme, the fraction of on-time is inverse proportional to the number of anode rows. As a consequence, a peak luminance of more than

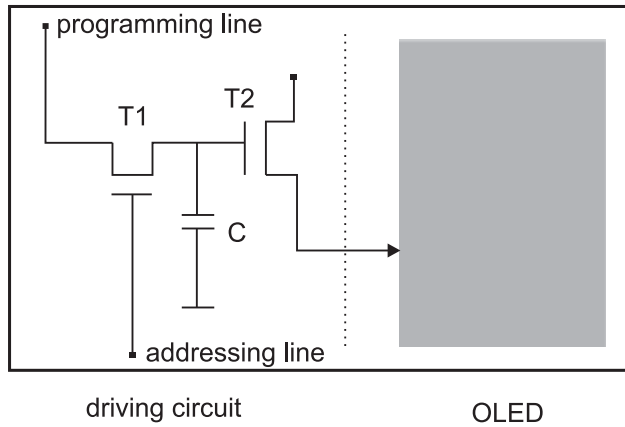


Figure 1.2.: AM-OLED pixel: Horizontal integration of TFTs and bottom-emitting OLEDs.

24000 cd/m² is necessary, to achieve an average brightness of 100 cd/m² for a quarter-VGA resolution (320 x 240 pixels) [9]. At such high brightness levels, the increased driving voltage and resistive respectively idle losses due to charging and discharging of the anode and cathode lines dramatically reduce the overall system efficiency. Model calculations for quarter-VGA PM-displays showed, that an initial OLED efficiency of 10 lm/W is reduced to a system efficiency of about 0.2 lm/W [10], which suggests, that PM-OLED displays will not be suitable for high-resolution full-color OLED displays.

1.2.2. active-matrix OLED displays

Due to resolution limitations, which arise from the high peak luminance in PM-OLED displays, it is favorable to apply an active driving scheme, which permanently supplies the necessary driving current to the OLED. Corresponding to this need, a large number of reports on silicon-based [11–13], organic [14–16] or even highly transparent, ceramic [17] thin film transistors (TFT) integrated onto OLED substrates was published. It is most likely, that existing polycrystalline or amorphous silicon technology will be used for the first generation of commercial AM-OLED displays.

For controlling the OLED current, at least two transistors have to be employed in AM driving schemes, as depicted in figure 1.2. The displayed pixel is addressed via transistor $T1$. When switched on, a gating voltage for transistor $T2$ is programmed onto the store capacitance C . If C is charged, the transistor $T2$ is switched on and the pixel is illuminated. Discharging of the capacitance switches off the current flow through $T2$ and the pixel remains dark. Driving circuits, which consider gray-scaling and threshold voltage compensation, commonly use 3 or more transistors per pixel [9, 13, 15]. In a bottom emitting architecture, the OLED has to be placed beside the driving circuit to allow the generated light to be emitted through the substrate. This inherently limits the filling factor, which is defined as the ratio of light

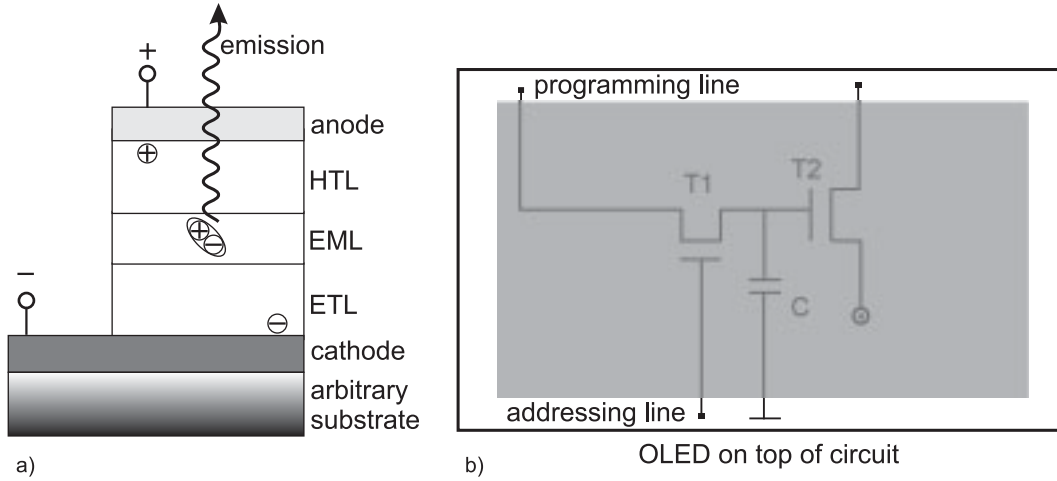


Figure 1.3.: AM-OLED pixel employing an inverted OLED design: a) Structure of an inverted organic light emitting diode. b) Vertical integration of TFTs and top-emitting IOLED.

emitting to total pixel area. In general, a filling factor of 30 - 40 % is suggested for bottom-emitting AM-OLED architectures, which turns out to be a fundamental drawback.

Higher filling factors can be achieved by employing top-emitting OLED concepts. These are conventional OLEDs emitting light through a transparent or semi-transparent cathode [18–22] and inverted organic light emitting diodes (IOLEDs) [23–25] with sputtered ITO top-anodes. In the latter case, more effective n-channel TFTs can be used for the AM-backplane [9]. Figure 1.3 depicts the inverted device concept, which demands for a reversed deposition sequence. Now, the light is emitted through the transparent top anode, which allows vertical integration of the light emitting device on top of the AM driving circuit and significantly increases the filling factor. The inverse deposition sequence implies several technological challenges, of which sputtering of ITO on top of sensitive organic layers is identified as the most severe task. Polymeric or molecular polycrystalline buffer layers were introduced to prevent from sputter-induced damage [24–26]. The reversed layer sequence also affects charge injection from the electrodes, which can be improved by applying doped charge injection layers [25]. Although the preparation of IOLEDs underlies certain limitations, the benefits for AM-OLED displays makes IOLEDs appear as a promising and important topic for further research activities.

1.2.3. production issues

So far, the OLED technology did not fulfill the predicted expectations for the display market. To some extent, this can be explained by the lack of mass production equipment and the incompatibility of several preparation processes to production demands. For commercial success, the production of OLEDs must be as cost-effective and reliable as it holds for today's LCD production, which sets the standards as dominating technology. Several of the front- and back-end processes can be adopted under minor efforts. For example, the cleaning of the substrates and packaging of finished devices are referred. A major difference in the process chain arises, when the deposition of organic materials is concerned. Several different approaches for high-yield, high-throughput deposition of OLEDs were introduced in the past. Among these are thermal evaporation from multiple point sources within cluster-type OMBD tools, ultrahigh-rate organic vapor phase deposition within a single reactor [27, 28], and thermal evaporation from linear sources within an inline configuration [8, 29]. In the LCD production, inline sputtering of ITO already proofed its reliability under high-throughput conditions. Therefore, it is reasonable to employ inline deposition systems for mass production of OLEDs. Due to the nonexistence of suitable co-evaporation sources and patterning technologies for substrate sizes exceeding 1 m^2 , further efforts have to be carried out until large AM-OLED screens will be commercialized.

1.3. goals and outline of this study

This work is motivated by the development of device and process technology for full-color AMOLED displays. It is expected that the application of phosphorescent emitter materials will significantly increase the efficiency of inverted organic light emitting diodes. In the course of this study, a stacked device concept for IOLEDs is proposed and will be intensively examined. A second emphasis is placed onto the development of inline deposition processes and equipment. Concerns are focused on room-temperature sputtering of ITO, co-evaporation of organic materials and patterning technology.

The presented study can be outlined as follows:

Chapter 2 starts with an introduction to basic models describing charge injection, charge transport and recombination in organic light emitting diodes. Following, a brief summary of device preparation and characterization is given in chapter 3.

In Chapter 4 experimental results for inverted organic light emitting diodes employing highly efficient phosphorescent materials are discussed. The discussion comprises the identification

of quenching mechanisms and possible ways to minimize these, which leads over to the realization of highly efficient red, green and blue IOLEDs.

Next, stacking of OLEDs as a new device concept is demonstrated (Chapter 5). A physical model of the charge separating mechanism at doped organic pn-junctions is drawn from experimental data obtained by Kelvin Probe measurements and temperature-, respectively thickness-dependent current voltage characteristics. It will be shown, that the application of the stacking approach to inverted OLEDs yields an outperforming device efficiency.

The development of inline deposition processes and equipment is presented in chapter 6. The chapter starts with a discussion of the influence of oxygen flow and RF power ratio on the optical and electrical properties of room temperature (RT) sputtered ITO.

Further, a unique design of a linear co-evaporation source is visualized and evaluated by thickness and concentration distributions of thin films deposited onto large substrates.

To the end of chapter 6, the laser induced local transfer of organic emitter materials is proposed as novel, high-resolution patterning technique for full-color OLED displays. The process will be described by a physical approximation. The approximated model will be confirmed by comparison to the experimental results.

2. Charge injection, transport and recombination

Organic chemistry comprises millions of substances, of which most are regarded as insulators. The discovery of conducting polymers marked an important breakthrough in material science [30]. Compared to the vast majority of insulating organic compounds, conducting and semiconducting polymeric or molecular materials represent an exceptional minority. Often, these exceptions consist of conjugated carbon rings or chains, which are described in the following sections.

2.1. π -conjugated small molecules

For this work, mainly vacuum deposited thin films of molecular compounds were used. Therefore the physical properties of organic semiconductors will be discussed by means of molecular compounds. Nevertheless, the dependencies, which are illustrated in this section may also be applied to polymeric materials. For a deeper understanding of the electric conductivity in organic materials, it is important to view at the electronic configuration of the carbon atom. The carbon sp^2 hybridization is depicted in figure 2.1. In the sp^2 electron configuration, which for example appears in graphite, the three sp^2 hybrid orbitals are singly occupied. The remaining valence electron is transferred to the p_z -orbital, which extends symmetrically out of the plain defined by the sp^2 -hybrids. When covalently linked to each other, the so-called σ -bond is established under electron exchange of neighboring carbon atoms via their sp^2 hybrid orbitals. σ -electrons are firmly bound and highly localized. Those electrons, which were transferred to the p_z -orbitals, stabilize the covalent bond by forming a so-called π -bond. The complete bond is known as carbon double bond. Adding more carbon atoms to this picture leads to a continuous alternation of single and double bonds, which is found in polymer chains and cyclic molecules like benzene. Due to the low binding energy, π -electrons are delocalized and cannot be assigned to a single atom. As consequence, the overlap of the π -orbitals leads to an extended π -electron system. In the molecule, the electronic states of the atom's p -orbitals split up to binding π - and anti-binding π^* -states (see figures 2.1d-e). The highest occupied π -state is called HOMO (Highest Occupied Molecular Orbital). For the lowest π^* -state the abbreviation LUMO (Lowest Unoccupied Molecular Orbital) is commonly used.

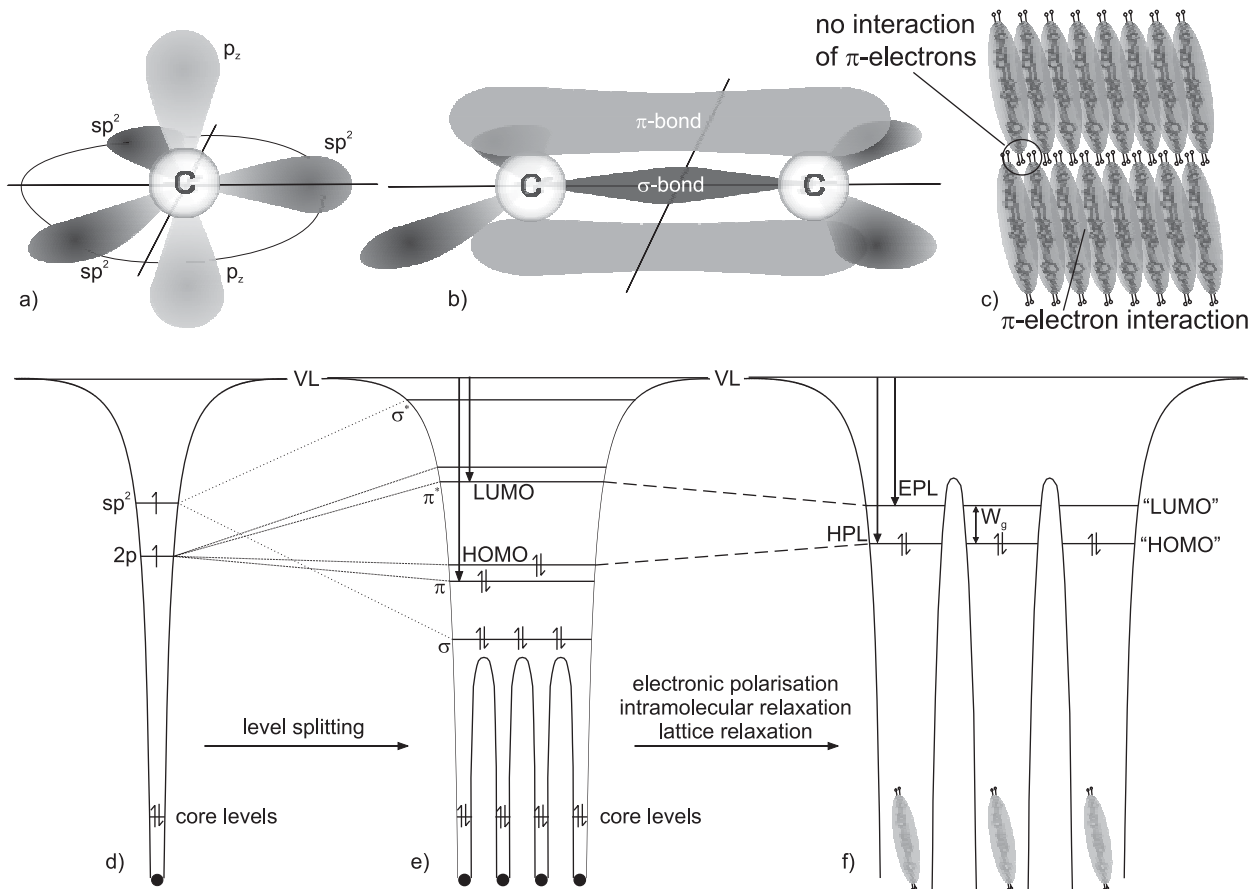


Figure 2.1.: a) sp^2 electron configuration of the carbon atom. b) σ -bond and π -bond for sp^2 -hybridized carbon atoms. c) Interaction of π -electrons in molecular crystals. d)-f) Energy level diagram for d) the carbon atom (sp^2 -configuration), e) a model molecule and f) a model molecular crystal. Only relevant states are explicitly indicated.

In the solid, molecules are weakly bound by van-der-Waals-forces. The probability for interaction between π -electrons of neighboring molecules is determined by the overlap of their electronic wavefunctions. Figure 2.1c schematically depicts this situation for a crystalline molecular solid. In the illustrated case charge exchange between these molecules is most likely along the horizontal stacking axis of the crystal, because only in this direction a significant overlap of the π -electron systems is observed. Along the vertical axis, the overlap is negligible, leading to a lower carrier mobility in the vertical direction. The described anisotropy of the charge carrier mobility in molecular organic crystals was documented amongst others for α -perylene single crystals [31]. For inorganic semiconductors, strong coupling of the electron wavefunctions leads to the formation of wide electronic bands and the delocalization of electrons and holes. In contrast, the coupling of the π -electron

systems in organic solids is rather low. Electrons are regarded as highly localized on a single molecule. Therefore, charges are carried via the transfer of an ionized state from one molecule to the next. The ionization of a particular molecule leads to a strong polarization of the surrounding molecules. Further, the reorganization within the π -electron system of the surrounding molecules, results in intermolecular and lattice relaxation, which means a rearrangement of the molecular bonds and/or repositioning within the lattice. Due to the mentioned mechanisms, the potential energy of the charge carriers within the solid is lowered. For anthracene-like crystals, the contribution of electronic polarization is in the range 1.5-2.0 eV, the relaxation energies account for 10-100 meV of intermolecular relaxation and about 30 meV of lattice relaxation [32, p. 45]. When the ionized state is transferred to a neighboring molecule, also the polarization and relaxation energies are transferred. Therefore the charge carrier transport in organic crystals is often described as polaron transport. Now, the highest occupied state is determined by the hole polaron level (HPL) which can be measured by UV photoelectron spectroscopy (UPS) [33,34]. Regarding the HOMO level of the isolated molecule, the HPL is shifted by the polarization energy towards the vacuum level. The electron polaron level (EPL) is shifted to lower energies compared to the LUMO of the isolated molecule. The gap between the HPL and the EPL is denoted as the transport gap W_g . The EPL is often estimated by adding the optical band gap energy¹ to the hole polaron energy. This way, certain errors in the value of the LUMO have to be considered, as the optical band gap differs from W_g by the value of the exciton binding energy, which was measured to be in the range of 0.4 eV to 1.4 eV [35]. More correct values for the electron polaron level can be obtained from inverse photoelectron spectroscopy (IPES) [36]. So far, the terms HOMO and HPL, and LUMO and EPL were used to exemplify the difference between the electronic states of isolated molecules and molecules in the solid. In the further discussion, the term "HOMO" will be used equivalently to the valence band in inorganic semiconductors as transport level for hole polarons. According to the use in literature and as counterpart to the conduction band, the term "LUMO" designates the transport level for electron polarons.

2.2. charge transport

The charge transport in organic materials is governed by the magnitude of electron-electron coupling in relation to electron-phonon coupling. At low temperatures, the electron-electron

¹The optical gap is determined by the energy, which corresponds to the peak wavelength of the emission spectrum.

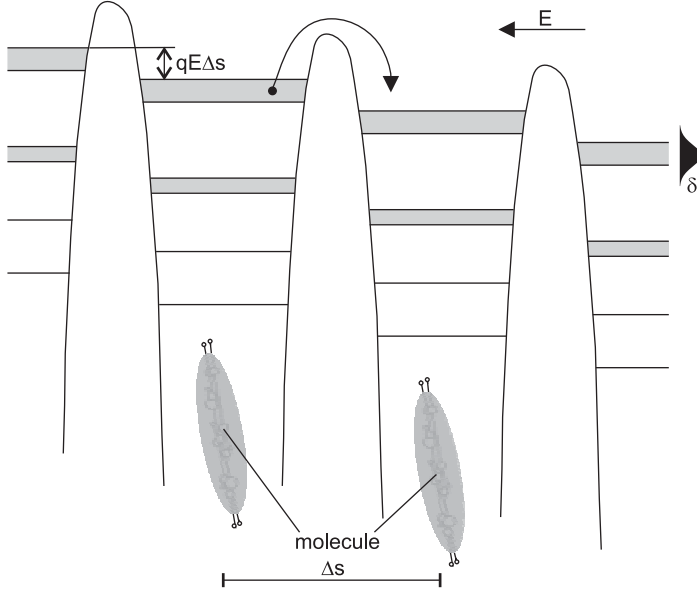


Figure 2.2.: Thermally activated hopping of an electron between two molecules. As the charge carriers are delocalized across the π -electron system, the voltage drops across the potential barrier between two molecules. δ is the width of the disorder-induced Gaussian distribution of LUMO states.

coupling in crystalline organic materials sufficiently exceeds the magnitude of electron-phonon coupling to allow band-like charge transport and charge carrier mobilities of several $100 \text{ cm}^2/\text{Vs}$ [31]. In these high-purity and highly ordered crystals, the mobility decreases with increasing temperature, indicating electron-scattering by phonons. Most materials, which are relevant for the application in OLEDs, reveal an disordered morphology. Under these conditions, the formation of transport bands is unlikely. Further, the magnitude of polarization energy depends on the distance and orientation of neighboring molecules. In disordered systems, the transport levels develop into Gaussian distributions of HOMO and LUMO states. The states in the low energy tail of the distribution act as trapping sites. Charge carriers are now localized and charge transport is either possible via tunneling, or via hopping. Figure 2.2 illustrates the hopping model.

The arrow indicates, that the electron has to be lifted over the potential barrier between the two molecules. This happens by coupling of vibrational modes of the molecule with the electron. Simplified, the zero field hopping rate is proportional to

$$p_{hop} = e^{-\frac{\Delta W}{k_B T}}, \quad (2.1)$$

where $k_B T$ is the thermal energy and ΔW is the activation energy, which represents the height of the potential barrier between two molecules. At zero field, random hops may occur. Due to their random orientation, the average hopping rate equals zero. When an external field is applied, the difference of the hopping rates against and in the direction of the electric field,

yields a net electron hopping rate

$$\Delta p_{hop} = e^{-\frac{\Delta W - qE\Delta s}{k_b T}} - e^{-\frac{\Delta W + qE\Delta s}{k_b T}} = e^{-\frac{\Delta W}{k_b T}} \cdot 2 \sinh \frac{qE\Delta s}{k_b T}, \quad (2.2)$$

where q symbolizes the elementary charge of a single electron and E represents is the local electric field. In contrast to the band model and also the tunneling model², the hopping mobility increases with temperature. In general, the temperature dependence of charge transport in disordered organic thin films confirms an increasing mobility for higher temperatures [37, 38].

In addition to the described temperature dependence, the drift mobility in disordered organic thin films is also affected by the external field. In many cases [38, 39], the field dependence was found to comply with

$$\mu(E) = \mu_0 e^{\frac{\beta \sqrt{E}}{k_B T}}. \quad (2.3)$$

Both dependencies were assigned to the Frenkel-effect, which describes the reduction of the activation energy ΔW of charged traps by reducing the effective trap depth, when a strong external field is present [40]. Then the temperature- and field-dependence of the mobility in amorphous organic solids can be expressed by

$$\mu(T, E) = \mu_0 e^{-\frac{\Delta W - \beta \sqrt{E}}{k_B T_{eff}}}. \quad (2.4)$$

In this semi-empirical description, the field dependence coefficient β and the effective temperature T_{eff} are obtained from experimental data [39]. Equation 2.4 gives a reasonable approximation of the measured drift mobility over several orders of magnitude.

Generally, the charge carrier mobility in organic semiconductors used for technical applications is several orders of magnitude lower compared to inorganic semiconductors. For example, the field effect mobility of holes in polycrystalline pentacene thin films is -depending on substrate conditions- in the order of $1 \cdot 10^{-3} \text{ cm}^2/\text{Vs}$ - $1.0 \text{ cm}^2/\text{Vs}$ [15, 41]. In amorphous thin films of Alq₃ an electron mobility of $5 \cdot 10^{-5} \text{ cm}^2/\text{Vs}$ was measured by a transient electroluminescence technique [42]. A general assumption of the carrier mobility being lower than $1 \cdot 10^{-3} \text{ cm}^2/\text{Vs}$ holds for most of the materials used in this work.

steady current flow in solid state organics

For steady current flow in organic thin films three different regimes have to be discussed. Figure 2.3 shows a model plot of current density against voltage. At low voltages, the electric

²Localized charge carriers may directly tunnel through the potential barrier between two molecules. For tunneling, no explicit temperature dependence is expected.

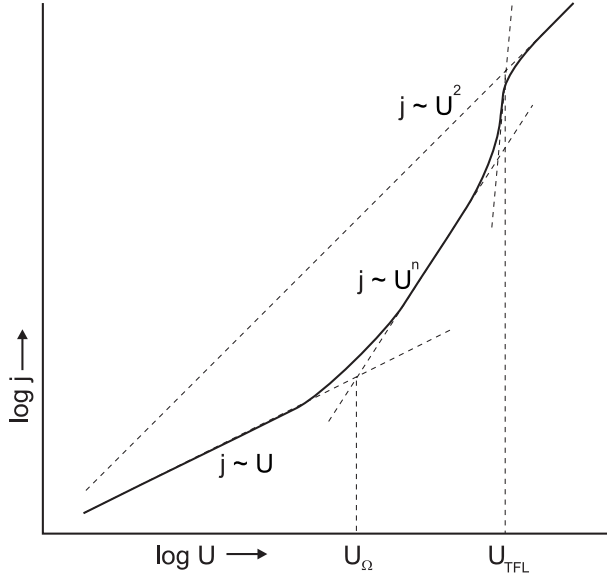


Figure 2.3.: Model current density voltage characteristics. U_{Ω} designates the transition voltage between ohmic and trap charge limited current. U_{TFL} marks the limit at which all traps are filled and the current becomes space charge limited.

current is carried by thermally generated intrinsic charge carriers. Within the ohmic regime, the current density J is described by

$$J = q\mu n_0 U/d, \quad (2.5)$$

where μ_n is the carrier mobility, n_0 is the intrinsic charge carrier density, U is the voltage and d is the film thickness. The intrinsic charge carrier density in materials used for OLEDs is very low. In Alq_3 , the intrinsic charge carrier density n_0 was estimated to be below $1 \cdot 10^{11} \text{ cm}^{-3}$ [43]. The contribution of ohmic conduction to the current flow in organic semiconductors is very low and can only be observed at low voltages. With increasing voltage, the current flow is dominated by injected carriers. In this case, intrinsic carriers can be neglected. In figure 2.5, U_{Ω} marks the transition, when the current flow becomes dominated by injected carriers.

A classical description of current flow by injected charge carriers is presented by the Mott-Gurney-Law:

$$J = \frac{9}{8} \epsilon_r \epsilon_0 \mu \frac{U^2}{d^3}. \quad (2.6)$$

Equation 2.6 models space-charge limited current (SCLC) and assumes ideal contacts and a trap-free semiconductor. It shows, that the current density is proportional to the square of the applied voltage and inverse proportional to the cube of the film thickness d . The assumption of ideal contacts is valid, when the voltage drop at the injecting electrode vanishes. In reverse, this means, whenever the current voltage characteristics of organic semiconductor devices comply with SCLC predictions, the injection at the contacts must be close to ideal. It was mentioned before, that -in contrast to the given preconditions- the drift mobility in

organic semiconductors often follows a field dependence ($\mu = \mu_0^* \cdot \exp(-\beta\sqrt{E})$). By including the Frenkel-effect, the Mott-Gurney-Law was extended to [40]

$$J = \frac{9}{8} \epsilon_r \epsilon_0 \mu_0^* \frac{U^2}{d^3} e^{0.89\beta\sqrt{U/d}}, \quad (2.7)$$

where ϵ_0 and ϵ_r are the absolute and relative permittivity, μ_0^* is the temperature-dependent zero-field mobility and β represents the field dependence coefficient.

Further, the assumption of a trap free semiconductor does not apply to disordered organic thin films. Often, the current is limited by traps (trap-charge-limited current: TCLC) [44]. When the current is increased, the Fermi level rises above the trap level and the traps are filled. This in turn, decreases the relative probability of trapping events for a single carrier, thereby increasing the effective drift mobility. As a result, the slope of the current voltage characteristics in the TCLC-regime is much higher than expected from SCLC-theory. The width and slope of the TCLC-regime is correlated to the trap density and energetic distribution [43]. At high currents, all traps are filled (and the current voltage characteristics is switched over to SCLC again. The transition between trap and space charge limitation is indicated in figure 2.3 as trap-filled-limit (TFL).

2.3. charge injection

In the previous section, ideal contacts were assumed as essential precondition for space-charge limited current. If this condition is not satisfied, the current voltage characteristics become injection limited and injection models rather than transport models describe the current flow in organic thin films.

Although the band model does not provide a satisfying description of charge transport in organic semiconductors, it can be employed for modeling of charge injection. At the interface between the metal cathode and the ETL, electrons have to surpass an injection barrier

$$\Phi_B = \Phi_m - W_{LUMO}, \quad (2.8)$$

which results from the difference between metal workfunction Φ_m and the LUMO level W_{LUMO} . Usually, two models are applied for treating charge injection into semiconductors, which shall be briefly introduced. In a first approximation, interfacial dipoles and traps will be neglected.

When the charge carrier is lifted over the barrier by means of thermal excitation, a thermionic injection model is appropriate. The Richardson equation

$$j_{th} = AT^2 e^{-\frac{\Phi_B}{k_B T}} \quad (2.9)$$

describes the emission of electrons out of a heated cathode into vacuum [45]. In this case, the potential barrier, which has to be overcome, equals the workfunction of the metal. When this model is applied to organic semiconductors, the field induced-lowering of the injection barrier by the Schottky effect has to be considered. The coulombic attraction of injected charge carriers induces a counter charge on the metal surface, which in turn lowers the potential energy of the charge carrier. The effective barrier height is reduced by $\Delta\Phi_B = \beta_{th}\sqrt{F}$ with $\beta_{th} = \sqrt{q^3/4\pi\epsilon_0\epsilon_r}$ and $F = V/d$. Applying this to equation 2.9 yields the Richardson-Schottky (RS) injection current [46]

$$j_{RS} = AT^2 e^{-\frac{\Phi_B - \beta_{th}\sqrt{U/d}}{k_B T}}. \quad (2.10)$$

The Richardson constant $A = 4\pi q m_{eff} k_B^2 / h^3$ equals $120 \text{ A/cm}^2 \text{ K}^2$, when the effective electron mass m_{eff} equals the electron mass m_0 .

In the case of a high injection barrier and comparably low temperatures, a temperature-independent injection mechanism is presented by Fowler-Nordheim tunneling. Here, carrier injection is only driven by the external field. Assuming a triangular injection barrier, the current density is determined by

$$j_{FN} = \frac{Aq^2 F^2}{\Phi_B \alpha^2 k_B^2} e^{-\frac{2\alpha\Phi_B^{3/2}}{3qF}}. \quad (2.11)$$

Here, α equals $4\pi\sqrt{2m_{eff}}/h$ [46, 47]. Both RS-emission and FN-tunneling- apply for inorganic semiconductors with an extended band structure. In disordered systems, trapping dominates the charge carrier transport and the mean free path is in the range of the molecular distance. For charge injection into disordered systems, backflow of injected current is expected. In this case, the presented models for charge injection have to be extended to include the nature of localized charge transport [48].

2.3.1. interface engineering

In equation 2.4, the injection barrier at the contact interface was expressed by the difference between the metal workfunction Φ_m and the LUMO energy W_{LUMO} . It was presumed, that no interfacial dipole is present. In fact, interfacial dipoles are often observed at metal/organic interfaces [33, 49–52]. By lowering or increasing the effective injection barrier, interfacial dipoles at the electrodes exhibit a significant impact on the device characteristics. Several possible factors forming an interfacial dipole layer can be mentioned. Among these are: (I) charge transfer from the metal film to organic molecules and vice versa [33], (II) rearrangement of the metal surface electron distribution [33, 49], (III) chemical reactions [33, 53, 54],

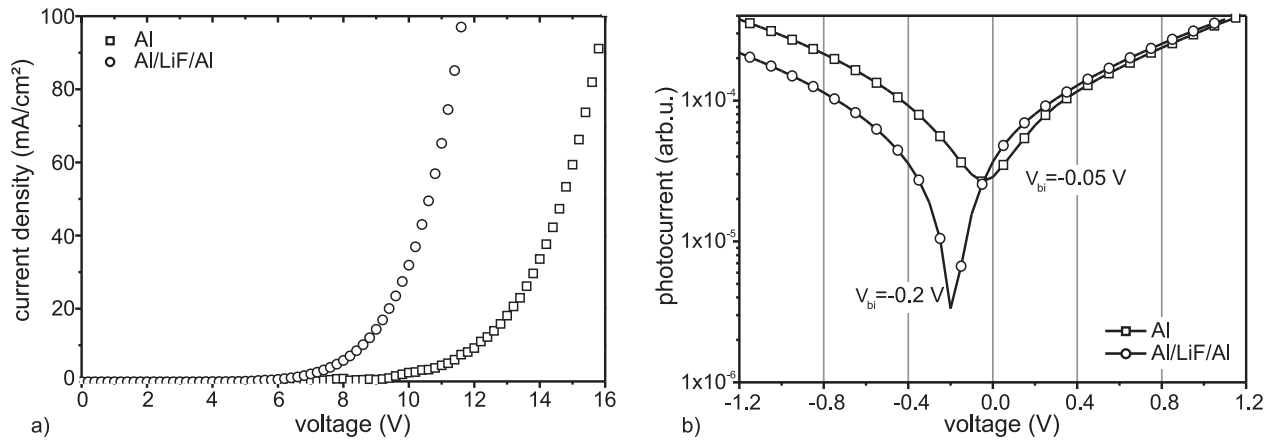


Figure 2.4.: a) Current density plotted against voltage for electron-only devices with Al bottom electrode (squares), respectively Al/LiF/Al bottom electrode (circles). b) Built-in-field photocurrent measurements for Alq₃ single layer devices. Device structure Al (thickness in nm): Al\Alq₃ 100\Al. Device structure Al/LiF/Al: Al\LiF 0.5\Al 0.3\Alq₃ 100\Al.

(IV) the presence of interfacial gap states [33, 55, 56] and (V) permanent dipole orientation [33, 57]. It is obvious, that the responsible mechanism strongly depends on the material choice. Due to the strong influence of the interface's nature on device characteristics, strong efforts were undertaken to enhance the injection of charge carriers by interface engineering as indicated by a large number of references to be found in literature [53, 58–62].

For electron injection, the insertion of sub-nm alkali-metal-fluoride layers between the ETL and the metal contact is commonly accepted as state-of-the-art cathode design [22, 54, 63–66]. The observed improvement of charge injection was explained by a chemical reaction involving Al, LiF and Alq₃, leading to the liberation of Li atoms, which diffused into the organic layer [54]. This interfacial n-type doping increases the density of free carriers close to the interface and reduces the injection barrier. The activation energy needed for the chemical reaction comes with impinging Al atoms, when deposited. Therefore, the injection efficiency clearly depends on the deposition sequence. When the deposition sequence was inverted, the injection current decreased by several orders of magnitude. As a consequence of the inverted layer sequence, Al/LiF cathodes are not suitable for IOLEDs in the so far described configuration.

Therefore a slightly different cathode configuration was investigated by means of Alq₃ single layer devices. The deposition sequence was 100 nm Al, 0.5 nm LiF, 0.3 nm Al, 100 nm Alq₃ and 150 nm Al. The thin Al film serves as activation layer. To observe electron injection from the bottom electrode, a negative bias was applied to it. As the Al electrodes exhibit

poor hole-injecting properties, the injection of holes from the top-electrode can be neglected. Figure 2.4 compares the injection current of a device incorporating the described LiF/Al cathode sequence with a control device employing Al-electrodes at bottom and top. Applying an Al/LiF/Al-contact increases the driven current for a given bias by a factor of 10 to 20. A possible explanation follows the cited reasoning [54] as a thermally assisted chemical reaction, liberating Li atoms, which may dope the Alq₃ layer close to the interface. The comparison of the contact potential difference (CPD) of the LiF-containing device with the CPD of the control device by means of photocurrent measurements³ confirms a lowering of the electron injection barrier by 0.15 eV. In the meantime, the presented results were confirmed by another publication [68]. In the further context of this work, the proposed LiF/Al cathode configuration was employed for IOLEDs with intrinsic ETL, which will be discussed in chapter 4.

In conventional bottom emitting OLEDs, ITO serves transparent anode. Several publications report on improved device characteristics upon oxygen-plasma or UV-ozone treatment prior to the deposition of the organic layers. [59,69]. Although the absolute value of ITO workfunction differs by several 100 meV for various publications, it is generally acknowledged, that the improved device characteristics are due to a higher ITO workfunction for pretreated ITO-surfaces, which in turn causes a lower hole injection barrier [59,69–73]. The change of the ITO workfunction was attributed to the removal of C-containing contaminants, and oxygen enrichment of the ITO film close to the surface.

In an inverted OLED design, the inverted deposition sequence does not allow any post- or pretreatment of the organic/ITO interface. So far published work dealt with stable organic buffer layers [23,24,26], but did not focus on the possibility to tune the ITO workfunction by an in-situ oxygen enrichment during the deposition itself. To bridge the gap between conventional and inverted IOLEDs, the influence of the oxygen content during the sputtering process was tested on pentacene single layer devices. Pentacene serves in IOLEDs as

³A difference in the contact potential of top and bottom contact results in a built-in field, which can be detected by the photoelectric effect. For measuring the built-in-field photocurrent, an organic sample layer is sandwiched between a semi-transparent reference electrode and an opaque test electrode. When the sample is exposed to UV light electron-hole-pairs are generated within the organic layer. Under the influence of the built-in-field electron-hole-pairs are dissociated and drift towards the electrodes, provoking current flow, which is measured in the outer circuit. A balancing external field is applied, to minimize the measured photocurrent. The voltage which has to be applied to minimize the photocurrent is directly related to the contact potential difference between the two electrodes. This way, the height of the injection barrier for the test electrode is set into relation to the barrier height of the reference electrode. A detailed description of photoelectric CPD measurements and the experimental setup can be found in [67].

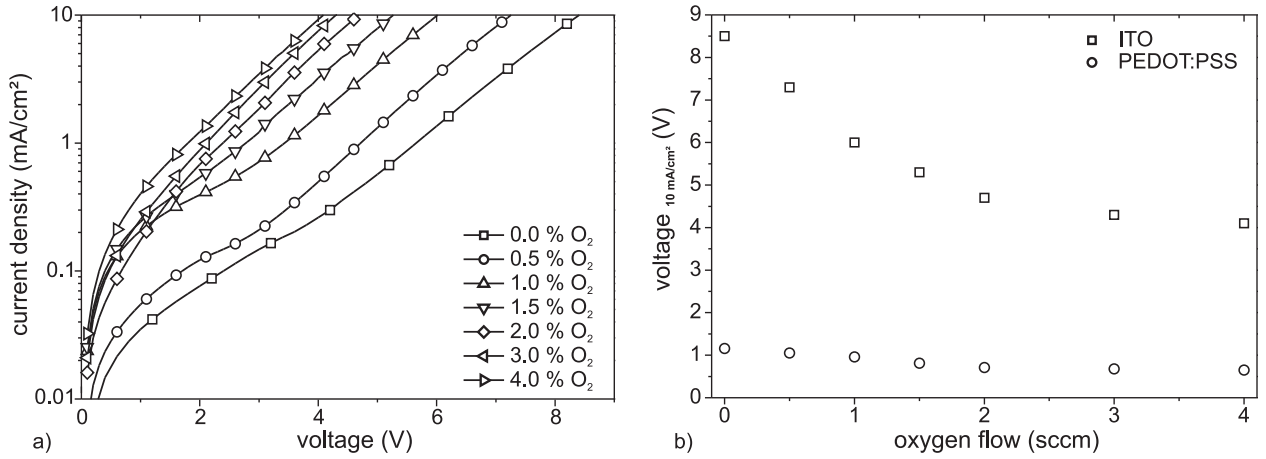


Figure 2.5.: Comparison of several pentacene single layer devices with top ITO anodes sputtered under varying oxygen flow. a) Current density voltage characteristics. b) Operational voltage at a current density of 10 mA/cm^2 plotted against oxygen flow. Injection from top Oxy-ITO anode (squares) and bottom PEDOT:PSS anode (circles). Device structure (thickness in nm): commercial ITO\PEDOT:PSS 30\pentacene 200\Oxy-ITO buffer 5\RT-ITO 90.

protective buffer layer [24] and was deposited onto an PEDOT:PSS coated commercial ITO substrate. PEDOT:PSS was employed to reduce the probability of electrical shorts and to give a common reference electrode for all devices. The top electrodes were deposited in a two step sputtering sequence. For each sample, a 5 nm thick seed layer was deposited at a reduced DC power density of 0.26 W/cm^2 , varying the oxygen flow for each sample while keeping the Ar flow constant. In the second step, a 95 nm thick ITO film was sputtered at 1.04 W/cm^2 DC power within a 1-to-50 oxygen-to-argon atmosphere. This way, it was possible to vary the oxygen content of the film close to the ITO/organic interface, without affecting the lateral conductivity. Section 6.1 presents a study on the influence of oxygen content on the electrical and optical properties of RF/DC sputtered ITO films and gives detailed information about the process parameters.

Figure 2.5 plots current density against voltage for devices sputtered under varying oxygen flow. The plot shows, that when comparing the device with zero oxygen flow to the device with 4.0 sccm, the injection current is increased by a factor of 30 to 50. In the case of the former device, a characteristic current density of 10 mA/cm^2 , can be reached by applying a bias of 4.1 V. The corresponding value for the device sputtered in a pure Ar atmosphere is doubled to 8.4 V (see figure 2.5b). The results confirm, that sputtering of ITO in an oxygen rich atmosphere dramatically improves the hole injection properties of ITO top electrodes. The workfunction of the oxygen enriched seed layer is expected to rise, thereby lowering the hole injection barrier, as it was confirmed for oxygen-plasma treated ITO surfaces in

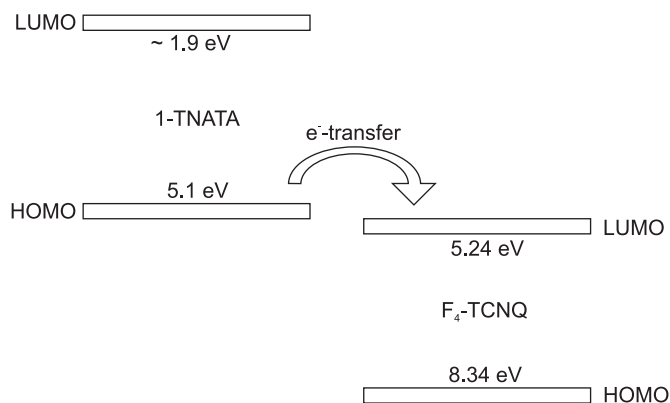


Figure 2.6.: Doping mechanism in F₄-TCNQ-doped 1-TNATA HTL. The energy values for HOMO and LUMO levels were derived from literature [82, 91].

conventional OLEDs [59, 69]. A saturation of the effect is observed for oxygen flows higher than 4 sccm.

The injection current from the bottom PEDOT:PSS anode is also displayed in figure 2.5b. The voltage drop, across the device for a current density of 10 mA/cm² is always lower than 1.2 eV. The superior injection properties of PEDOT:PSS over ITO or Au anodes have already been reported [26, 74, 75]. A hybrid anode concept, which includes the application of PEDOT:PSS as highly injective top anode, was proposed in a prior work and intensively studied [25]. It was found out, that spin-coating of PEDOT:PSS was enabled by the hydrophobic nature of pentacene thin films, which act as water diffusion barrier. Within the scope of this work, the hybrid anode concept was employed for the fabrication of IOLEDs. Nevertheless, oxygen-rich ITO seed-layers may promise improved device characteristics for small-molecule-based IOLEDs in the future.

2.3.2. doped charge transport layers

Acceptor and donor doping significantly increases the electrical conductivity of organic semiconductors. In the past, several approaches for p- and n-type doping were introduced. p-type doping was demonstrated by oxidizing gas treatment [76], by inorganic oxidizing agents [77–79], or by organic acceptor molecules [80–83]. For n-type doping, alkaline metals [84–86] or molecular donors [87–89] were employed. Within the scope of this work, p- and n-type doping was employed for the purpose of realizing highly efficient IOLEDs and stacked devices. As the doping mechanism itself was not piece to investigation, the employed doping approaches employed will only be briefly outlined. A comprehensive survey about various doping techniques is given for further reference [90].

Acceptor doping: p-doping was performed by co-evaporation of the starburst derivative 1-TNATA and the molecular acceptor F₄-TCNQ. Figure 2.6 schematically depicts the dop-

ing mechanism. In general, TCNQ-derivatives establish a material class, which features strong accepting properties. In the case of the fluorine substituted F_4 -TCNQ, the accepting nature of TCNQ is intensified by the strong electronegativity of fluorine. This leads to deep lying HOMO (8.34 eV) and LUMO levels (5.24 eV) [82]. It shows, that the LUMO level of F_4 -TCNQ lies even below the HOMO level of the matrix material 1-TNATA. When doped into 1-TNATA it may be energetically favorable, that 1-TNATA donates an electron to F_4 -TCNQ. This leaves a hole carrier on the 1-TNATA molecule, which participates in the current transport. Concerning bulk properties, the described mechanism leads to a drastic increase of the free carrier density, meaning a twofold benefit for the device characteristics. First, the increase in bulk conductivity reduces resistive losses across the transport layers. Second, the presence of free charge carriers at the interface between the injecting electrode and the transport layer, leads to the formation of a thin depletion zone, which is transparent to tunnel injection, minimizing the contact resistance [82].

Donor doping: Doping of electron transporting materials with alkaline metals, was performed by co-evaporation of Li and electron transporting materials TPBI and BPhen. When doped into an electron transporting host, Li donates its valence electron to achieve a noble gas configuration. Results for photoelectron spectroscopy on Li-doped 2,9-dimethyl-4,7-diphenyl-1,10-phenanthroline (BCP) indicate, that the formation of a $BCP^-:Li^+$ charge transfer (CT) complex is likely. With increasing doping concentration the Fermi level moves by 0.6 eV toward the LUMO edge [86]. For co-evaporated BPhen:Li films, the optimum doping concentration is given by a molar ratio of 1:1 [92]. Prior to this work, the suitability of Li-doped Alq_3 and BPhen for the application as electron injection layer in IOLEDs was tested [25]. In a brief summary for both materials, dramatically improved I-V characteristics were measured, when doped with Li. In line with the picture drawn for p-doping, this was assigned to an increased bulk conductivity and enhanced charge injection, due to the formation of a narrow depletion zone. The width of the depletion zone has to be small enough, to be transparent for tunnel injection.

It has to be pointed out, that Li- and F_4 -TCNQ-doping inherits a fundamental drawback, when lifetime is concerned. It has been demonstrated that F_4 -TCNQ tends to diffuse in polycrystalline phthalocyanine layers [86]. Li was shown to instantly diffuse up to 70 ± 10 nm into the bulk, when evaporated onto BCP thin films [86]. When dopant diffusion extends into the emission layer, exciton quenching is likely [92, 93]. To some extent, diffusion can be suppressed by employing amorphous host materials [82], but cannot be fully excluded at elevated temperatures during operation. A possible solution to this problem is the use

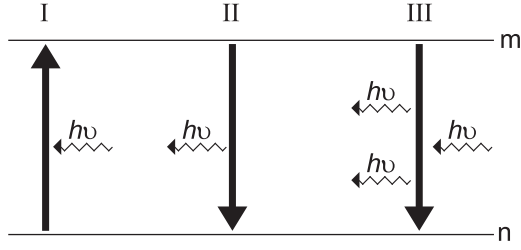


Figure 2.7.: Light interaction with matter: I) absorption, II) spontaneous emission, III) stimulated emission.

of inorganic salts and metal oxides for inexpensive n- and p-doping of transport layers, as reported recently [94–96]. It is expected, that these approaches may enable a higher temperature stability, which in turn leads to longer device lifetimes.

2.4. luminescent properties of organic dyes

Excited states in organic materials can either be generated by photoexcitation or by recombination of charge carriers. In the context of OLEDs, photoexcitation is mainly used for spectroscopic investigations like photoluminescence (PL) measurements or ultraviolet photoelectron spectroscopy (UPS) to gain a deeper understanding of the working principle of the devices. Therefore, a brief description of light absorption in solid state organics will be given. The recombination of injected charge carriers is the basic working principle of OLEDs and will be discussed in section 2.4.2.

2.4.1. photoexcitation

The interaction of light and matter is described by three principal processes, as shown in figure 2.7. Absorption of a photon (I) leads to a transition from an initial state n to a final state m . Light emission is divided into spontaneous (II) and stimulated (III) processes. Due to conservation laws, the difference between the energies of state n and state m ΔW must equal the discrete photon energy $h\nu$. The probabilities of transitions between both states are given by the Einstein equations for light absorption and emission:

$$r_{n \rightarrow m} = N_n B_{nm} I(\nu) \quad (2.12)$$

$$r_{m \rightarrow n} = N_m [A_{mn} + B_{mn} I(\nu)]. \quad (2.13)$$

In the given equations $r_{n \rightarrow m}$ and $r_{m \rightarrow n}$ represent the rate of absorption processes, respectively emission processes. N_n and N_m are the densities of states n and m , $I(\nu)$ is the frequency-dependent light intensity. The material properties are considered by the specific proportionality constants A_{mn} (spontaneous emission), B_{mn} (stimulated emission) and B_{nm}

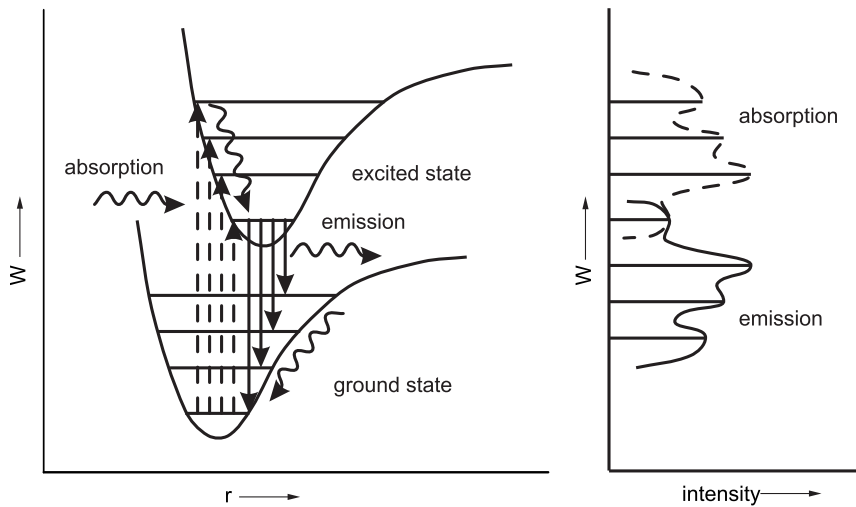


Figure 2.8.: Light emission and absorption in a bi-nuclear molecule.

(absorption). When thermal equilibrium conditions are applied, meaning equal numbers for rates of light emission and absorption, the light intensity $I(\nu)$ for a constant temperature T can be expressed as

$$I(\nu) = \frac{A_{mn}}{B_{nm}e^{\frac{h\nu}{k_B T}} - B_{mn}}. \quad (2.14)$$

The probability of any arbitrary transition within electronic systems can be calculated by quantum mechanics. In quantum mechanics, the absorption of light is described as the reaction of an electronic system to a perturbation by an electromagnetic wave. The discussion of quantum mechanical calculations of molecular properties would by far exceed the scope of this work. Instead, light absorption and emission properties of a bi-nuclear molecule shall be exemplified.

Figure 2.8 shows the ground state and the first excited state of a bi-nuclear molecule. Ground and excited states include associated vibrational modes. Due to a rearrangement of the covalent bond upon excitation, the nuclear distance r between the atoms in the relaxed ground state is smaller than in the excited states. A shift of the nuclear distance demands for a momentum, which is much higher than the momentum carried by a single photon. Conservation of momentum applies and only transitions between states with the same nuclear distance are allowed. As indicated in figure 2.8, absorption processes are most likely between the low energy modes of the ground state and high energy modes of the excited state. The lifetime of the excited state is much higher than the time scale for thermal intrastate relaxation of high energy vibrational modes, leading to a depletion of latter ones. Therefore emission processes take place between the low energy modes of the excited state and high

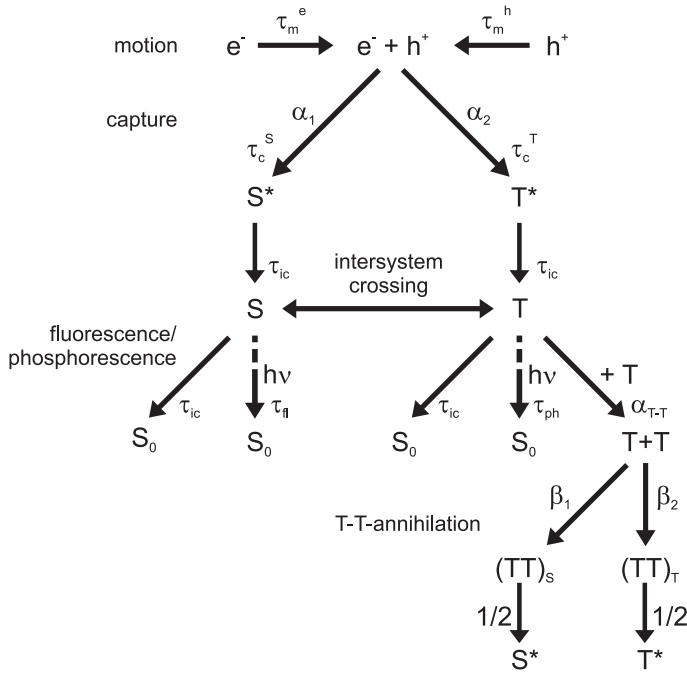


Figure 2.9.: Schematic description of recombination and decay paths for excited states in organic light emitting diodes.

energy modes of the ground state (which are then quickly depleted themselves). In summary, the emission spectrum is found to be red-shifted to the absorption spectrum, which is known as Franck-Condon-shift and a common property of organic dyes.

2.4.2. charge carrier recombination

So far, the charge transport in organic solids and the photoelectric properties of single molecules have been discussed. The following discussion of carrier recombination and excitonic decay paths links the modeling of charge transport in organic solids to the photoelectric properties of single molecules. Figure 2.9 depicts recombination and decay paths for injected charge carriers.

The charge carrier recombination in disordered organic solids is referred as Langvin-like [97]. Langvin's theory of recombination in ionized gases divides the recombination process into motion and elementary capture. The carrier motion time is defined as the period which elapses until the carriers enter the coulombic radius $r_c = q^2/4\pi\epsilon_0\epsilon_r k_B T$. The elementary capture time is defined as the period, which elapses from entering the coulombic radius until the annihilation of charge carriers. Langvin assumes that the carrier motion time τ_m is much higher than the elementary capture time τ_c , which applies for organic semiconductors, in which the mean free path of charge carrier (1 nm) is much lower than the capture radius ($r_c = 15$ nm) [97]. Langvin-like charge carrier recombination is therefore diffusion-limited. The correlated charge carriers are annihilated either to singlet- or triplet-excitons, depending

on the spin multiplicity of the excited state. The spin multiplicity m is defined by the spin quantum number s , following $m = 2s + 1$. Electrons have spin $+1/2$ or $-1/2$. Recombining charge carriers can have either antiparallel or parallel spins, resulting in a spin quantum number of 0 (singlet, $m=1$) or 0 ($m=3$, triplet), respectively. Due to spin statistics, the initial singlet to triplet ratio $\alpha_1 : \alpha_2$ is determined to be 1 to 3 (assuming equal capture times for singlet and triplets). After carrier recombination, the excitons relax radiationless and very rapidly to the lowest vibrational level. This process is indicated by the decay time for internal conversion τ_{ic} . Decay to the ground state and exchange of energy between the singlet and triplet state occurs via fluorescence, phosphorescence, internal conversion, intersystem crossing or annihilation processes. These terms will be separately discussed:

Fluorescence denotes the radiative decay of excited singlet states S_1 to the ground S_0 . The fluorescent transition is spin-conservative. A very high probability is expected for the fluorescent singlet decay. This is reflected in very short singlet lifetimes of a few ns or even below. As mentioned, only 25 % of the electron-hole-pairs recombine to singlet states. This means, that fluorescent emitters are limited to about 25 % internal quantum efficiency. In some cases, triplet-triplet-annihilation (T-T-annihilation) generates singlet excitons, and improves the quantum efficiency.

Phosphorescence describes the non-spin-conserving radiative decay of the triplet state T_1 to the ground state S_0 . Spin conservation applies for the majority of materials and non-radiative decay processes (see: internal conversion) dominate. In these materials the triplet lifetime can be in the ms-range. For Ir- or Pt- based complexes, very efficient phosphorescence was observed. The central heavy metal atom causes strong spin-orbit coupling, which modifies the selection rules for allowed transitions. The increased probability for luminescent triplet decay is reflected in a decreased phosphorescence lifetime τ_{ph} of several 10 ns.

Internal Conversion includes any type of non-radiative energy loss in the system and can be assigned to electron-phonon coupling. As mentioned before, intrastate conversion is responsible for a very rapid relaxation from higher vibrational modes to the lowest level of the same electronic state. This allows the conclusion, that the time constant for intrastate conversion τ_{ic} must be much shorter than the singlet decay lifetime. In contrast, the time constant for interstate conversion describes the thermal relaxation from an excited state to the ground state. As the energy gap between excited and ground state is much higher than the difference between vibrational levels of the same state, the time constant for interstate conversion is longer. In fluorescent emitters, triplet states decay via interstate conversion.

Intersystem crossing is the radiationless transfer of singlet energy to a triplet state of the same energy and vice versa. In phosphorescent emitters, intersystem crossing is very

effective and leads to the complete transfer of singlet energy to triplet states, which quenches the fluorescence in favor of a phosphorescence yield of 100 % photons per generated excitons.

T-T-annihilation occurs, when two neighboring molecules form a temporary excited complex. It represents a possibility of increasing the internal quantum efficiency of fluorescent emitters, but also quenches the efficiency of phosphorescent emitters. In the former case, T-T-annihilation is exploited to generate further singlet excitons, as shown in figure 2.9. The quenching effect of T-T-annihilation in phosphorescent emitters is reflected in the efficiency roll-off, which is observed for higher current densities. In this context, lowering the phosphorescence lifetime (by molecular design) is equivalent to a reduction of T-T-annihilation. As the influence of T-T-annihilation is expected to be dominant, other types of exciton-interaction (for instance triplet-singlet or triplet-polaron) shall not be discussed.

exciton diffusion

As a consequence of the charge carrier localization and strong polarization effects in organic solids, excitons are expected to be of the Frenkel-type, in which both charge carriers are trapped on a single molecule. In some cases excited charge transfer complexes may occur. Both types of excitons have a very small excitonic radius and a high exciton binding energy in common. The transfer of excitation energy from one molecule to another is traditionally described by Förster or Dexter transfer. Former is based upon dipole-dipole interaction between an excited donor molecule and an acceptor molecule. Efficient energy transfer is possible, when the acceptor molecule is found to be within the so called Förster radius, which is in the range of 4-10 nm. Often, the effectiveness of the Förster mechanism is estimated by the spectral overlap of the donor's emission spectrum with the acceptor's absorption spectrum. As the spin orientation has to be conserved, the Förster transfer applies only for singlet excitons. Triplet excitons are transferred via the Dexter mechanism, which can also be applied for singlet excitons. As the Dexter transfer requires the formation of a transfer complex $(D A)^*$ of neighboring molecules, the transfer range is limited to 1 nm or less. The exciton diffusion length is determined by the transfer rate and the exciton mean lifetime. The triplet diffusion length in Alq₃ was determined to 140 nm [98]. As a consequence of exciton diffusion to the OLED design, blocking layers have to be applied to confine the excitation energy within the emission layer to prevent non-radiative losses by contact quenching.

3. Device preparation and characterization

The following sections describe the experimental details of the preparation and characterization of the IOLEDs discussed in chapter 4 and chapter 5. The experimental details of the process development presented in chapter 6 as well as other further measurement techniques are not included in this chapter but will, if necessary, be briefly outlined upon their first appearance.

3.1. device preparation

In case of IOLEDs, all devices were prepared on simple float glass sheets. Cleaning of the substrates was performed in commercial wafer cleaning systems (Fairchild, later Miele) using deionized water combined with alkaline detergents. Possible residual organic contaminations were removed by an oxygen-plasma treatment (10 min, 180 W). For single layer devices and bottom-emitting OLEDs commercial ITO-coated glass substrates (Merck: $15\ \Omega/\text{sq.}$) were applied. These substrates were cleaned according to the described procedure. The oxygen-plasma treatment also led to an increase of the ITO surface workfunction.

The evaporation of the cathode metal and the deposition of the organic layer stack was carried in an ultra-high vacuum (UHV) cluster tool, comprising of several organic molecular beam deposition (OMBD) chambers, which are connected via a UHV transfer system. During this work, the system was upgraded several times. The current system configuration is shown in figure 3.1. Chambers, which were mainly used for this work, are indicated in boldface. Metal deposition was performed by thermal evaporation from resistively heated crucibles at a background pressure of about $1 \cdot 10^{-6}$ mbar. The IOLED cathode structure was defined by a metal shadow mask, which was then removed within the system without breaking the vacuum. Afterwards, the samples were transferred to the corresponding deposition chambers for organic materials. The base pressure within the transfer system was below $1 \cdot 10^{-7}$ mbar. To avoid cross-contamination between the emitter respectively transport materials and the volatile p- and n-dopants, separate chambers were used for p-doping, n-doping and the deposition of emission and transport layers. Stable deposition rates were achieved by evaporating the organic materials from custom-built temperature-controlled effusion cells at crucible temperatures ranging from 70 °C to 250 °C and a base pressure close

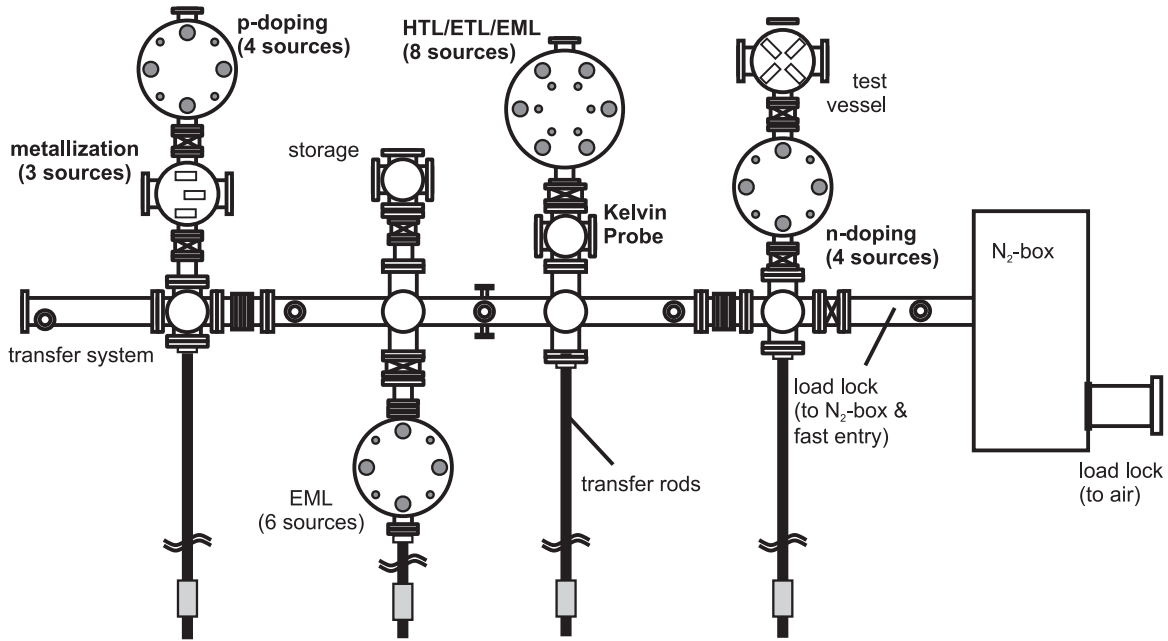


Figure 3.1.: Schematic of the OMBD cluster tool used for the deposition of cathode metals and organic thin films.

to $1 \cdot 10^{-9}$ mbar. All chambers were equipped with multiple monitors for precise rate control and rotating sample holders, guaranteeing uniform thin films. The substrate support was capable of carrying 4 substrates, each $17 \times 17 \text{ mm}^2$ in size. A special shutter geometry allowed to deposit 4 devices with different layer thicknesses or doping concentrations without breaking the vacuum.

For IOLEDs, spin-coating of PEDOT:PSS (Baytron P AI 4083, H. C. Starck) was performed from a filtered aqueous dispersion at 4000 rpm under ambient conditions. The process was repeated 2-4 times until a visibly clear and homogeneous film has been constituted. Prior to radio-frequency (RF) sputtering of the ITO-anode, residual water within the PEDOT:PSS layer was desorbed by storing the samples within the vacuum load lock of the sputtering system. The ITO-anode was sputtered from an 8-inch oxide target (90 % In_2O_3 / 10 % SnO_2 , 99.99 % purity). Sputter-deposition was carried out at room temperature in a pure Ar atmosphere at a pressure of $5 \mu\text{bar}$. The anode geometry was also defined by a metal shadow mask, which was fixed within close distance to the substrate. Further details of the sputtering process can be found in section 6.1.

Due to the low lateral conductivity of the organic layers, electroluminescence is only observed, where the cathode and the anode overlap. The lateral geometry of single IOLED devices was defined by the intersection of a 2 mm wide cathode stripe and a perpendicular

oriented anode stripe (3.1 mm in width), resulting in an active area of 6.2 mm². For single-layer devices and bottom emitting OLEDs, the active area was defined by lithographically patterned openings (diameter: 2 mm) of an insulating photoresist layer. This allows to use the same shadow mask for organic layer and metal cathode deposition, enabling a closed vacuum cycle during device preparation.

3.2. electro-optical characterization

As mentioned, possible applications of OLEDs are lighting and flat panel displays. For these applications, any discussion of device characteristics has to consider the spectral sensitivity of the human eye. Photometric quantities can be derived from the luminous intensity I_v which is related to the radiant intensity I by

$$I_v = \int_0^{\infty} I(\lambda)V(\lambda)d\lambda. \quad (3.1)$$

The luminous function $V(\lambda)$ was defined by the International Commission on Illumination (CIE: Commission Internationale de l'Eclairage) and is based on empirical investigations on the human eye perception. In terms of photometric quantities, the luminance L (unit: cd/m²) is defined as the density of luminous intensity. Assuming Lambertian emission [99,100], the current efficiency η_{phot} (unit: cd/A) and the power efficiency η_{lum} (unit: lm/W) are:

$$\eta_{phot} = \frac{L}{J} \quad \text{and} \quad \eta_{lum} = \frac{\pi L}{UJ}. \quad (3.2)$$

The current efficiency is a measure for how many photons are emitted per injected electron. The power efficiency gives the ratio between the total luminous flux emitted by a device and the total input power. In the following discussions, devices will be compared by means of current efficiency and power efficiency at fixed luminances of 100 cd/m² and 500 cd/m², representing the mean respectively maximum luminance for display applications.

The electro-optical properties of the devices were recorded under ambient conditions using a source measure unit (Keithley 2400) and a large-area Si-photodiode (Advantest TQ 82214) connected to a optical power meter (Advantest TQ 8221). Conversion to photometric quantities was done by careful calibration with a luminance meter (Minolta LS-110). For low-temperature current voltage characteristics, the same setup was used, while keeping the samples within a cryostat. Further, voltage-dependent EL spectra of the devices were

obtained by using a fiber-coupled micro-spectrometer (TecFive MMS UV-VIS II) in combination with the mentioned source measure unit. Software-controlled measurement routines ensured equal measurement conditions throughout the complete period of this work.

4. Phosphorescent IOLEDs

Up to now, inverted organic light emitting diodes employed fluorescent materials [23, 24, 26, 68]. By spin statistics, the singlet to triplet ratio in luminescent materials can be estimated to 1 to 3 [97] and limits the internal quantum efficiency to about 25 % (see sec 2.4.2. Since first reports on electrophosphorescence in OLEDs [101–103], the internal quantum efficiency of bottom-emitting OLEDs was improved to nearly 100 % [104, 105]. Introducing phosphorescent emitter materials to IOLEDs promises a dramatic increase of the devices' efficiency. The following chapter presents a study on highly efficient red, green and blue phosphorescent IOLEDs.

4.1. deposition induced luminescence quenching in phosphorescent IOLEDs

The sputter-deposition of ITO on top of the organic layers is a crucial process during the preparation of inverted OLEDs. It was demonstrated that pentacene or PEDOT:PSS can be used as buffer layer to prevent from sputter-induced damage [24, 26]. In latter case the underlying pentacene layer may act as hydrophobic water barrier, which does not allow water to penetrate the device during spincoating of PEDOT:PSS from an aqueous dispersion. Although the buffer layer absorbs the UV radiation emitted from the plasma and minimizes the harming influence of highly energetic atoms, ions and electrons it does not reduce the heat-related stress onto the organic thin films. In thermally stable device configurations for fluorescent IOLEDs, Alq₃ was employed as electron transporting and emission layer. Highly efficient fluorescent IOLEDs were realized by using TPBI as hole blocking layer [25]. Due to its high triplet energy, TPBI is often used as exciton blocking layer in phosphorescent OLEDs [106, 107]. For realizing phosphorescent IOLEDs, the suitability of those host materials most commonly used in conventional OLEDs has to be evaluated.

Figure 4.1 compares the characteristics of phosphorescent IOLEDs, employing two different carbazol-derivatives as host material doped with the green phosphor emitter Ir(ppy)₃: TCTA and CBP. For a common voltage, the CBP device exhibits a higher current density than the TCTA device. Electrons are often referred as minority carriers in OLEDs. This proposition holds even more for IOLEDs, where less electron injection was measured for bottom metal

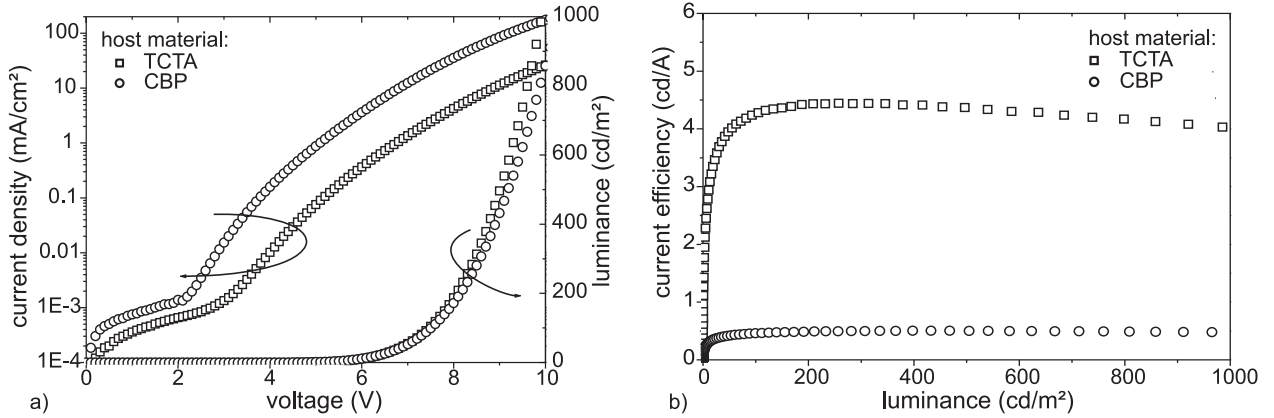


Figure 4.1.: Device characteristics for IOLEDs employing TCTA (squares) or CBP (circles) as host material. a) Current-density and luminance plotted against voltage. b) Current efficiency plotted against luminance. Device structure TCTA (thickness in nm): Al 100\Alq₃ 5\Li 0.6\TPBI 15\TCTA:Ir(ppy)₃ (6.9 %) 25\α-NPD 10\1-TNATA 10\pentacene 20\PEDOT:PSS 30\ITO 90. Device structure CBP (thickness in nm): Al 100\Alq₃ 5\Li 0.6\TPBI 25\CBP:Ir(ppy)₃ (7.1 %) 30\α-NPD 30\1-TNATA 10\pentacene 20\PEDOT:PSS 30\ITO 90.

cathodes compared to top cathodes [25]. Improving the electron injection and transport properties will therefore be reflected in the current density voltage characteristics. At intrinsic organic organic interfaces, only negligible dipole formation has been observed [108]. This observation allows to determine the barrier which electrons or holes have to overcome at the interface between the TPBI ETL and the CBP respectively TCTA HTL by the energy difference of the corresponding LUMO respectively HOMO level. Literature values for the LUMO energies of TPBI, CBP and TCTA [107] yield an electron barrier of 0.4 eV at the TPBI/CBP interface and of 0.7 eV between TPBI and TCTA. This difference may explain the higher current density measured for the CBP device.

In contrast, the comparison of the voltage which has to be applied for a certain luminance reveals very similar values for both devices. At higher brightness levels (> 200 cd/m²) even a lower driving voltage is achieved by the TCTA device. When CBP is substituted by TCTA, the lower current density for a given voltage is compensated by a much higher current efficiency, as displayed in figure 4.1b. Maximum efficiencies of 0.5 cd/A respectively 4.4 cd/A have been measured for the CBP respectively TCTA device. It has been reported, that within CBP:Ir(ppy)₃ systems a reverse energy transfer from the phosphor molecule to the matrix may be responsible for non-radiative losses [109]. Although CBP may not be perfectly suited, current efficiencies of 28 cd/A were achieved using CBP as host material [102]. A difference in the energy transfer rate from the host to the phosphor molecules cannot explain the very low efficiency of the CBP IOLED.

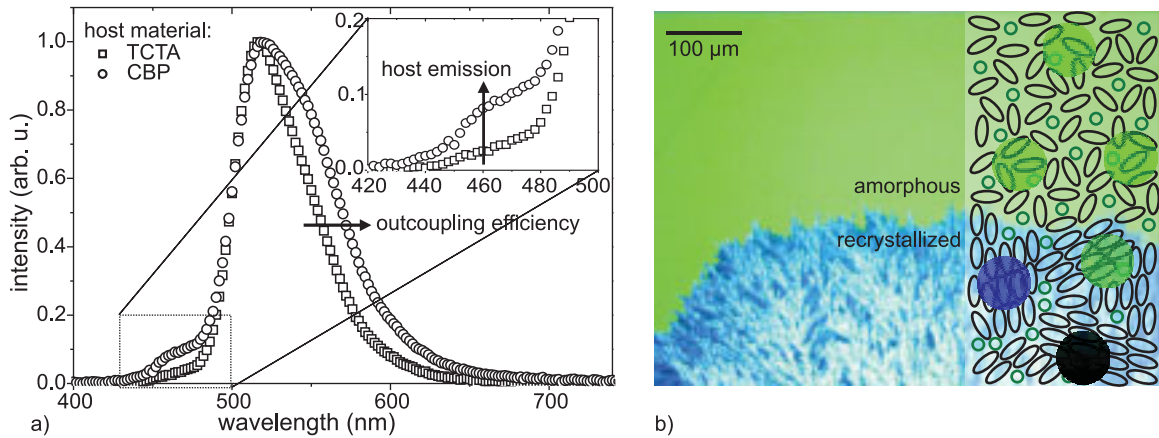


Figure 4.2.: a) EL spectra of phosphorescent IOLEDs employing CBP or TCTA as host material. The inset shows the short wavelength edge of the emission spectra around 460 nm. b) Microscopic image of a 100 nm thin CBP:Ir(ppy)₃ film. Under UV light emission, green PL is observed in the amorphous area, whereas the recrystallized part of the film does not show a significant PL. The inset shows a model schematic. Within the recrystallized thin film, CBP molecules (open ellipses) rearranged to micro-crystals. The phosphor molecules (open circles) accumulate at the grain boundaries. In the amorphous film, host and matrix molecules are randomly distributed. Filled green circles represent phosphor emission, blue transparent circles represent host emission and black circles represent non-radiative decay due to aggregate quenching. The diameter of the filled circles indicates the Dexter radius.

Figure 4.2a shows the EL spectra of both devices. For both devices the peak emission wavelength is about 518 nm and characteristic of the phosphorescent dopant. The broadening in the longer wavelength part of the CBP device's spectrum can be explained by a difference in the transport layers' thicknesses, which by microcavity effects tunes the spectral outcoupling efficiency [110]. A more interesting feature for the discussion of the current efficiency can be observed at the short wavelength edge of the EL spectra around 460 nm (see inset of figure 4.2a). A blue shifted emission feature can be attributed to relaxation of excited CBP molecules or bi-molecular excited states including CBP as participating species. The appearance of an additional feature around 440 nm was observed for low concentrations of Ir(ppy)₃ doped into 3-phenyl-4-(1'-naphthyl)-5-phenyl-1,2,4-triazole (TAZ) [111]. This has been attributed to an insufficient transfer of the triplet energy from host to phosphor molecules, which leads to an increasing host emission, and coincidences with a lower device efficiency. As the doping concentration of the CBP device was 7.1% and close to the efficiency maximum [102], no additional EL feature originating from host molecules would be expected.

But it was observed, that CBP thin films tend to recrystallize under minor thermal stress or even at room-temperature. Figure 4.2b shows a microscopic image of a 100 nm thin CBP film doped with Ir(ppy)₃ after several days of storage under ambient conditions. In the upper part of the image, the film shows a smooth surface and an amorphous thin film is most likely. In the lower part of the image, the thin film recrystallized and does not show a significant PL under UV light illumination. The inset shows a model schematic of the film structure and the possible recombination processes. For conventional OLEDs, the emission layer is expected to be amorphous. A doping concentration of 6 vol.% then results in a mean distance between phosphor molecules, which is small enough, that the Ir(ppy)₃ site lies within the Dexter radius of excited CBP molecules and efficient energy transfer from the host to the lumophore is enabled. This is indicated by filled green circles. For higher doping concentrations the mean distance is reduced and aggregate quenching may occur, thereby reducing the efficiency [112]. For IOLEDs, recrystallization due to elevated temperatures during the sputter-deposition of ITO is most likely. Then, the CBP molecules rearrange in microcrystals and Ir(ppy)₃ molecules accumulate at the grain boundaries. At excitation sites, where lumophores lie beyond the Dexter radius, the energy is not completely transferred to the dopant, but also host emission occurs. Further, aggregate quenching due to the accumulation of Ir(ppy)₃ molecules increases. Both effects lead to a dramatic decline of the luminescence yield. Thus, CBP is not suitable as host material in IOLEDs with sputtered ITO anodes. TCTA thin films exhibit a very stable amorphous structure which is reflected in a comparably high glass transition temperature of about 151 °C [113]. During the experiments, TCTA thin films proved to maintain a disordered morphology upon ITO sputtering and no deposition induced quenching is expected.

4.2. cathode-induced quenching in phosphorescent IOLEDs

Cathode-induced luminescence quenching has been extensively studied in the past and was described by either dissociation of excitons, which diffused to the organic-metal interface or a resonant dipole interaction [114] of the excited molecule with the free electron gas in the metal film. In the latter case, the exciton is seen as a dipole, which induces an image dipole on the metal surface. Then, resonant energy transfer to the image dipole quenches the luminescence. Figure 4.3 displays the influence of the distance between emission layer and metal cathode on the IOLED characteristics. The Alq₃ layer thickness was varied from 5 nm to 15 nm, resulting in a total thickness of the ETL of 25 nm to 35 nm. A slight increase of the driving voltage for a given current density with increasing layer thickness is observed. The

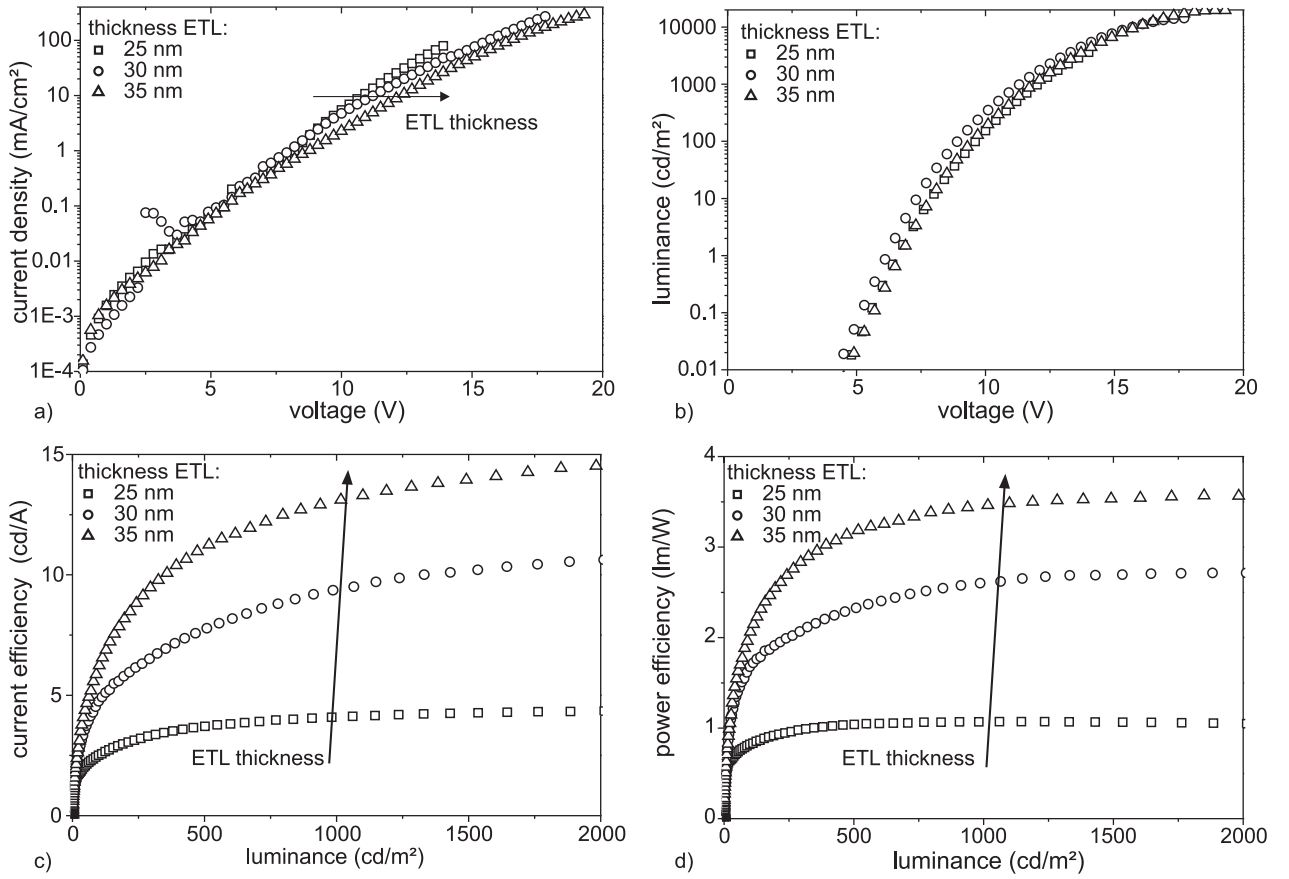


Figure 4.3.: Influence of the ETL thickness on the device characteristics of phosphorescent IOLEDs. a) Current density plotted against voltage. b) luminance plotted against voltage. c) current efficiency plotted against luminance. d) power efficiency plotted against luminance. Device structures (thickness in nm): Al 100\Alq₃ 5\Li 0.6\Alq₃ 5 (squares), 10 (circles), 15 (triangles)\TPBI 15\TCTA:Ir(ppy)₃ (10.4 %) 25\α-NPD 10\1-TNATA 10\pentacene 20\PEDOT:PSS 30\ITO 90.

EL onset voltage is independent of ETL thickness and equals 4.5 V. For lower voltages than the EL onset voltage a small leakage current is visible. As the influence of the leakage current vanishes for higher driving levels, the maximum efficiencies were measured at relatively high brightness levels. The current efficiency drastically increases with growing ETL thickness. At a brightness level of 1000 cd/m² current efficiencies of 4.1 cd/A, 9.4 cd/A and 13.1 cd/A were measured for an ETL thickness of 25 nm, 30 nm and 35 nm, respectively. This is also reflected by the power efficiency plot. As the generated excitons are confined within the EML by the TPBI HBL, exciton diffusion to, and dissociation at the metal/organic interface can be excluded. Therefore, the presented data is a clear evidence for a non-radiative coulomb interaction of the excited state and a counter-dipole within the metal cathode. As the

transfer rate has a cubic dependence on the metal-exciton-distance [115], cathode quenching will be negligible for thicker electron transport layers.

4.3. multicolor IOLED stack

Section 6.3 discusses the micro-patterning of organic materials for full color OLED displays. It can be anticipated, that a common IOLED structure, in which the emission color is determined by a simple substitution of the EML, is favored for reasons of a simpler process handling and less material consumption. In the previous section, the phosphorescent heavy metal complex Ir(ppy)_3 serves as archetypal emitter molecule for green phosphorescent IOLEDs. Conventional OLEDs, employing the red emitting dopant $\text{btp}_2\text{Ir(acac)}$ doped into CBP, reached an external quantum efficiency of about 7 % and exhibited a smaller efficiency roll-off at high currents [106] compared to the Pt-complex 2,3,7,8,12,13,17,18-octaethyl-12H,23H-porphin platinum (II) OtOEP [101, 116]. Efficient blue organic electrophosphorescence was achieved by doping FIrpic into different carbazol-derivatives [117–119]. As discussed before, CBP will not be suitable as host material for phosphorescent IOLEDs. Further it has been demonstrated that the triplet energy of CBP is slightly below the Triplet energy of FIrpic. Therefore, TCTA will also be applied as host material for the red and the blue phosphor dopant.

Figure 4.4 summarizes the device characteristics of three IOLEDs, in which only the phosphor dopant was substituted to achieve red, green and blue emission. The driving voltage which has to be applied for a luminance of 500 cd/m^2 is 12.0 V for the red IOLED, 10.6 V for the green IOLED and 9.1 V for the blue IOLED. It has been reported, that Ir(ppy)_3 molecules doped into TCTA thin films represent hole trapping sites, which decrease the drift mobility. This leads to an increasing driving voltage with increasing doping concentration [25]. This becomes clear, when the HOMO levels of TCTA (5.9 eV [107]) and Ir(ppy)_3 (5.6 eV [120]) are compared. The picture of dopant induced traps in the TCTA layer can also be applied to discuss the observed difference in driving voltage, when the phosphor dopant is substituted. The HOMO level of FIrpic was reported to be 6.0 eV [121, 122]. Compared to the HOMO level of TCTA (5.9 eV), dopant trapping of holes is not likely. This assumption is confirmed by a lower driving voltage of the blue IOLED compared to the Ir(ppy)_3 device. For $\text{btp}_2\text{Ir(acac)}$ a HOMO level of 5.1 eV was measured by UV photoelectron spectroscopy [122]. When doped into TCTA, $\text{btp}_2\text{Ir(acac)}$ molecules act as deep lying traps within the HOMO-LUMO gap of the host. This coincidences with the highest driving voltage observed.

Although a common IOLED architecture with identical layer thicknesses for all colors was

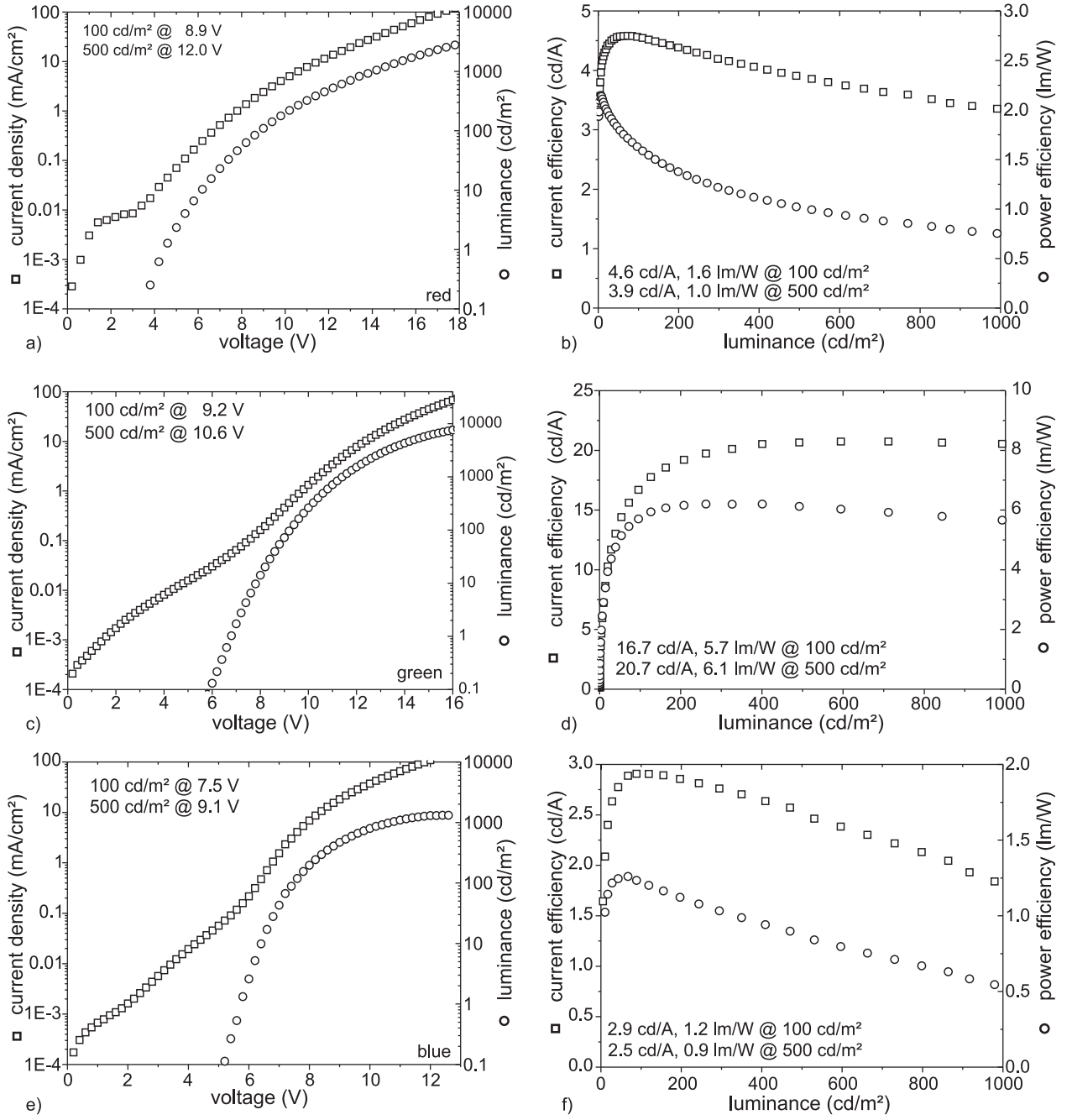


Figure 4.4.: Device characteristics of a) b) red, c) d) green and e) f) blue phosphorescent IOLEDs. a) c) e) Current density (squares) and luminance (circles) plotted against voltage. b) d) f) Current efficiency (squares) and power efficiency (circles) plotted against luminance. Device structures (thickness in nm): Al 100\LiF 0.5\Al 0.3\Alq₃ 5\TPBI 35\TCTA:dopant 10\α-NPD 5\1-TNATA 5\pentacene 20\PEDOT:PSS 30\ITO 90. The doping concentration (by volume) was 6.7 % btp₂Ir(acac) for red, 7.0 % Ir(ppy)₃ for green and 6.0 % FIrpic for blue emission.

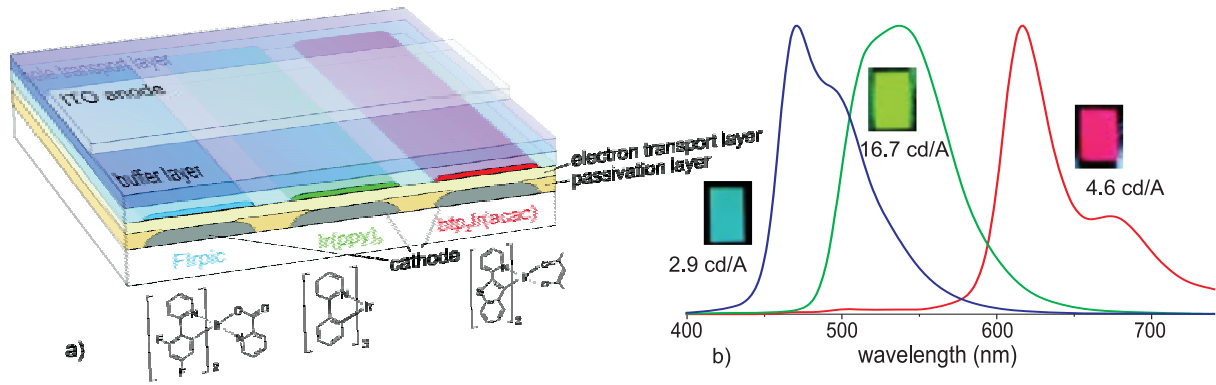


Figure 4.5.: a) Cross-sectional schematic of a multicolor IOLED-pixel. Common transport layers and common anode simplifies the processing. The EML can be deposited via LILT (see section 6.3. b) EL spectra of a red, green and blue IOLED. The insets show images of the EL of the corresponding devices.

used, reasonably high efficiencies were achieved. At 100 cd/m^2 the current efficiency was measured to 4.6 cd/A for red, 16.7 cd/A for green and 2.9 cd/A for blue emission. Due to leakage currents, the efficiency for the green device rises further to 20.7 cd/A at a luminance level of 500 cd/m^2 , whereas the efficiency of the red and blue devices show a decrease for with increasing luminance. The observed roll-off is attributed to increasing T-T-annihilation, which was reported to occur at higher current densities [106]. In agreement with the spectral response of the human eye, which is most sensitive around 550 nm , the green IOLED is most efficient. Characteristic values of the discussed devices are summarized in Table 4.1.

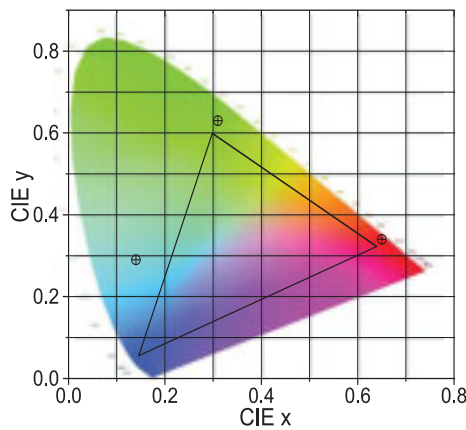


Figure 4.6.: CIE color chart. The coordinates of the presented IOLEDs are marked with crossed circles. The triangle represents the color space defined by the sRGB standard.

The emission spectra of the three devices are presented in figure 4.5. The EL spectra of the red emitting IOLED reaches its maximum intensity at an emission wavelength of 617 nm and a further characteristic feature at 672 nm. This translates to a saturated red with CIE color coordinates of $x = 0.65$ and $y = 0.34$. The green IOLED's spectrum peaks at 537 nm at, giving CIE coordinates of $x = 0.31$ and $y = 0.63$. The blue spectrum reflects the characteristic spectrum of FIrpic, exhibiting an intensity maximum at 471 nm and a further shoulder on the longer wavelength edge around 490 nm. The color impression is not very saturated and converts into CIE coordinates of $x = 0.14$ and $y = 0.29$. The color coordinates of the three spectra are indicated within a CIE color chart, displayed in figure 4.6.

Also indicated in figure 4.6 is the color space defined by the sRGB standard, which is accepted for a wide range of applications ¹. It shows, that the red and green IOLEDs' emission spectra satisfies the sRGB standard very well. The tone of the blue IOLED is not very saturated and is described best as sky blue. Therefore it is not surprising, that the color coordinate does not fit the sRGB color space very well. This mismatch, results in a smaller color gamut for the presented multicolor architecture than demanded by the sRGB standard. Currently great efforts are carried out, to develop stable deep blue phosphorescent emitter molecules and suitable wide band gap hosts [123–125]. First promising results for true blue emitting phosphorescent OLEDs have been published recently [126]. In the near future, these materials may also be applied for inverted OLEDs to enhance the color gamut covered by the multicolor IOLED architecture.

Table 4.1.: Characteristic values of IOLEDs employing different emitter materials: Bias V_b for a luminance of 500 cd/m², current efficiency η_c at 500 cd/m² and maximum value, power efficiency η_P at 500 cd/m² and maximum value, maximum luminance L .

dopant	V_b (V) 500 cd/m ²	η_c (cd/A) 500 cd/m ²	η_c (cd/A) max.	η_P (lm/W) 500 cd/m ²	η_P (lm/W) max.	L (cd/m ²) max.
btp ₂ Ir(acac)	12.0	3.9	4.6	1.0	2.1	2900
Ir(ppy) ₃	10.6	20.7	20.7	6.1	6.2	9200
FIrpic	9.1	2.5	2.9	0.9	1.3	1300

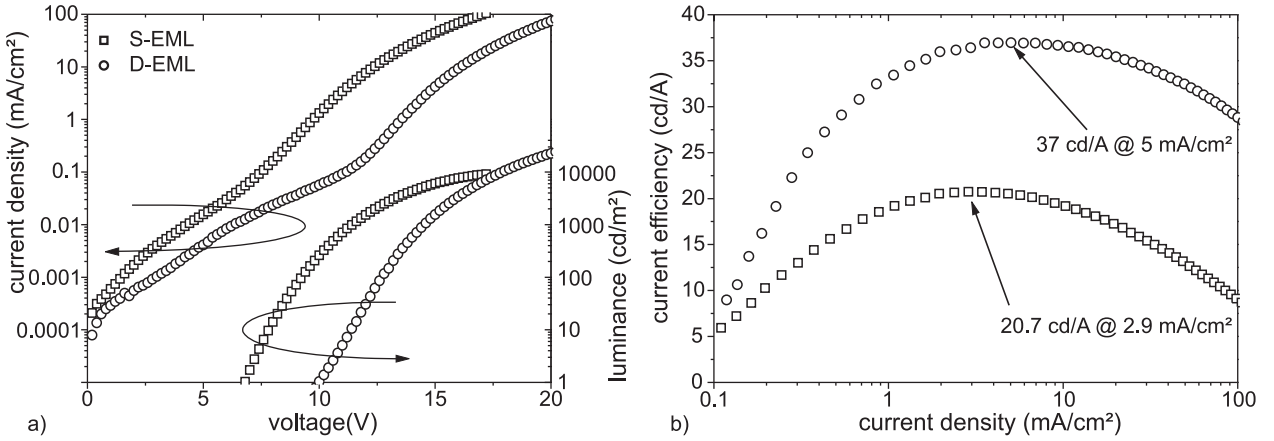


Figure 4.7.: Comparison of IOLEDs with S-EML (squares) or D-EML (circles). a) Current density and luminance plotted against voltage. b) Current efficiency plotted against current density. Device structure S-EML (thickness in nm): Al 100\LiF 0.5\Al 0.3\Alq₃ 5\TPBI 35\TCTA:Ir(ppy)₃ 10\α-NPD 5\1-TNATA 5\pentacene 20\PEDOT:PSS 30\ITO 90. Device Structure D-EML: Al 100\LiF 0.5\Al 0.3\Alq₃ 5\TPBI 30\TPBI:Ir(ppy)₃ 10\TCTA:Ir(ppy)₃ 10\α-NPD 5\1-TNATA 5\pentacene 20\PEDOT:PSS 30\ITO 90.

4.4. influence of interfacial exciplex states

For conventional green emitting OLEDs the internal quantum efficiency nearly reached the theoretical limit of 100 % [105]. The so far reported values for the current efficiency of IOLEDs cannot compete with those values published for conventional OLEDs. Recently, a significant increase in current efficiency was observed, when dual emitting layers (D-EML) were employed [127]. In this context, the term "dual emitting layers" describes a phospho-

¹Proposed in 1996 by Microsoft and Hewlett Packard, the sRGB standard developed into a widely accepted standard for computer and printing applications and is filed under IEC 61966-2-1.

Table 4.2.: Characteristic values of IOLEDs employing different emitter systems: Bias V_b for a luminance of 500 cd/m², current efficiency η_c at 500 cd/m² and maximum value, power efficiency η_P at 500 cd/m² and maximum value, maximum luminance L .

EML	V_b (V) 500 cd/m ²	η_c (cd/A) 500 cd/m ²	η_c (cd/A) max.	η_P (lm/W) 500 cd/m ²	η_P (lm/W) max.	L (cd/m ²) max.
S-EML	10.6	20.7	20.7	6.1	6.2	9200
D-EML	13.9	34.9	37.0	7.9	8.0	50000

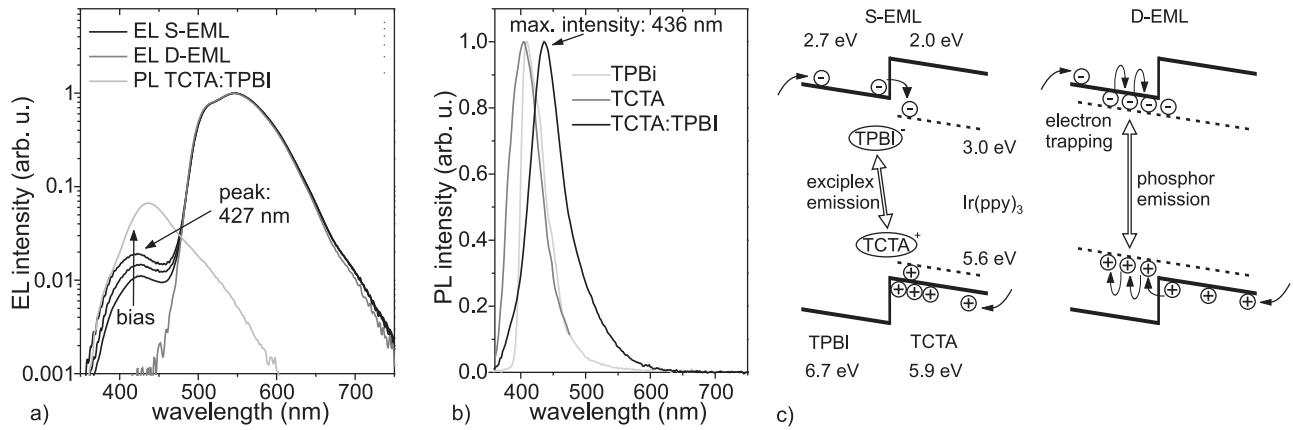


Figure 4.8.: Visible exciplex feature in a) EL spectrum of a S-EML IOLED and b) PL spectra of a co-evaporated TPBI:TCTA thin film. c) Energy level alignment at TPBI/TCTA interface for a S-EML and a D-EML. Values for HOMO and LUMO levels of the materials are indicated in the figure. The dashed line displays the position of the HOMO and LUMO levels of Ir(ppy)₃.

rescent emitter system, in which the phosphor is doped into two separate, but neighboring layers. One of these layers shows electron transporting properties, the other one exhibits a hole transporting nature. In this configuration, the recombination is located at the interface between electron transporting and hole transporting host. It was tested, if this approach, also leads to an increased current efficiency in IOLEDs. Figure 4.7 displays a comparison between an IOLED with a single emission layer (S-EML) and a device employing a D-EML. Characteristic values for both devices are given in table 4.2.

At first sight, a dramatic increase in current efficiency of nearly 80% strikes the eye. The maximum current efficiency for the S-EML device is measured at 2.9 mA/cm² to be 20.7 cd/A. The D-EML device yields a maximum current efficiency of 37 cd/A at a current density of 5.0 mA/cm². When the power efficiencies are compared, still, the D-EML (8.0 lm/W) yields a higher efficiency than the S-EML (6.2 lm/W), but the increase is put into perspective, by an increased driving voltage for the D-EML device. The cited report quotes the diffusion of triplet excitons into the undoped transport layers as a possible non-radiative decay path in the S-EML device, as the emission spectrum of the S-EML devices featured a further peak around 450 nm, [127]. Figure 4.8a plots the EL spectra of the discussed S-EML and D-EML devices in a logarithmic scale. In case of the S-EML an additional EL feature arises, peaking at 427 nm. As indicated in the figure, this feature rises, when the applied bias is increased. If the suggestion of exciton diffusion into the undoped HBL is valid, the additional feature in the EL spectra has to be assigned to TPBI. PL spectra of neat TPBI

and TCTA films and a mixed TPBI:TCTA thin film are shown in figure 4.8b. TPBI reveals a relatively narrow spectrum, which peaks at 410 nm. Due to the peak wavelength discrepancy, exciton diffusion into the HBL can be excluded. The PL maximum of the neat TCTA film is measured at 404 nm. When the spectrum of the mixed TPBI:TCTA thin film, which peaks at 436 nm, is compared to those of the neat films, it becomes clear, that it cannot be reproduced by a superposition of latter ones. In contrast, the absorption spectrum of the mixed film does represent a superposition of the absorption spectra of the neat films (not shown here). Both observations can be explained by the presence of exciplexes (excited complex) in the mixed film. Due to the large difference in the HOMO and LUMO levels of TPBI and TCTA, it is energetically favorable, that upon excitation electrons occupy TPBI LUMO states and holes occupy TCTA HOMO states. This leaves TPBI molecules negatively and TCTA molecules positively charged. According to the following sum formula, coulomb attraction leads to the formation of a new species.



After relaxation, the participating molecules dissociate to their isolated ground state. As given by name, exciplexes appear only in the excited state. The exciplex emission spectrum is expected to be redshifted relative to the isolated spectra of the participating molecular species.

Returning to figure 4.8b, the mixed film's emission spectra perfectly complies with the exciplex model. The exciplex PL spectra is also displayed in figure 4.8a, which, by comparison with the blue feature in the EL spectrum of the S-EML devices, leads to the conclusion, that an interfacial exciplex between the TPBI HBL and the TCTA EML (doped with Ir(ppy)₃) must be present. Such interfacial exciplexes are well known in fluorescent OLEDs [128–130], which in most cases lower the devices' efficiency.

For phosphorescent IOLEDs, the presented data suggests a different interpretation than given by literature [127]. This is illustrated by figure 4.8c. The figure shows the energy level alignment at the interface, which was constructed according to literature values for the HOMO and LUMO levels of TPBI, TCTA [107] and Ir(ppy)₃ [120]. Holes are injected into the phosphor-doped TCTA layer and drift towards the interface. As mentioned before, the electron current is expected to be the limiting factor. Following, holes accumulate next to the TPBI/TCTA interface, leading to a high density of positively charged TCTA molecules. If an electron encounters the interface, it may be transferred to an Ir(ppy)₃ molecule, or possibly lead to the formation of an excited complex. The latter case is indicated and increases the non-radiative losses. The ratio of electrons transferred to phosphor molecules and those participating in exciplex formation determines the device efficiency. With increasing bias,

more holes are accumulated and the probability for exciplex formation is increased. This suggestion complies with the observed increase in exciplex emission with increasing bias. For the D-EML device, no exciplex emission is observed. Therefore, the accumulation of holes at the interface seems to be negligible. Holes are expected to penetrate the phosphor doped TPBI layer via hopping between dopant trap states [124]. Under these circumstances, the recombination zone is shifted into the TPBI layer, preventing from any type of interfacial exciplex. This leads to the observed increase in current efficiency. The drawback which has to be accepted is, that obviously, the presence of phosphor molecules do not only enable hole transport within the electron transporting host, but also represent effective trap sites for the electron transport, which lead to the observed driving voltage increase (see figure 4.7a). In conclusion the use of D-EML in IOLEDs suppresses the formation of interfacial exciplexes and enables efficiencies comparable to those measured for conventional OLEDs.

4.5. highly efficient IOLEDs with doped injection layers

The presented D-EML approach enables an increased current efficiency, but at the same time limits the increase in power efficiency due to a higher driving voltage. Doping of the transport layers with suitable accepting or donating species lowers the driving voltage of conventional OLEDs significantly [80, 81, 85, 131]. In the so far discussed inverted OLED architecture, the use of the polymeric conductor PEDOT:PSS leads to a very small hole injection barrier of about 0.25 eV, which drastically improves the hole injection current in single carrier devices [74, 75]. Further evidence for ohmic charge injection from PEDOT:PSS into pentacene was found by investigations on single carrier devices with top-anode [25]. At the cathode, the metal organic interface is modified by a LiF-Al bilayer which reduces the injection barrier by 0.15 eV (see section 2.3.1). Nevertheless, the electron injection and transport seems to be the limiting factor for achieving lower driving voltages (see section 4.4). It has been demonstrated, that Li-doping drastically improves the charge injection into the ETL and the bulk conductivity itself of doped ETLs [86]. In conventional OLEDs, very low driving voltages were achieved by applying Li-doped ETLs [85, 92]. In reference [25] the benefit of alkali-metal doped ETLs with respect to its application in IOLEDs is discussed. It was found, that quasi-ohmic charge injection even from high work function electrodes (e.g. Au, ITO) is possible. The term "quasi-ohmic" refers to tunnel injection through a very narrow -and for this reason transparent- tunnel barrier at the metal organic interface.

Under these preconditions, highly efficient IOLEDs with D-EML, employing a highly reflective Ag cathode and a 40 nm thick Li-doped ETL were fabricated. Such a device is characterized in figure 4.9, which also contains the characteristics of an IOLED with an

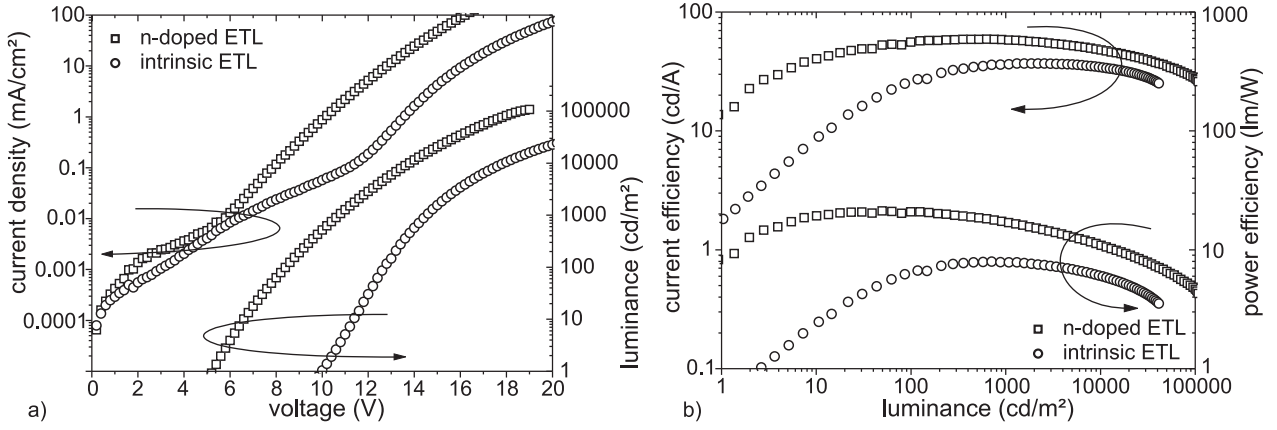


Figure 4.9.: Device characteristics of highly efficient IOLEDs for which either a Li-doped BPhen ETL (squares) or an intrinsic TPBI ETL (circles) was employed. a) Current density against and luminance against voltage. b) Current efficiency and power efficiency against luminance. Device structure intrinsic ETL (thickness in nm): Ag 100\LiF 0.5\Al 0.3\Alq₃ 5\TPBI 35\TCTA:Ir(ppy)₃ 10\α-NPD 5\1-TNATA 5\pentacene 20\PEDOT:PSS 30\ITO 90. Device Structure n-doped ETL: Al 50\BPhen:Li 40\TPBI 10\TPBI:Ir(ppy)₃ 10\TCTA:Ir(ppy)₃ 10\α-NPD 5\1-TNATA 10\pentacene 20\PEDOT:PSS 30\ITO 90.

intrinsic ETL². Characteristic values for both devices are listed in table 4.3. As expected, the driving voltage for a brightness level of 500 cd/m² was lowered by 3.9 V to 10.0 V. This means that the complete AM operation regime can be addressed by voltages lower than 10 V. Further the current efficiency increased to a maximum of 59.2 cd/A, measured at a luminance

²The term intrinsic refers to the fact, that the ETL was not intentionally doped during the deposition. It was reported, that by using LiF/Al bilayers in conventional OLEDs, Li atoms diffused into the ETL upon a dissociative chemical reaction of LiF, Al and the ETL [54]. The results for LiF/Al bottom electrodes presented in section 2.3.1 suggest, that in case of LiF containing bottom cathodes, an unintentional doping of the ETL cannot be excluded.

Table 4.3.: Characteristic values of IOLEDs employing either an intrinsic or n-doped ETL: Bias V_b for a luminance of 500 cd/m², current efficiency η_c at 500 cd/m² and maximum value, power efficiency η_P at 500 cd/m² and maximum value, maximum luminance L .

ETL	V_b (V) 500 cd/m ²	η_c (cd/A) 500 cd/m ²	η_c (cd/A) max.	η_P (lm/W) 500 cd/m ²	η_P (lm/W) max.	L (cd/m ²) max.
intrinsic ETL	13.9	34.9	37.0	7.9	8.0	50000
n-doped ETL	10.0	59.1	59.2	18.6	21.2	107000

of 630 cd/m². The corresponding value for the device with intrinsic ETL is 37.0 cd/A. The increase in current efficiency can either be explained by a more balanced charge injection, or by a higher outcoupling efficiency for devices with Ag cathode. A more balanced charge injection leads to less leakage current and lower electric fields across the emission layer and the interfaces next to the EML, which in turn may lead to field-induced phosphorescence quenching [132]. Numerical simulations for top-emitting devices with different semitransparent metal films employed as top cathodes showed, that the light outcoupling ratio increases by a factor of 2.5, when Al is substituted by Ag [133]. Although the device structure which was employed for the simulation, significantly differs from the IOLED device structure used in this work, it is self-evident, that the higher reflectivity of the Ag cathode leads to an improved outcoupling factor ³. It is most likely, that both effects account for the observed increase in current efficiency. The low driving voltage in addition to a high current density allows a maximum power efficiency of 21.2 lm/W. At a driving voltage of 19 V, a maximum luminance of more than 100000 cd/m² is obtained.

³The reflectivity of commercial Ag coatings is 98 % for wavelengths bigger than 500 nm. Al coatings exhibit a reflectivity of about 90 % throughout the visible spectrum.

5. The stacking approach

Recently, charge carrier separation at organic/inorganic or organic/organic interfaces within stacked organic light emitting diodes (OLEDs) has been observed and aroused a lot of interest because of its potential to dramatically enhance the quantum efficiency of OLEDs. Within stacked OLEDs two or more emission layers are interconnected by introducing thin metal interlayers [112] or by employing so-called charge generation layers (CGLs) [95, 134–141]. Several different CGL architectures have been proposed, but in all cases they consisted either of doped organic/inorganic layer sequences [95, 134–139] or doped organic/organic p-n junctions [140, 141]. The major research focus was laid onto realizing highly efficient or white light emitting devices for lighting applications. By stacking of several OLEDs the current efficiency scales with the numbers of stacked emission units (EMU). As the driving voltage for a given brightness is also multiplied by the number of emission units, the power efficiency should - in principle - not be affected by stacking of OLEDs. For lighting applications this means a major advantage, as now the current density for a given driving voltage can be reduced drastically. This enables longer device lifetimes and larger panels, as the current density in relation to the resistance of the ITO anode defines the upper limit for the maximum panel size.

But where is the advantage for display applications? For PM-OLED displays the increase in driving voltage would lead to an increase in idle and loss power, which is caused by charging and discharging of the parasitic capacity along the anode and cathode lines and higher loss currents due to a higher suppression bias. For AM-OLED displays the situation is different. As not only resistive losses within the OLED device have to be taken into account but also within the underlying driving circuit, a reduction of the driving current could lead to a higher overall AM-OLED display efficiency. Assuming that the AM-backplane's power consumption is proportional to the driving current and makes up about 50 % of the display consumption (backplane + IOLED), a reduction of the driving current to 50 % by employing a stacked IOLED with 2 EMUs, would lead to a overall power reduction of 25 % for the AMOLED display. Expecting a higher overall power efficiency and a longer device lifetime, stacking of IOLEDs for AM-OLED displays is therefore a very promising subject for research and will be discussed in detail.

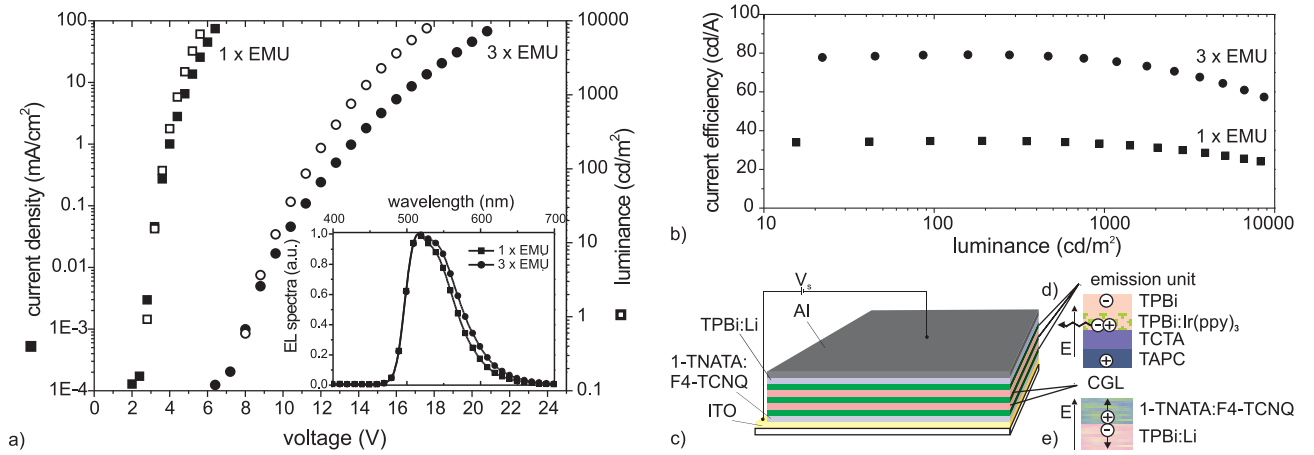


Figure 5.1.: Characteristics and schematic for a stacked OLED. a) L-I-V-characteristics for a conventional OLED having one EMU (squares) compared to a stacked OLED with three EMUs (circles). b) Current efficiency vs. luminance for a conventional OLED having one EMU (squares) compared to a stacked OLED with three EMUs (circles). c) Schematic of a stacked OLED consisting of three EMUs connected by two CGLs. d) Schematic of a single emission unit: injected electrons and holes are transported to the recombination zone and recombine to excitons, which decay radiatively. e) Schematic of a CGL-structure: Electrons and holes separate upon the application of an external electric field and can be injected into the neighboring EMUs.

5.1. stacked organic light emitting diodes

Figure 5.1 shows a comparison of a conventional OLED having one emission unit and a stacked OLED employing three EMUs connected by organic/organic p-n junctions serving as charge generation layers. The device structure of the stacked OLED is depicted schematically in figures 5.1c to 5.1e. Both devices were prepared on commercial ITO substrates. For the single EMU device, the structure consisted of 40 nm of F₄-TCNQ doped 1-TNATA as hole injection layer, one EMU and 40 nm of Li-doped TPBI as electron injection layer. The stacked device employs the same 40 nm thick hole and electron injection layers, but three EMUs which are interconnected by two CGLs. A single EMU comprises 10 nm of TAPC and 10 nm of TCTA as hole transporting layers, 10 nm of TPBI doped with Ir(ppy)₃ as emission layer and a 10 nm thin hole-blocking, electron-transporting layer (TPBI). The CGL structure consists of a F₄-TCNQ doped 1-TNATA layer and a Li-doped TPBI layer, which are both 40 nm in thickness. For both devices a 200 nm thick Al layer serves as cathode. The L-I-V characteristics show, that for a given luminance the driving voltage and current efficiency

nearly triples, indicating an efficient charge generation at the TPBI:Li / 1-TNATA:F₄-TCNQ interface. The improvement factor in current efficiency is slightly smaller than the number of EMUs. As can be derived from the emission spectrum of the two devices, micro-cavity effects may cause the lower than expected efficiency [139].

It has to be pointed out, that the improvement in current efficiency in these devices can only be explained by additional pairs of charge carriers separated within the CGL unit as shown in figure 5.1e. Then electron and hole carriers are injected into the neighboring EMU where they recombine with the corresponding opposite charge carrier (see figure 5.1d). The latter ones are injected either from another CGL or from the electrodes, if the EMU is next to the anode or to the cathode. If no charge carriers were generated at the p-n junction, there would be no improvement in the current efficiency, as injected electron-hole pairs can only recombine once. Furthermore, high injection barriers at the organic heterointerfaces and transport barriers resulting from electrons passing mainly hole transporting layers (HTL) and holes passing mainly electron transporting layers (ETL) would lead to a drastic increase in the driving voltage, as has been observed for a stacked OLED in which no CGL layers were applied [140]. Summarizing the presented results and the results of other groups published so far, field-assisted charge carrier generation at doped organic/organic or organic/inorganic interfaces is evident and essential for stacking of OLEDs [137].

5.2. field-induced charge separation at doped organic/organic heterointerfaces

So far, the understanding of the charge separation mechanism in CGLs is very limited. Tsutsui *et al.* proposed a model for charge carrier separation at the interface between Mg-doped tris(8-quinolinolato) aluminum(III) (Alq₃) and V₂O₅ thin films [137, 138]. By low temperature capacitance measurements they proofed a temperature dependence of the described charge carrier separation and attributed this dependence to thermally activated electron transport via defect states within the V₂O₅-layer. This process leaves a hole carrier within the valence band of the metal oxide, which drifts under the influence of the applied bias towards the cathode [138]. Although other metal oxides were not tested, this model may be applied to other kinds of CGLs consisting of doped organic/metal oxide interfaces. As this model incorporates the presence of a broad distribution of deposition induced defect states within the metal oxide layer, it may not fit to CGLs consisting of doped organic/organic p-n junctions. For latter ones, Law and co-workers performed ultra-violet photoelectron spectroscopy (UPS) on CGL structures consisting of Mg-doped Alq₃ and tetrafluorotetracyanoquinodimethane (F₄-TCNQ) doped 4,4',4''-tris(*N*-3-methylphenyl-

N-phenylamino)-triphenylamine (m-MTDATA) thin films, revealing a large energy shift at the interface due to the presence of a large space charge density. [141] Proceeding, the authors referred to the model proposed by Tsutsui *et al.* [138] leaving the mechanism occurring at the interface unclear and piece to further investigation. The following paragraphs display a more detailed study on organic/organic CGL structures based on F₄-TCNQ doped 1-TNATA and Li-doped TPBI.

5.2.1. doping profile

Organic/inorganic CGLs consist of a donor-doped electron transporting layer and a thermally evaporated metal oxide layer. In this case, the field-assisted charge transfer from occupied valence band states of the metal oxide to LUMO states of the electron transporting layer was identified as mechanism for charge separation under reverse bias [138]. Because no significant hole injection barrier between metal oxide and HTL is present, p-doping of the HTL was not necessary. For organic/organic interfaces, it has not been evaluated yet, if and how different doping schemes at the organic heterojunction affect the efficiency of charge carrier generation. For this reason, CGL samples, having either a doped p-n junction, a partially doped p-n junction or an intrinsic p-n junction, were prepared. In this context the term p-n junction refers to the heterointerface between hole transporting and electron transporting layer. Detailed information on the device structures and layer thicknesses are given in figure 5.2b. For all devices the overall thickness of doped and intrinsic films is kept constant. Figure 5.2a shows the I-V-characteristics for these devices. Devices B and D show very similar characteristics and display the lowest current densities and a rectification ratio of more than three orders of magnitude. In both devices an intrinsic ETL can be found at the interface. In device C an intrinsic HTL and an n-doped ETL establish the p-n junction. Compared to the forward current a 30 times smaller reverse current is measured resulting in an asymmetric I-V-characteristic. Only for device A, which represents doped hole and doped electron transporting layers adjacent to the p-n interface, a symmetric I-V characteristic is observed. Under reverse bias (negative voltage) charge injection and recombination or unipolar charge transport can be neglected due to high injection and transport barriers [137]. Therefore, the obtained data suggests that charge generation and extraction into the contacts under reverse bias is as efficient as charge injection and recombination under forward bias.

The symmetry of the I-V-characteristic of CGL-structures can be taken as an indicator for

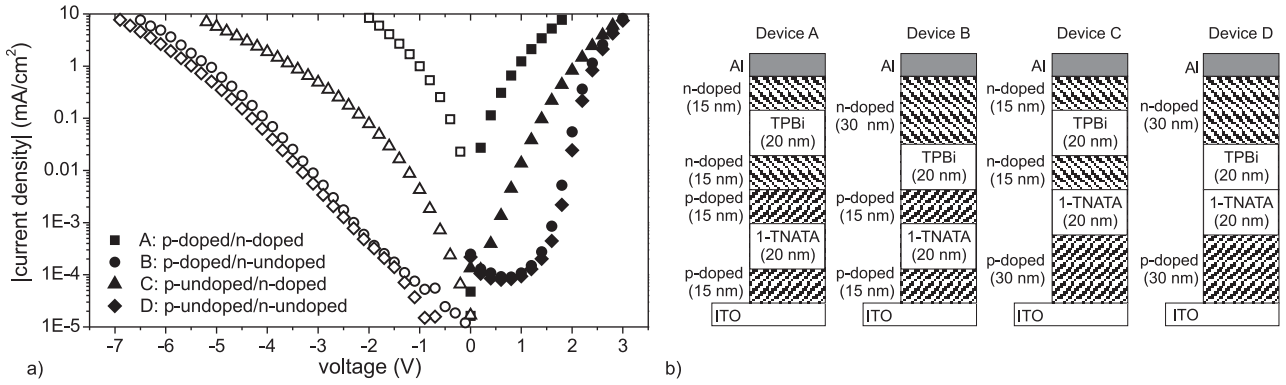


Figure 5.2.: a) I-V-characteristics and b) schematic for p-doped/n-doped (squares), p-doped/n-undoped (circles), p-undoped/n-doped (triangles), p-undoped/n-undoped (diamonds) interfaces. Positive voltage corresponds to ITO electrode biased positively (closed symbols), negative voltage corresponds to Al electrode biased positively (open symbols). b) Schematic of the devices' layer sequence.

the efficiency of charge generation at the p-n interface. As for device C an asymmetric characteristic is observed and devices B and D exhibit a rectifying behavior, it has to be recorded, that for efficient charge generation both - the ETL and the HTL - have to be doped (device A).

5.2.2. low temperatures

Further investigations on the thermal dependence of the CGL architecture proposed in this work were conducted on simple CGL samples, comprising of a F₄-TCNQ doped 1-TNATA film and a Li-doped TPBi layer, both 50 nm in thickness, deposited onto an ITO substrate and capped with 100 nm of Al as top electrode. Temperature dependent I-V-characteristics of this device are shown in figure 5.3.

Upon applying a positive voltage to the ITO electrode charge carriers are injected at both electrodes and transported to the p-n interface where they recombine. A common model for charge injection from metallic contacts into n- or p-doped organic semiconductors describes tunneling of charge carriers through a narrow space charge region at the interface [47, 82]. Unlike the Richardson-Schottky (RS) model, which gives a good approximation for charge injection into intrinsic organic semiconductors [47] and assumes thermally activated hopping over the injection barrier, no explicit temperature dependence is expected for the Fowler-

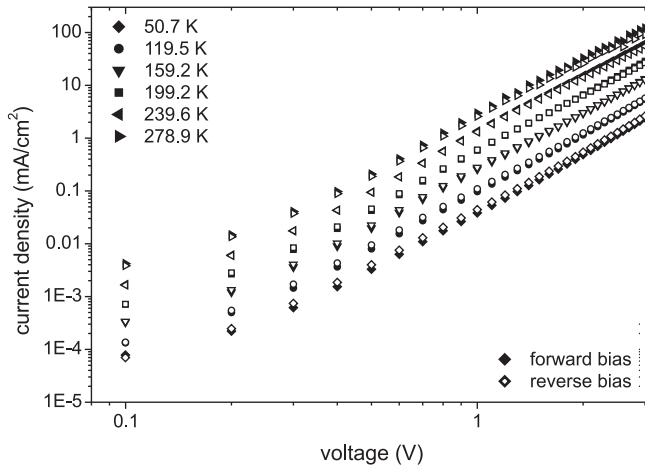


Figure 5.3.: Temperature-dependent I-V-characteristics of a CGL-sample. Forward bias corresponds to positive voltage applied to the ITO electrode (closed symbols), reverse bias corresponds to positive voltage applied to the Al electrode (open symbols).

Nordheim (FN) tunneling mechanism. We assume that the recombination of electrons and holes at the interface is independent of temperature within the observed temperature range. Due to the structural disorder of the organic thin films and only weak intermolecular coupling, the charge transport in organic solids is often described as thermally activated hopping of localized charge carriers. The temperature dependence of the forward characteristic is attributed to a lower carrier mobility for lower temperatures.

Under reverse bias the device shows the same current density for a given temperature and voltage leading to symmetric I-V-characteristics for all temperatures within the given range. Considering, that the temperature dependence of the hopping mobility will affect the reverse current in the same way as it affects the forward current and that the symmetry in the I-V-characteristic is maintained for all temperatures, the charge carrier separation must be independent of temperature. Therefore, a temperature dependence of the charge separating mechanism as reported for organic/inorganic CGL-architectures [138] can not be observed for organic/organic CGLs. Thus a field-only driven mechanism is most likely.

5.2.3. thickness dependence

The dependence of the electrical properties of CGL structures on the thickness of the doped regimes adjacent to the p-n heterojunction will be discussed next. For this reason CGL samples with different thicknesses of the doped layers have been prepared. As displayed in the inset of figure 5.4d, the thickness of the doped layers adjacent to the p-n interface can be adjusted by shifting the position of an undoped ETL (TPBI) or HTL (1-TNATA) without changing the ratio of the doped layers' thickness compared to the total device thickness. This means that a change in the characteristics cannot be attributed to a change in the ratio of the thickness of doped to that of intrinsic layers. For charge injection, an at least 10 nm

thick electron injection layer (EIL) and hole injection layer (HIL) has been employed next to the cathode or anode, respectively. For simplicity, the thickness of the n-doped layer next to the interface will be denoted as X and the thickness of the p-doped layer will be short-termed as Y (inset of figure 5.4d). Figure 5.4 shows the I-V-characteristics for four different sets of CGL-samples.

For figure 5.4a, X and Y are equal and altered from 2 nm to 20 nm. Only the device with 2 nm n- and p-doped layers exhibits a significant difference in the I-V-characteristic. Under forward bias only a slight increase of driving voltage for low current densities can be observed, but reversing the bias leads to a large increase in driving voltage for the $X = Y = 2$ nm device. For a more detailed view the experiment was repeated, again keeping X and Y equal, now ranging from 1 nm to 4 nm with 1 nm step-size. The I-V-characteristics for this set of samples are displayed in figure 5.4b. As for these extremely thin layers the run-to-run reproducibility becomes an issue, the values from figure 5.4a and 5.4b cannot be compared quantitatively and have to be discussed separately and under qualitative aspects. Again under forward bias, only a small increase in driving voltage with decreasing thickness of the doped layers is observed. For reverse bias the driving voltage for a given current density gradually increases for decreasing thickness of the doped layers. This leads to a strong asymmetry of the I-V-characteristic, indicating a less efficient charge generation for devices with less than 5 nm thick p- and n- doped layers. As the results discussed in figure 5.2 suggest, that the symmetry of the I-V-characteristic is affected predominantly by doping of the n-doped layer, it has to be checked, if this is reflected, when the thickness of the doped layers are changed separately. Figure 5.4c shows the I-V-characteristic of CGL-samples for which X varied within the range of 1 nm to 4 nm and Y was kept constant at 20 nm. The characteristics seem to be very similar to those of figure 5.4b with an increasing asymmetry for decreasing thickness of the n-doped layer. When X is kept constant and Y is varied between 1 nm and 4 nm a very different image is revealed as shown in figure 5.4d. For all devices the I-V-characteristics are nearly symmetric and exhibit slightly increasing driving voltages under reverse bias with decreasing thickness of the p-doped layer. Compared to the asymmetry in figure 5.4b and figure 5.4c the increase in driving voltage and the asymmetry can be neglected. It has to be noticed, that no closed films can be expected for only 1 nm layer thickness. The slight increase of driving voltage in the positive regime for the 1 nm thin p-doped layer may be an indicator for this. As for thicker layers, no remarkable differences in the forward characteristics are observed, closed films are expected for thicknesses greater than 1 nm. Summarizing the results shown in figure 5.4, it is evident that a minimum thickness of 5 nm for the n- and p- doped layers next the interface is necessary for efficient charge generation. Further, the charge generation seems to be more sensitive to the thickness

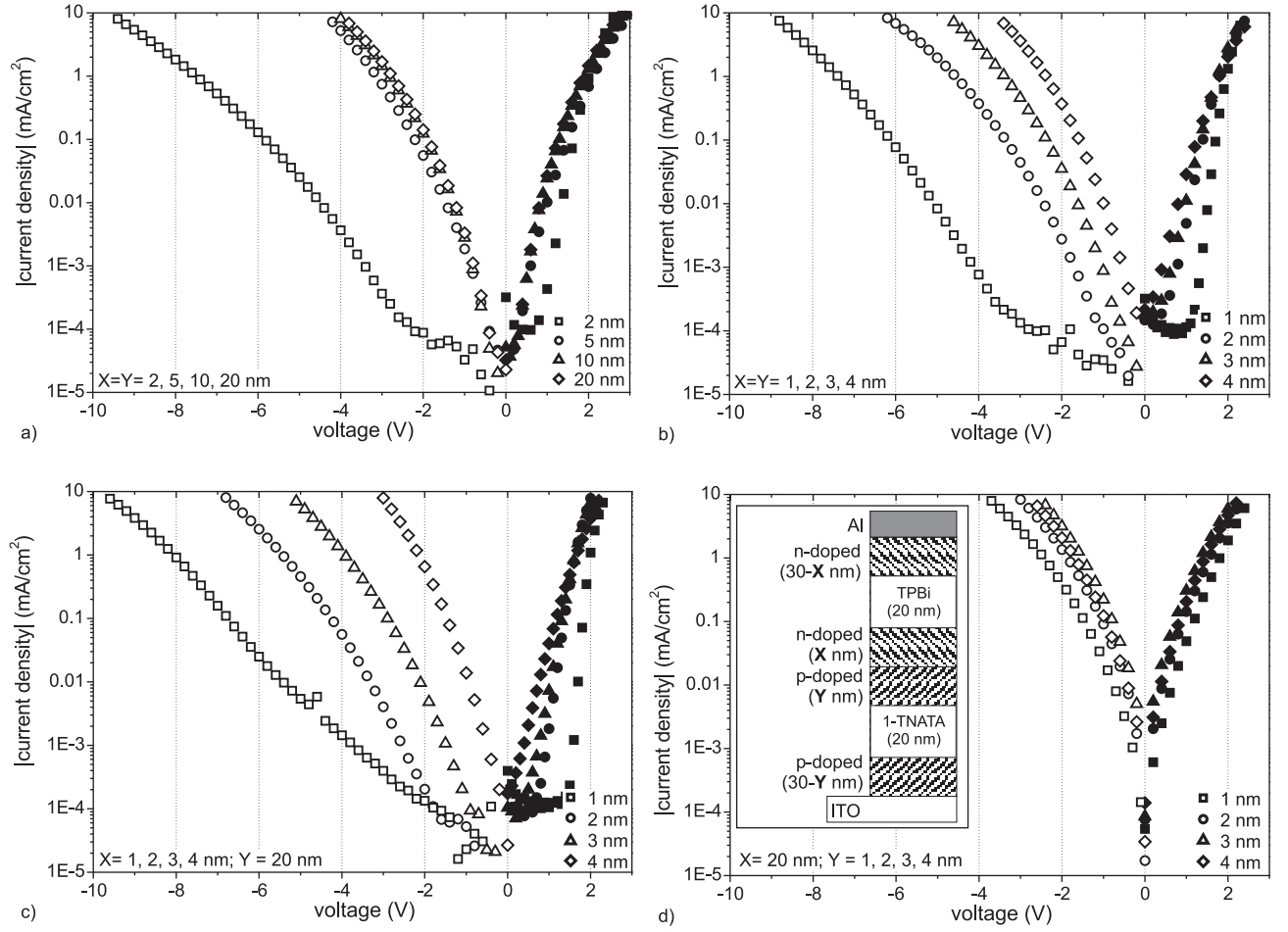


Figure 5.4.: I-V-characteristics for CGL-samples with different thicknesses of the p- and n-doped layers adjacent to the p-n interface. Positive voltage corresponds to ITO electrode at positive bias (closed symbols), negative voltage corresponds to Al electrode at positive bias (open symbols). a) Thickness of p- and n-doped layer varied between 2 nm and 20 nm. b) Thickness of p- and n-doped layer varied between 1 nm and 4 nm. c) Thickness of p-doped layer kept constant at 20 nm, thickness of n-doped layer varied between 1 nm and 4 nm. d) Thickness of p-doped layer varied between 1 nm and 4 nm, n-doped layer was kept constant at 20 nm. The inset displays a schematic of the device structure for all sets of devices.

of the n-doped layer.

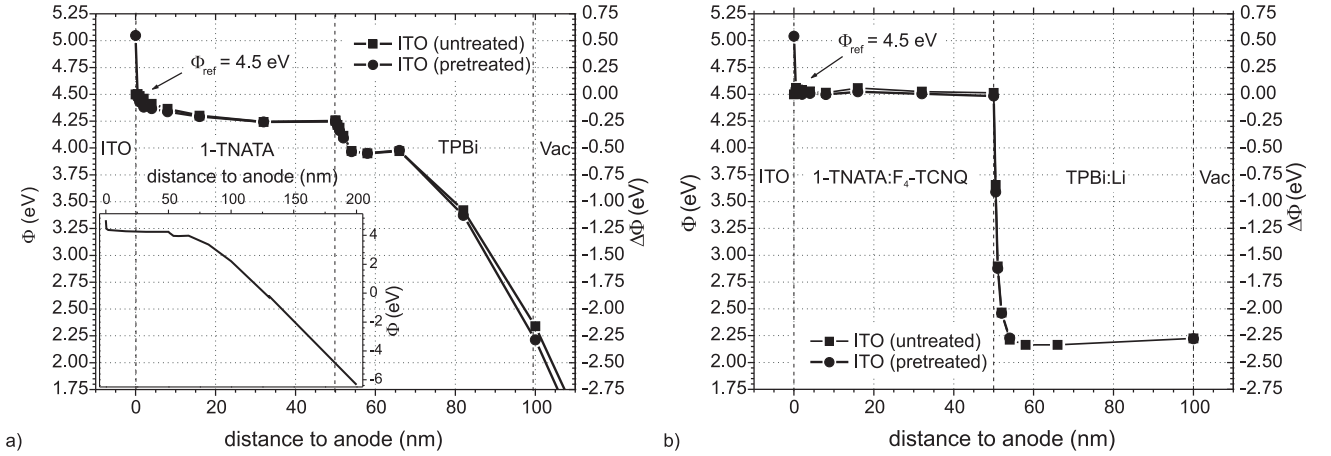


Figure 5.5.: Work function obtained from KP measurements as a function of the film thickness, relative to the ITO substrate's work function for a) an undoped p-n heterojunction (inset: progression of the work function for a thicker TPBi film) and b) a doped p-n heterojunction.

5.2.4. Kelvin Probe measurements

To gain a deeper understanding of the dominating mechanism leading to charge generation at organic/organic heterointerfaces, the energy level alignment at the interface was determined by using a Kelvin Probe (KP) analyzer. Figure 5.5 shows the evaluation of the work function ϕ at different positions within the device. As the KP technique does not provide depth-resolution, and rather delivers the surface work function, the CGL stack was deposited incrementally and the corresponding surface work function was measured after each deposition step. Close to the interfaces an increment size of 1 nm is useful and several 10 nm steps are sufficient at a certain distance from the interface for resolving the energy level alignment. For keeping the samples under UHV conditions during the complete deposition and characterization cycle, a commercial KP analyzer (McAllistor KPG 6500) was mounted to the vacuum deposition system. The experimental error can be estimated to be lower than 20 meV.

The work function was determined for an undoped HTL/ETL stack (see figure 5.5a) and for the so far described CGL-stack (see Figure 5.5b) deposited onto differently pre-conditioned substrates. As the work function of the reference tip is not given by the manufacturer, the measurements are referenced to the substrate's surface work function. Literature values for ITO vary from 4.1 eV to 5.2 eV depending on the pretreatment of the substrate and the mea-

surement technique [59, 70–73, 142]. A work function of 4.5 eV for as-received ITO substrates complies with most of the publications [70, 72, 142]. Furthermore it is documented, that an oxygen plasma treatment prior to the deposition of organic materials leads to an increase of work function of about 0.5 eV [59, 70, 73]. Therefore, a work function of 4.5 eV for untreated ITO and 5.0 eV for ITO films exhibited to an oxygen plasma prior to the organic layer deposition is assumed. For both types of samples (undoped and doped) a good match of the energy levels can be observed for both substrates indicating that the energy level alignment is independent of the pretreatment of the substrate. For the undoped device a slight downward shift of the work function of 0.15 eV is observed with increasing 1-TNATA thickness. Upon the deposition of undoped TPBI the work function decreases within the first 3 nm to about 0.3 eV above the value for undoped 1-TNATA and is constant until 15 nm of TPBI are deposited. The vacuum level shift at the interface can be attributed to a small interfacial dipole as it has been observed for other undoped organic/organic interfaces. [143] For thicker undoped TPBI layers the work function shows a steep linear decrease of several eV. This effect has been investigated by Ito *et al.* in 2002 [144]. They observed a spontaneous buildup of surface potential upon deposition of Alq₃ onto an Au substrate. The surface potential determined by the KP method reached 26 V for a 560 nm thick film and was explained by preferential orientation of the dipole moments of Alq₃ molecules. Furthermore it has been demonstrated, that irradiating the sample with visible light ($\lambda < 600$ nm) removes the surface potential. This has been attributed to the loss of preferential orientation upon electronic excitation of the molecules. A change of surface potential of about 10.3 eV can be observed upon deposition of 135 nm of TPBI, as shown in the inset of figure 5.5a. The slope of the rise in surface potential is about 0.07 eV/nm and is close to the value determined by Ito *et al.* for Alq₃ (0.05 eV/nm). For this reason, it is most likely, that a similar mechanism holds for the observed spontaneous buildup of surface potential in undoped TPBI films. In addition, it can be expected, that the preferential orientation will also be removed by charges injected into the film upon applying an external bias. Therefore, the characteristics of undoped devices should not be affected by the measured phenomenon, which will be neglected in the further discussion. Overall, only a small interfacial dipole can be observed between 1-TNATA and TPBI. The energy level alignment at the interface significantly changes when doped ETLs and HTLs are investigated.

Figure 5.5b shows the progression of the work function with film thickness for doped transport layers. Upon deposition of F₄-TCNQ doped 1-TNATA onto the substrate the work function is measured to be 4.5 eV and independent of film thickness and substrate pretreatment. As this value equals the work function assumed for untreated ITO as reference substrate, no interfacial dipole should be expected in this case. For the oxygen-plasma-treated

ITO an interfacial energy shift of 0.5 eV can be observed, which corresponds to the difference in work functions. At the p-n junction between the HTL and the Li-doped TPBI ETL the energy level drastically shifts towards lower values. Within the first nm the work function changes by 1.6 eV. As the prior results suggested that 1 nm of deposited film is needed for a closed surface, this shift in work function is most likely due to an interfacial dipole. The value of the work function further decreases until the curve saturates for film thicknesses above 5 nm at a work function about 2.3 eV lower than that measured for the p-doped HTL. The observed band bending is an indicator for the exchange of free charge carriers at the p-n junction leading to a space-charge region of about 5 nm thickness.

In a recent paper, Law *et al.* showed results for UPS measurements on a CGL-structure very similar to that one employed in this work. The reported structure consisted of Mg-doped Alq₃ as n-type electron-transporting layer and m-MTDATA doped with F₄-TCNQ as p-doped hole-transporting layer [141]. They observed an interfacial dipole of 0.46 eV and an upward band bending of 1.36 eV, giving a total energy shift of 1.82 eV. Due to the fact that KP measurements do not allow to clearly separate the influence of interfacial dipoles from the influence of space charges, only the overall energy shifts should be compared. The shift of work function of about 2.3 eV within Li-doped TPBI is close to the vacuum level shift of 1.82 eV within m-MTDATA doped with F₄-TCNQ measured by UPS. Furthermore the width of the space charge region within the ETL was determined to be about 5 nm which complies very well to the value (6.4 nm) given in the mentioned publication [141]. As both techniques -UPS and KP- are surface sensitive, it can be assumed, that the deposition of the n-doped TPBI ETL on top of the p-doped 1-TNATA HTL also leads to a thin space charge region within the HTL.

5.2.5. energy level alignment

The presented results lead to the conclusion, that at doped organic p-n junctions the exchange of charge carriers induces a drastic band bending, which is in the same order of magnitude as the optical band gap of the organic materials, leading to a thin depletion zone within both layers adjacent to the heterointerface. Figure 5.6 depicts the energy level alignment and compares the involved physical processes for forward and reverse bias taking a simple CGL-structure as example. The given values for the work functions of the electrodes [142,145] and the HOMO and LUMO levels of the organic materials [91,107] are taken from literature. According to the presented KP measurements the Fermi level within the p-doped HTL lies 4.5 eV below the vacuum level (VL) and 0.6 eV above the HOMO level. Considering literature values for Cs-doped CuPc films [146], the position of the Fermi level within the n-doped ETL has been assumed to be 0.2 eV lower than the LUMO edge. At

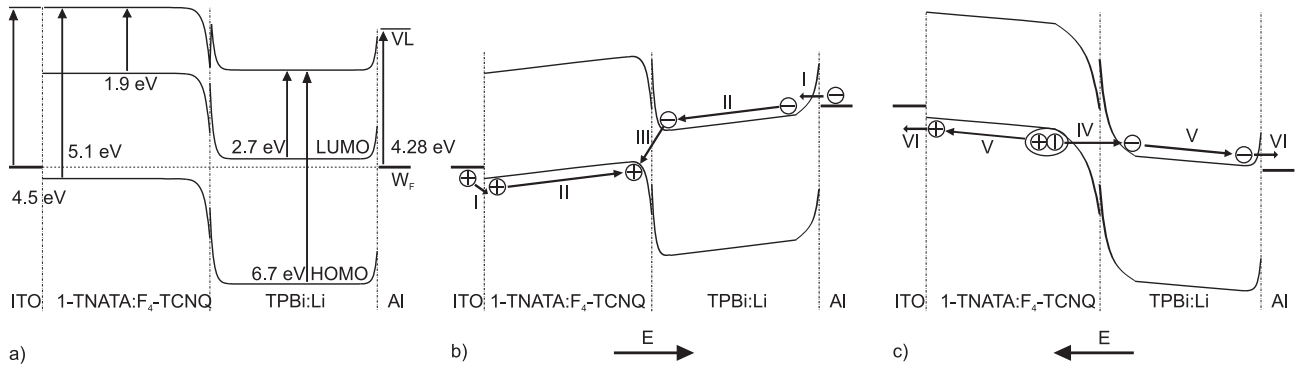


Figure 5.6.: Energy level alignment for a CGL-device: a) no external bias, b) under forward bias (recombination) , c) under reverse bias (charge generation)

the p-n interface, the exchange of free charge carriers and a possible interface dipole have to be taken into account. The downward band bending in the ETL quantitatively corresponds in energy and width to the results obtained by KP. The upward band bending was approximated in energy and width by the values given by Law *et al.* [141]. Both, upward band bending within the HTL and downward band bending in the ETL, as well as an interfacial dipole ($\Delta E = 1 \text{ eV}$) have been included in the vacuum level alignment shown in figure 5.6a. When no external bias is applied, equilibrium conditions demand for a common Fermi level throughout the device (see figure 5.6a). The energy level alignment is not expected to be completely correct in quantitative values, but it qualitatively suffices to explain the observed charge generation. For the purpose of simple understanding, the VL and explicit values for energy levels are not included in Figures 5.6b and 5.6c.

Under forward bias holes are injected from the anode into the HTL and electrons are injected from the cathode into the ETL. In figure 5.6b the charge injection is denoted as I at both electrodes. For highly doped organic semiconductors it has been demonstrated, that at the interface towards the electrode band bending and charge injection via FN-tunneling through a narrow space charge region may occur [83], as shown for the electron injection from the cathode. At the anode flat-band conditions apply and holes have to pass a small injection barrier of 0.35 eV. The injected holes are transported - most likely via hopping - towards the heterointerface (II). The tilted energy levels within the bulk of the HTL and ETL account for the voltage drop across the transport layers due to the limited bulk conductivity of the organic materials. At the heterointerface electrons and holes recombine. The recombination mechanism shall not be discussed in detail, but recombination via gap states, dopant states or excited complexes at the interface may occur (III). In all cases of recombination, accumulation of both carrier types close to the heterointerface is expected, resulting

in a significant voltage drop across the interface. For higher external fields, LUMO level alignment is expected, leading to a direct injection of electrons into the HTL. Then, most of the excitons formed within the HTL are quenched by the high acceptor concentration, as only negligible light emission could be observed (not shown here).

In the case of reverse bias it has already been demonstrated, that only charge generation at the p-n interface can lead to a significant current. Under zero bias the LUMO level of the ETL lies only about 300 meV above the HOMO level of the hole transporting layer [141]. Applying a reverse bias even lowers the position of the ETL's LUMO level with respect to the HOMO level of the HTL, which are separated by a few nm thick energy barrier. There is a finite probability σ_{pn} , that electrons may tunnel through this barrier from occupied HOMO states of the HTL to unoccupied LUMO states of the ETL (IV). The probability σ_{np} for the vice versa process IV⁻¹ of electrons tunneling from filled LUMO states in the ETL to unfilled HOMO states in the HTL equals σ_{pn} , but the process can be neglected, as almost no free charge carriers are present close to the p-n interface due to the depletion of the space charge region. Furthermore, electrons tunneling from the HOMO of the HTL into the LUMO of the ETL will immediately be driven away from the interface by the external electric field (V). This leaves a hole in the HOMO of the HTL, which in the same way immediately escapes the space charge region at the interface (V). As in the regarded case no or only small energy barriers are present at the electrodes, the charge carriers can easily escape (VI). Considering the case of a stacked OLED, these charge carriers can be injected into neighboring recombination zones, where they recombine with charge carriers injected from the electrodes of the stacked OLED.

As tunneling processes in general are regarded as temperature-independent, the model, which is developed from the experimental data collected via KP measurements and thickness-dependent IV-characteristics, fits well to the results for low temperature I-V-characteristics.

5.3. stacked inverted organic light emitting diodes

So far, the stacking concept was only demonstrated for conventional bottom emitting OLEDs. To confirm the suitability of the stacking concept for any type of OLED design, stacked IOLEDs with 2 EMUs were prepared. The device structure was adopted from the structure of highly efficient IOLEDs employing doped injection layers, which is presented in section 4.5. Figure 5.7 shows characteristics for a stacked OLED employing two EMUs. The layer structure is depicted schematically in the inset of figure 5.7a and is further detailed in the figure's caption. Operational parameters are summarized in table 5.1.

A characteristic brightness of 500 cd/m² is reached at a driving voltage of 23.2 V. Assuming

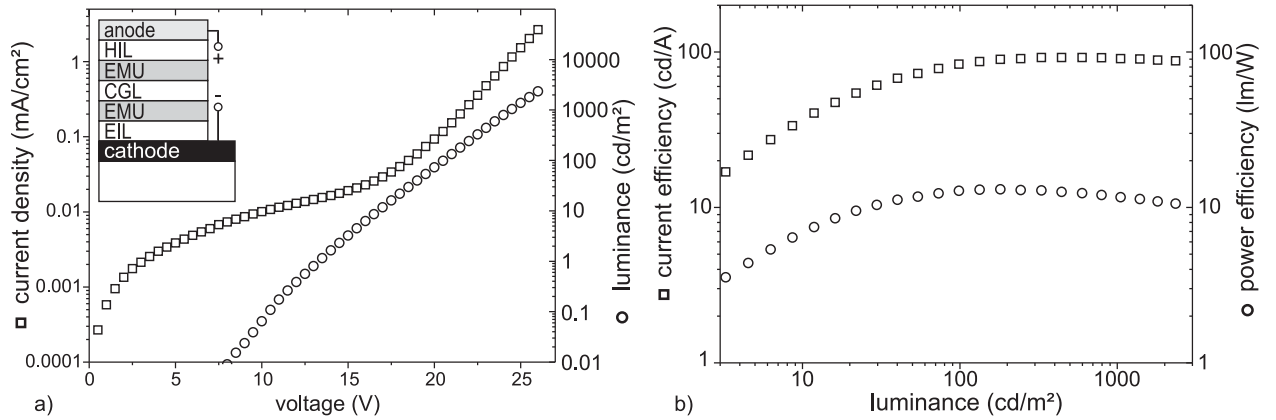


Figure 5.7.: a) LIV-characteristics of a stacked IOLED: current density (squares) and luminance (circles) plotted against voltage. The inset shows the device structure. b) Device efficiency: current efficiency (squares) and power efficiency (circles) plotted against luminance. The inset shows an EL spectrum of a stacked IOLED at a driving voltage of 23 V. Structure of functional units (thickness in nm): Cathode: Ag 120, EIL: BPhen:Li 40, EMU: TPBI 10\TPBI:Ir(ppy)₃ 10\TCTA:Ir(ppy)₃ 10\TCTA 5\α-NPD 5, CGL: 1-TNATA:F₄-TCNQ 40\BPhen:Li 40, HIL: 1-TNATA 10\pentacene 20\PEDOT:PSS 30, anode: ITO 60.

that the driving voltage splits up equally for each EMU, 11.6 V per EMU have to be applied. This is slightly higher than the voltage which has to be applied to a single EMU IOLED (10 V), as listed in table 4.3. The difference is within the limit of reproducibility and is most probable caused by an unintentional variation of the Li doping concentration. It may also be possible that, despite the hydrophobic barrier function of pentacene the CGL unit is affected by the water from the aqueous dispersion during spin coating of the PEDOT:PSS anode.

Figure 5.7b shows, that a superior current efficiency of 92.4 cd/A is measured at a brightness of about 600 cd/m², representing an increase of about 60 % when compared to the maximum current efficiency of the single EMU IOLED. As the increase in driving voltage is slightly higher than 100 %, and the current efficiency increase below, the power efficiency is cut down

Table 5.1.: Characteristic values of a stacked IOLED: Bias V_b for a luminance of 500 cd/m², current efficiency η_c at 500 cd/m² and maximum value, power efficiency η_P at 500 cd/m² and maximum value.

	V_b (V)	η_c (cd/A)	η_c (cd/A)	η_P (lm/W)	η_P (lm/W)
	500 cd/m²	500 cd/m²	max.	500 cd/m²	max.
2 EMUs	23.2	92.3	92.4	12.5	13.1

to 13.1 lm/W. Nevertheless, it shows, that the stacking concept also enhances the current efficiency of IOLEDs. The device shows the potential for further optimization to reduce the driving voltage by introducing doped buffer layers instead of PEDOT:PSS to achieve a closed vacuum preparation cycle. Further, the optical cavity has to be tuned to maximize the light outcoupling factor, thereby increasing the efficiency of the stacked IOLED.

6. Advanced process technology

In the following sections, different concepts for inline processing of full color AM-OLED displays will be introduced and discussed with regard to mass production aspects.

6.1. inline system for sputtering of indium tin oxide

Thin films of indium tin oxide (ITO) can be deposited via several different coating technologies. To list just a few, thermal evaporation, chemical vapor deposition (CVD), spray pyrolysis, pulsed laser deposition (PLD) and sputtering shall be mentioned. A comprehensive survey about transparent conductive oxides and related deposition techniques is given in reference [147]. Within the last decade sputtering became accepted as the major production technology for high quality ITO coatings. This is mainly due to its suitability for high throughput inline processing. From an economic point of view, it is reasonable to also use existing production equipment - currently used for the fabrication of LCDs - for the production of AMOLEDs, where possible [148]. Therefore, only sputtering of ITO will be discussed in detail.

The functional principle of the sputtering process is illustrated in figure 6.1 in a diode configuration. The principle setup consists of a closed vacuum system, a gas inlet for the process gas, a piece of material, which is to be sputtered and is denoted as target, and a substrate, onto which the thin film will be deposited. In the schematic, a negative bias is applied to the target - the substrate and the vacuum chamber are connected to ground potential. If a single free electron is present, it will be accelerated by the influence of the electric field. The electrons are scattered by collision events with gas atoms. Inelastic scattering occurs, when the kinetic energy of an electron is high enough to excite or ionize a gas atom, respectively molecule. The relaxation of excited gas atoms and molecules can be observed by the characteristic light emission for the participating gas species. Further ionization of gas atoms generates a plasma. Within the plasma free electrons are accelerated away from the target, positively charged gas ions are accelerated towards the target and gain high kinetic energies of up to 100 eV. When the ions hit the target's surface, the kinetic energy is transferred to the struck surface atoms, allowing them to surpass the lattice binding energy. As the substrate is placed in front of the target, sputtered particles will be deposited onto the substrate.

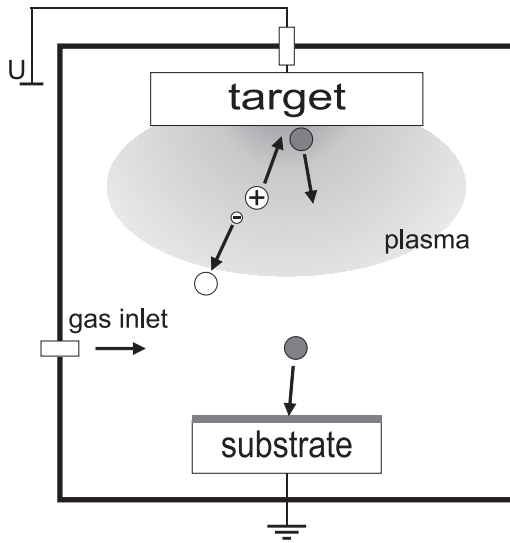


Figure 6.1.: Functional principle of the sputtering process.

The electrical and optical properties of ITO thin films mainly depend on four process parameters - the substrate temperature, the pressure, the oxygen partial pressure and the plasma excitation mode. These parameters and the challenges related to sputtering ITO on top of organic thin films shall be further outlined.

substrate temperature

High quality ITO thin films are deposited at elevated temperatures of more than 200 °C [149]. The thermal energy facilitates the crystallization during the thin film growth and leads to larger grain sizes, enhancing the conductivity and the transparency. Often, the deposited thin films are annealed in a thermal post-treatment, which further improves the conductivity and the transparency. When ITO is sputtered as top contact for surface-emitting OLEDs, the substrate should not be heated, as the organic layers may recrystallize, intermix or decompose. For example the glass transition temperature for α -NPD is 96 °C [91]. Therefore the IOLED substrate is kept at room temperature, limiting the possibilities to deposit highly conductive and transparent ITO. During the process, plasma interaction and the kinetic energy of the impinging atoms heat up the substrate. Not only that the substrate should not be externally heated, it has to be ensured, that during the process, the temperature does not rise above a critical value, at which thermal degradation of the organic layers is likely.

In a preceding work, the temperature rise during sputtering was below 50 K, which did not significantly affect the device characteristics [25].

pressure

The sputtering plasma is generated by ionizing collisions of neutral gas atoms and electrons respectively ions, which both are accelerated by the electric field applied to the cathode. A constant glow discharge and thereby a stable plasma is achieved, if acceleration and ionization are well balanced. This balance strongly depends on the mean free path between two scattering events and can therefore be controlled by pressure. If the pressure is very low, the mean free path is very long, resulting in too few collisions to keep the plasma going. On the other hand, if the pressure is very high the mean free path becomes too short, so that the mean kinetic energy, which electrons and ions receive by the field-induced acceleration, does not suffice to ionize the corresponding scattering partner. Within the transition region between both cases the mean free path is long enough to enable ionization of the collision partners and short enough that the accelerated ions and electrons experience several scattering events before hitting the target respectively the side wall of the vacuum chamber. For sputtered atoms, a low pressure means less collisions before hitting the substrate. Comparing processes carried out at higher pressure, the kinetic energy of particles impinging on the substrate is increased. On the one hand, the kinetic energy of the sputtered particles strongly affects the degree of crystallization of the thin film, so that above a critical pressure the conductivity of the deposited thin film is dramatically reduced. If on the other hand the task of sputtering ITO on top of organic thin films is concerned, a high kinetic energy of impinging particles may crack the molecular bonds and strongly degrades the device characteristics.

oxygen partial pressure

The film growth mode strongly depends on the amount of oxygen which is incorporated into the film. This can be controlled by adding oxygen to the sputtering gas. For low oxygen content, the film grows in an amorphous metallic mode. In this case the film exhibits a very high free carrier density, but only a very low carrier mobility due to a large density of oxygen vacancies, which act as scattering sites and limit the conductivity. Further, the transparency of the film is very low. If the oxygen content is increased, the growth mode shifts to a polycrystalline oxide mode. With increasing grain size, scattering at grain boundaries is reduced. This enables electron mobilities of up to $50 \text{ cm}^2/\text{Vs}$ [150]. Any further increase of the oxygen content fills up oxygen lattice vacancies and leads to trapping of free electrons,

which means a reduction of the carrier density and the carrier mobility. This drastically reduces the conductivity in the oxide mode. The perfect oxygen partial pressure lies within the transition between metallic to oxide mode, and permits a rather high electron density, a high electron mobility and a high optical transparency. Further, the oxygen content influences the work function of the thin film, which has been demonstrated to affect the suitability as hole injecting contact (see section 2.3.1).

plasma excitation

There are several different possibilities of exciting plasmas with technical relevance for production applications. Direct current sputtering (DC) is the most simple technique but can only be applied to conducting target materials. The principle has been described by means of figure 6.1. For DC magnetron sputtering, a very dense plasma close to the target surface is observed.

Insulating materials as well as conductors can be deposited by radio-frequency sputtering (RF). A very common frequency for RF sputtering is 13.54 MHz. At this frequency, only electrons are able to follow the alternating field. Collisions of electrons and neutral gas atoms, generates further electrons and ions. When electrons hit grounded parts of the process chamber, the charge is led towards ground potential. If the electrons hits the non conducting target, they get absorbed and a surface charge builds up. The heavier gas atoms cannot follow the RF excitation, so that the surface charge which builds up during the first half of one single period is not equalized during the second half. On the average, a negative bias builds up and positively charged gas ions get accelerated towards the cathode. In RF configurations, the target is isolated from ground potential by a capacitor. For an alternating potential this capacitor represents an electrical short. This way, conducting and non-conducting materials can be sputtered. Within RF magnetron sputtering configurations, the plasma extends far away from the target, so that the impact of the plasma on the film growth is much bigger than in DC configurations. Another difference, which influences the film growth, is the kinetic energy of the sputtered atoms. In DC configurations, the cathode discharge bias is much higher than the RF-induced bias on the cathode. In general, a higher bias voltage results in a higher kinetic energy of the sputtered atoms.

6.1.1. ITO sputtering onto organic thin films

Sputter-deposition of ITO as top electrode for OLEDs may harm these for several reasons. Due to the high energy-excitation of the plasma, light in the deep UV range below 200 nm

wavelength is emitted. This corresponds to a photon energy, which by far exceeds the intermolecular bonds and may cause dissociation of organic molecules. The kinetic energy of sputtered atoms, fast electrons and ions striking the organic molecules, is in the range of several 10 eV. Inelastic scattering with organic surface molecules may also cause the dissociation of latter ones. Further the impact of high energetic particles heats up the substrate. If the temperature rises above the glass transition temperature, the mainly amorphous organic thin films recrystallize. This causes intermixing of the organic layers and results in a reduced device efficiency and a lower yield, due to an increased density of electrical shorts.

Although sputtering of ITO on top of OLEDs inherits several challenging tasks and underlies sensitive restrictions, sputtered ITO layers have already been employed for transparent [17, 18, 112, 151] or top-emitting [23, 24, 26] OLEDs. Transparent cathodes were realized by sputtering ITO either on top of semitransparent metal films [18, 21] or onto a molecular protective cap layer [19, 152]. For IOLEDs, molecular [23, 24] or polymeric [25, 26] buffer layers have been employed to enable sputtering of ITO as top anode. Another approach of reducing the sputter induced damage of the organic layers is facing target sputtering (FTS), which was demonstrated recently [153].

In early reports about sputtering of ITO on top of organic semiconductors the referred ITO deposition rate was rather low [18, 23]. Prior to this work, a two-step sputtering sequence was developed to decrease sputter induced damages and to increase the deposition rate [25]. In the first step a 10 nm thin seed layer was deposited at very low RF power of 0.16 W/cm² yielding a deposition rate of 2 nm/s. Then the power was raised to 0.56 W/cm², increasing the deposition rate to 8.5 nm/s. This standard process served as initial point for the development of an inline process for room-temperature sputtering of ITO.

6.1.2. inline sputtering system: setup

The referenced standard ITO deposition process was performed on a commercial Leybold Z590 sputtering system. ITO (90 %In₂O₃/10% SnO₂) was sputtered in a pure argon atmosphere at a pressure of 5 μbar. The distance between target and substrate was 70 mm. According to these initial values a custom inline sputtering module as extension for the existing inline OMBD system was designed. Figure 6.2 shows an image of the completed inline sputtering system. A cubic vacuum chamber served as sputtering module, featuring a water-cooled linear magnetron sputtering source, two mass flow controlled gas inlets and a pressure control system. Samples can be loaded via a vacuum load lock and a linear transfer system, which is installed into several standard vacuum tubes attached at both sides of the sputtering chamber. The target size is 320 x 60 mm², enabling a thickness uniformity of better than -3 % of the center value across the a maximum substrate width of 180 mm. Pure Argon and

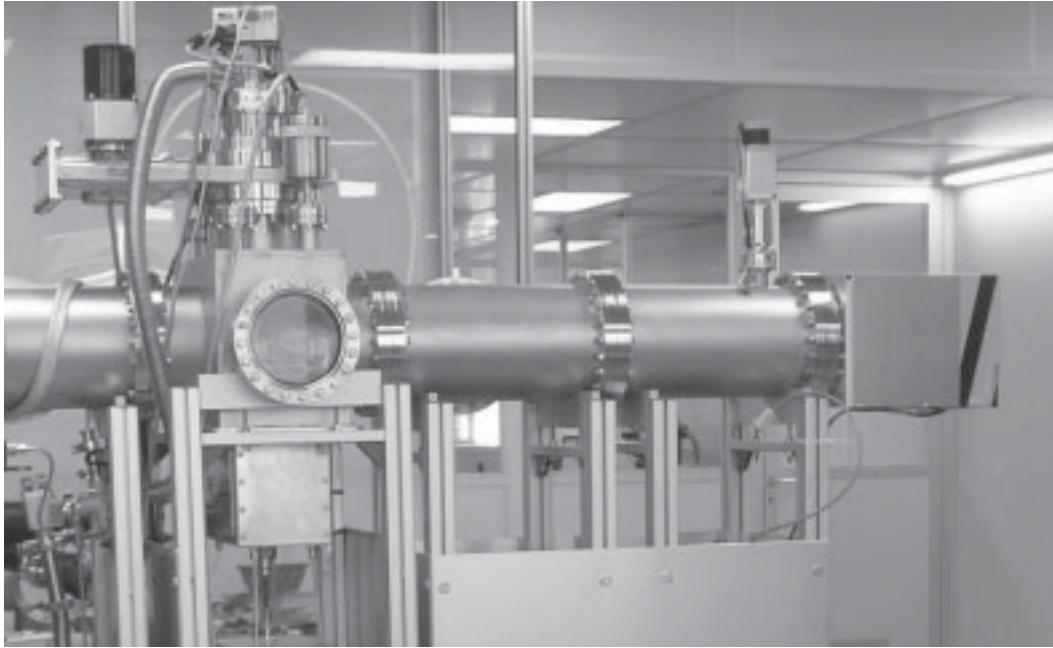


Figure 6.2.: Custom-built inline sputtering system.

pure Oxygen are used as process gases. It has been reported, that in terms of less sputter induced damage of the organic layer DC sputtering may be advantageous over commonly used RF sputtering [152]. Therefore, both - a DC and a RF power generator - were installed. A blocking filter allowed to use RF and DC power at the same time.

6.1.3. dependence of electrical and optical properties on plasma excitation and oxygen flow

By setting up a new sputtering tool, the complete IOLED deposition process should be transferred to an inline system. Most process parameters were kept unchanged compared to the established cluster tool process. Table 6.1 displays the parameters for the standard and the inline sputtering process. The inline process was developed, by varying the Oxygen flow from 0.0 sccm to 2.0 sccm and the RF power ratio from 0 % to 100 %, and comparing the transparency and the conductivity of the deposited thin films. ITO thin films were deposited onto cleaned float glass substrates. The thickness of the films was determined by stylus profilometry (Dektak 8) at edges, which were etched into the film after deposition. The conductivity as well as the charge carrier density and mobility were determined at room temperature by using the van der Pauw method [154]. The transparency of the thin films was determined by referring the transmission spectra of the samples to an uncoated reference

Table 6.1.: Comparison of standard Leybold process and the inline process to be developed. The values for the Leybold process are taken from [25]. For the inline process, RF power ratio and oxygen flow are varied. As deposition rate, conductivity and transparency are functions of the varied parameters, former ones have to be determined (tbd).

parameter	Leybold process	inline process
power density	0.54 W/cm ²	1.04 W/cm ²
RF power ratio	100 %	varied
substrate temperature	20 °C	20 °C
pressure	5 μ bar	5 μ bar
argon flow	40 sccm	50 sccm
oxygen flow	0 sccm	varied
target substrate distance	70 mm	70 mm
substrate movement	oscillating, $\pm 45^\circ$, 2 rpm	oscillating, ± 200 mm, 20 mm/s
substrate potential	float	float
deposition rate	0.15 nm/sec	tbd
conductivity	≈ 1760 S/cm	tbd
transparency	81.3 % @ 550 nm	tbd

substrate. The given value, represents the mean transparency over a spectral range from 400 nm to 700 nm.

Figure 6.3 shows a three dimensional plot of the deposition rate against RF power ratio and oxygen flow. The deposition rate significantly drops, when the RF power ratio is increased. This has already been observed before, and can be explained by the lower cathode bias for RF sputtering compared to DC excitation [155]. For DC processes, the deposition rate seems to be independent of Oxygen flow. The situation changes, when RF power is superimposed. Now the deposition rate clearly decreases for increasing oxygen content. A decreasing deposition rate for increasing oxygen partial pressure has already been reported for RF sputtering of ITO from a ceramic target and was explained by increasing oxidation of the target [156]. This leads to a reduction of the sputtering yield, which is defined by the number of atoms

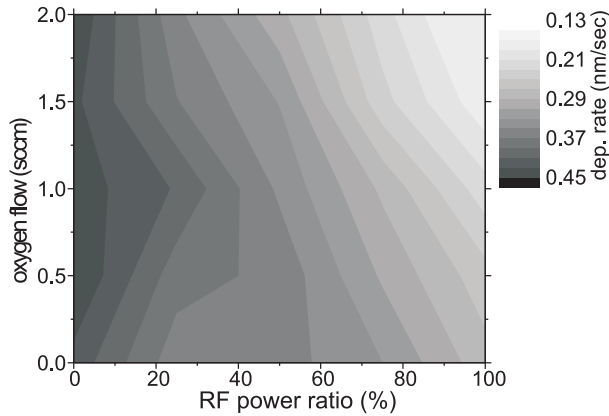


Figure 6.3.: Dependence of deposition rate on RF power ratio and oxygen flow for RF/DC sputtering of ITO.

sputtered by one single ion. It is known that the density of atomic oxygen species is lower for DC compared to RF plasmas [157]. An observable influence of the oxidation of the target surface on the deposition rate during DC sputtering processes is therefore expected to arise at a significantly increased oxygen level compared to RF sputtering. The presented data suggests, that this level is above the upper limit, employed for this work.

Next, the optical and electrical properties of the sputtered ITO thin films will be discussed. The experimental data is presented in figure 6.4. The transparency rises as the oxygen flow and thereby the amount of oxygen, which is incorporated into the thin film, rises. For zero oxygen flow, the film grows in an oxygen-deficient metallic mode, where light is rather scattered or absorbed at metallic clusters than transmitted [157]. Raising the oxygen flow leads to an oxide film growth, increasing the transparency to more than 85 %. Transparency values of about 90 % have been measured for fully oxidized ITO thin films. As the oxygen content was very high, these films showed only a very poor conductivity. Compared to RF sputtering, an increased oxygen flow was necessary to achieve a good transparency when sputtered in DC mode. It was already mentioned, that the density of atomic oxygen species is higher in RF plasmas, so that for DC sputtering a higher oxygen flow has to be employed to obtain equal thin film properties. Apparently, this is also true for the electrical properties, as the oxygen flow for maximum conductivity is shifted to higher values, when the RF power ratio is decreased. A maximum conductivity of about 2300 S/cm ($430 \mu\Omega\text{cm}$) was measured for ITO thin films sputtered with 100 % RF power and an oxygen flow of 0.5 sccm. The gas flow correlates to an admixture of 1 %, and complies with literature values reported for RF sputtering at elevated temperatures [156]. For DC processes, highest conductivity is obtained for an oxygen flow of 1.0 sccm (2 %). If the oxygen level is below the optimum, smaller grain sizes or even an amorphous morphology are expected. Further, the excess of metallic species in the thin film leads to the formation of metallic clusters. In these films, the charge

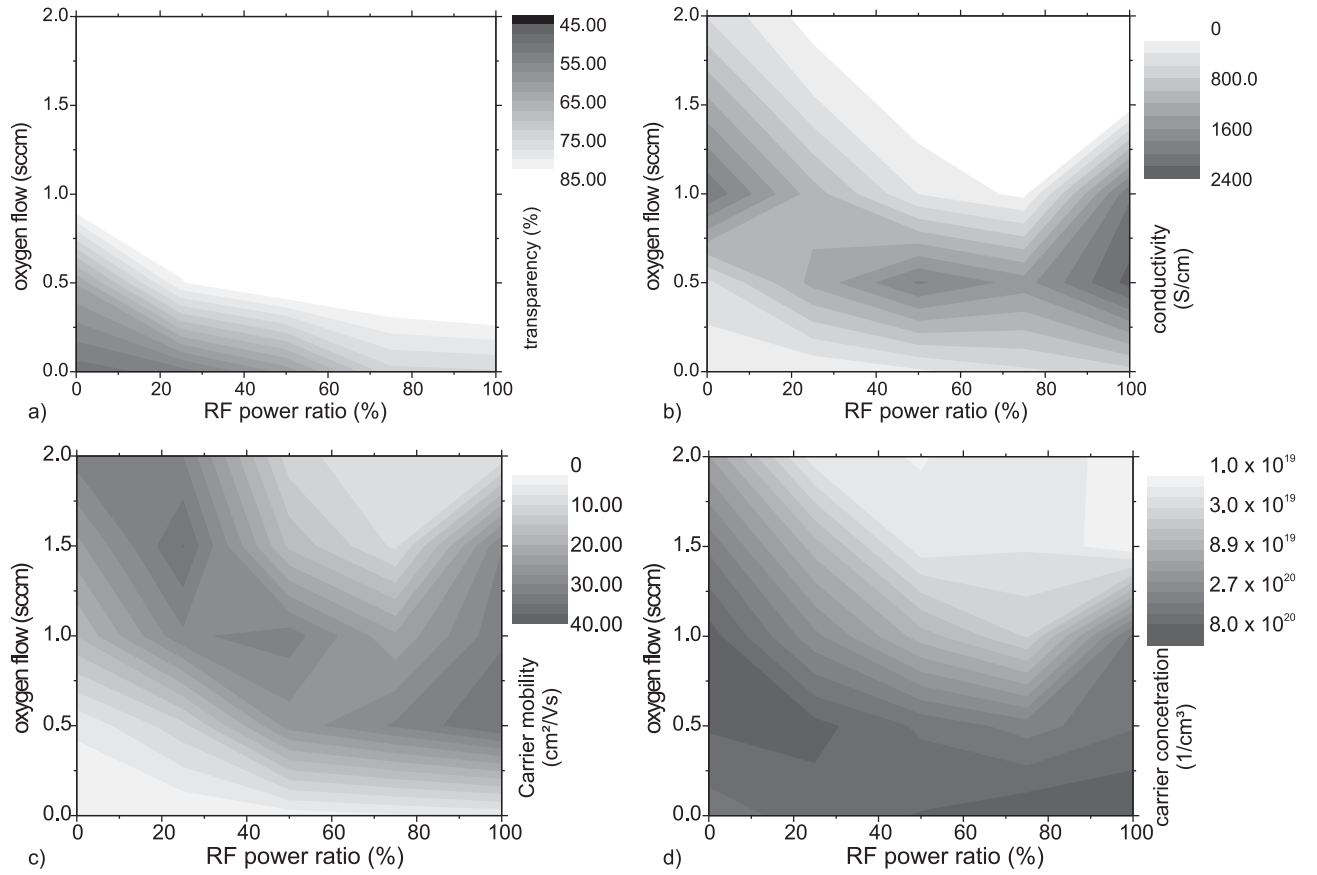


Figure 6.4.: Dependence of optical and electrical properties of sputtered ITO films on RF power ratio and oxygen flow. a) Transparency, b) conductivity, c) electron mobility, d) electron density.

carrier density is very high, but scattering at the grain boundaries drastically reduces the mobility. In oxygen-rich films excess oxygen atoms occupy interstitial defect states within the crystal lattice. These interstitial defects act as deep electron traps and scattering site, so that the electron density and mobility are reduced. It was demonstrated, that thermal annealing of over-oxidized ITO films enhances the conductivity and was attributed to the degasing of loosely bound interstitial oxygen [158].

In conclusion, the initial conductivity and transparency values are reproduced or even exceeded. Further, RF/DC sputtering allows to tune the ion flux onto the substrate [155], which is expected to have a great impact on the device characteristics of IOLEDs. If a higher conductivity is demanded, the application of thin metal layers sandwiched between two ITO layers [159, 160] will be advantageous.

6.2. linear co-evaporation source for organic materials

In OMBD cluster tools, mainly point sources are used for the deposition of organic materials. An uniform film thickness is achieved by a very large distance between sample and source. Often, the substrate is rotated to achieve a high uniformity for smaller distances. Nevertheless, to achieve a homogeneity better than $\pm 5\%$ ¹, the distance between the substrate and the point source is generally several times bigger than the substrate dimensions. This leads to a very low material utilization of about 5% [29], which is acceptable for research but strikes the cost effectiveness when applied for production. In the past linear and planar source concepts for large area deposition of organic materials have been developed [7, 29, 161, 162]. Prior to this work, the first linear deposition source for organic materials was developed [7]. The source consisted of a custom quartz tube with laser drilled holes aligned along the deposition axis. A thin molybdenum wire was winded around the quartz tube as heating element. The organic material was filled into the quartz tube, which then was closed by a quartz sealing. The internal temperature was monitored by a thermocouple fed through the quartz sealing. Several of these sources were installed into an inline OMBD system. Within this system substrates with a maximum size of 180 x 240 mm² were handled. Uniform thin films were achieved by a combination of a homogenous linear deposition profile, stable deposition rates and steady substrate movement perpendicular to the source axis. Due to the small distance between substrate and deposition source, the material loss was minimized. Similar linear evaporation sources for organic materials achieved a material utilization of more than 50% [29].

Due to the short distance between substrate and evaporation sources, the overlap of the molecular beams of two neighboring sources is very small. Therefore, doped thin films cannot be prepared with the described source configuration. Even when the sources are tilted towards a common center position the limited overlap of the molecular beams of two neighboring sources may affect the device characteristics. A possible solution to this task is presented in the following section, where a novel source concept, which allows to co-evaporate two different materials from one source, is introduced.

6.2.1. concept

The primary goal was to design a linear evaporation source, which allows to deposit two different materials perfectly aligned on one single axis. Figure 6.5 show a schematic of the

¹By experience, a thickness deviation of $\pm 5\%$ from the mean value is not noticed by the human eye, when operated.

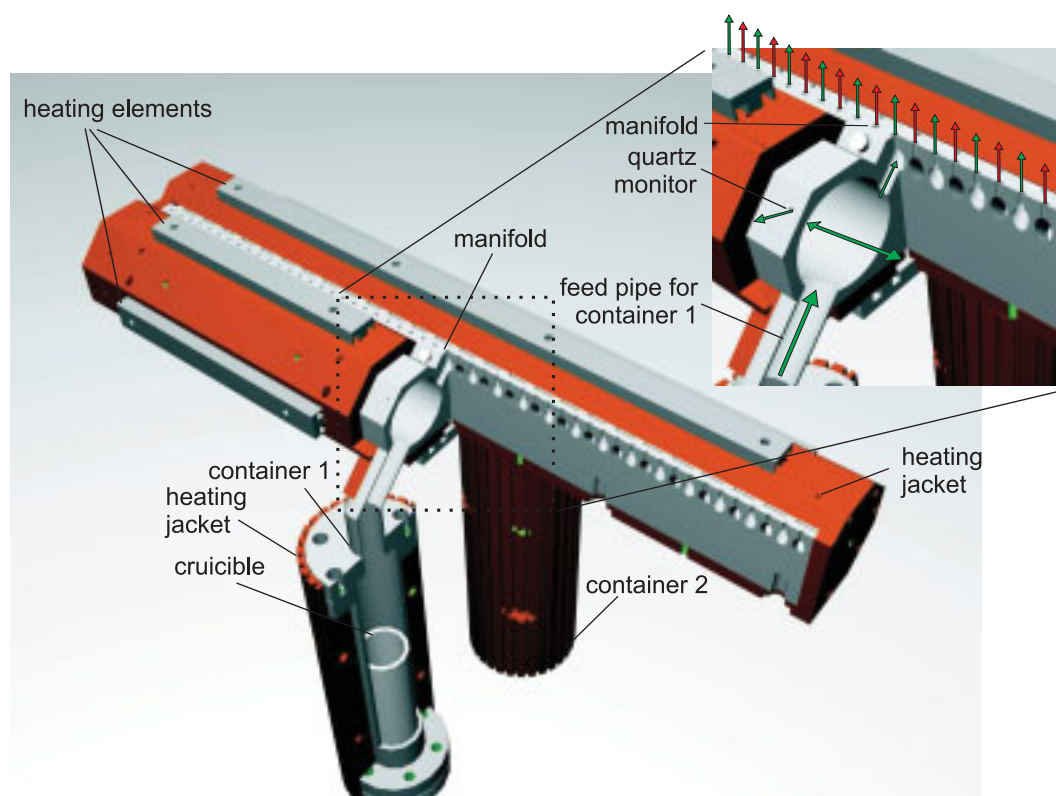


Figure 6.5.: Cross-sectional schematic of the linear co-evaporation source. The inset shows a magnification of the manifold and depicts the working principle. Green arrows indicate the flow of material 1, red arrows indicate the flow of material 2.

developed source concept. The evaporation source consists of two separate evaporation containers which are connected via feed pipes to a linear gas manifold. Both, manifold and containers are made from stainless steel. This offers a higher degree of freedom for the design-engineering at the cost of a possible incompatibility with strongly reactive materials. The first generation of linear evaporation sources lacked from a temperature gradient across the quartz tube. Therefore the stainless steel bodies are clad with copper heating jackets, which uniformly distribute the heat across the evaporation source. Pieces of Molybdenum wire, insulated within thin ceramic tubes and fixed at their positions by stainless steel supports, served as heating elements. The manifold is permanently held at process temperature. Before and after deposition, the containers are kept at a temperature which is below but close enough to the sublimation temperature to ensure a relatively short heat-up time. Both containers are shielded with water cooled stainless steel tubes (not shown in the figure), to avoid radiation induced cross talk of the containers' temperatures. This should also enable short cool-down delays.

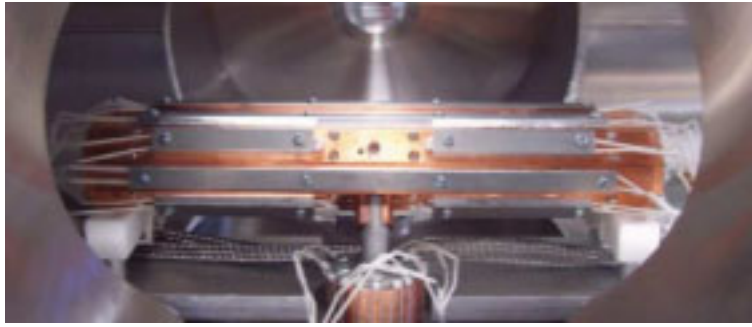


Figure 6.6.: Prototype co-evaporation source mounted into a test vessel.

Within figure 6.5, the gas manifold and container A are shown in a partial cross-section to illustrate the working principle of the co-evaporation source. As the evaporation source is symmetric the following description counts for both containers. The organic material is filled into a BN crucible, which is placed at the bottom of the container. When the container is heated to a temperature above the sublimation temperature, the organic material starts to vaporize. The pressure within the container rises and is released via the feed pipe into the corresponding distribution tube within the manifold. The diameter of the distribution tube was designed to be big enough (20 mm) to guarantee a constant pressure within the manifold tube. As there is no immediate connection between the two distribution tubes, cross-contamination of the containers is not expected. Between the two distribution tubes, small outlet holes of 1.5 mm diameter with a distance of 4 mm to each other establish the gas manifold. The outlet holes are connected in alternation and via beveled drill holes to one of the distribution tubes. Due to the increased pressure within the gas manifold, the molecular vapor is forced through the outlet holes. As these are positioned close enough to each other, the superposition of the sublimation beam of each hole yields a homogeneous deposition profile. The alternation of the outlet holes for material A and material B leads to a perfect mixing of the two materials outside of the manifold. In figure 6.5 this is indicated by two different colors for material A (green) and material B (red). The source was designed for a maximum substrate width of 180 mm. A further outlet hole was drilled into the side wall, directing a molecular beam towards a quartz crystal sensor to measure the film thickness independently for each material.

A prototype co-evaporation source has been assembled according to the described design and was mounted into a test vessel, as shown in figure 6.6. The complete test system consisted of several five-way vacuum crosses and was equipped with a linear transfer system. The maximum substrate size was limited by the transfer system to 100x120 mm². During the deposition the substrate carrier oscillated across the evaporation source ensuring a ho-

mogeneous film deposition along the travel axis. The distance between the outlet holes and the substrate was 35 mm.

6.2.2. thickness and doping profile

For characterization, intrinsic Alq₃ (container A) and DCM2 (container B) layers were deposited and the thickness profiles along the source axis (x) and along the transfer axis (y) were measured using a DEKTAK 8 step profiler. Normalized thickness profiles for both materials along the source axis are shown in figure 6.7a. Dashed lines indicate the mean value, to which the data was normalized, solid lines mark $\pm 5\%$ of the mean value. The deposition profile for Alq₃ shows a significant drop down to 90 % of the mean value 10 mm right of the center position. The thickness stays below the - 5 % mark until 30 mm right of the center position. Further, it rises to about 110 % of the mean value. The thickness profile on the left hand side of the center was determined to satisfy the $\pm 5\%$ uniformity demand. The thickness gradient is rather a singular problem for container A and not a general problem for the whole evaporation source as the thickness profile of the DCM2 layer exposes a uniformity better than $\pm 5\%$ across the whole measurement range of 100 mm. As the source was designed for a maximum deposition width of 180 mm, it is expected that a high uniformity can also be achieved for even bigger substrates than shown here. The non-uniformity of the Alq₃ layer is most likely caused by an angular or dimensional error of a single or several outlet holes.

Figure 6.7b shows the thickness profiles of both layers along the transfer axis. The data sets are normalized to their mean values, which are indicated as dashed lines. Again, solid lines indicate limit values of $\pm 5\%$. Both layers exhibit a very similar thickness profile along the transfer axis, featuring the maximum in thickness at the center of the substrate and decreasing thickness towards the edges of the substrate. The uniformity for the Alq₃ thin film is better than $\pm 5\%$, whereas the acceptance range is exceeded in the case of DCM2. It is possible, that the width of the substrate's oscillation across the evaporation source was not big enough to move the substrate's edge completely out of the wide-angle fraction of the deposition beam. Further, the linear transfer system was powered by a stepping drive. Although a mechanical attenuator was incorporated to the drive, the speed of the substrate's movement along the travel path was discontinuous. Using an advanced transport system will most probably yield a featureless deposition profile and a higher uniformity for both materials.

Next, doped thin films, prepared by co-evaporation of Alq₃ and DCM2, will be presented.

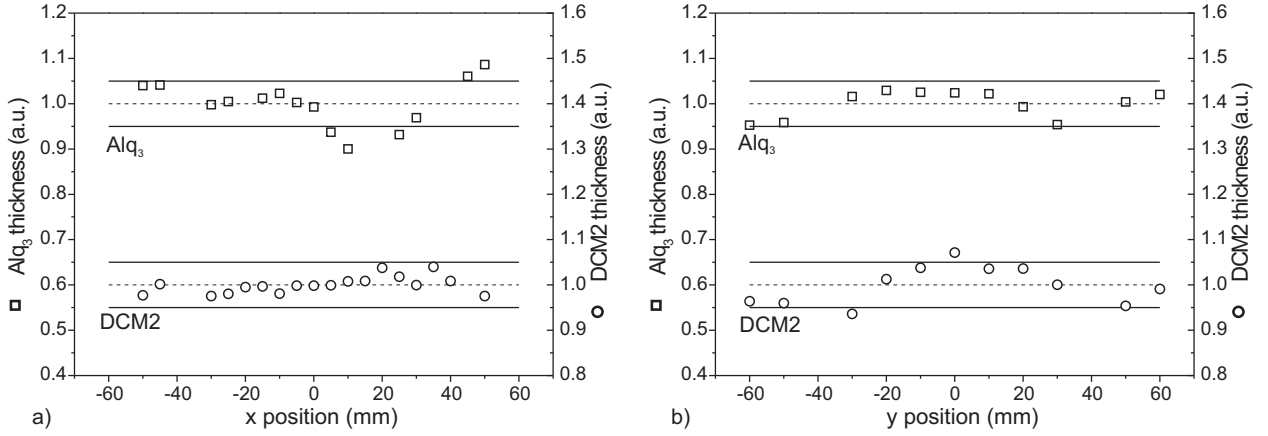


Figure 6.7.: Uniformity of intrinsic Alq₃ (squares) or DCM2 (circles) thin films deposited with the linear co-evaporation source. a) Thickness profile along the source axis. b) Thickness profile along the transfer axis.

Two Si-wafers - 100 x 80 mm² in size - were coated with doped Alq₃:DCM2 layers with different doping concentrations. The targeted doping concentrations (by volume) of the two samples were 3 % and 10 %. As the emission spectra of DCM2 red-shifts with higher concentration, this should be recognized, when both samples are compared. The image in figure 6.8a shows the photoluminescence of these two samples, when exposed to UV light. The expected color difference between the two samples clearly emerges. Bulovic *et al.* correlated the peak emission wavelength of doped OLEDs with the DCM2 doping concentration [163]. The targeted doping concentration for the sample situated on the right hand side of the picture was 3 %, which complies very well with the orange appeal and a peak emission wavelength of about 635 nm. For a doping concentration of 10 % a saturated red color can be observed. Figure 6.8b shows the distribution of the peak emission wavelength across the substrate with saturated red emission. The peak emission wavelength varies between 660 nm and 668 nm. To some extent the distribution of the peak emission wavelengths reproduces what should have been expected from the thickness profiles. Close to the right edge of the substrate, the deposition rate for Alq₃ showed its maximum. This translates into a lower DCM2 concentration which leads to a lower peak emission wavelength, as it can be observed in figure 6.8b. Following, the minimum of Alq₃ thickness measured 10 mm right of the substrate's center axis, leads to a higher doping concentration. As a consequence, the maximum peak emission wavelength appears at approximately 10 mm right of the center. The spectral distribution shows some features which cannot simply be explained by the difference in DCM2 concentration. Therefore it is noteworthy to say, that not only the concentration of DCM2 molecules

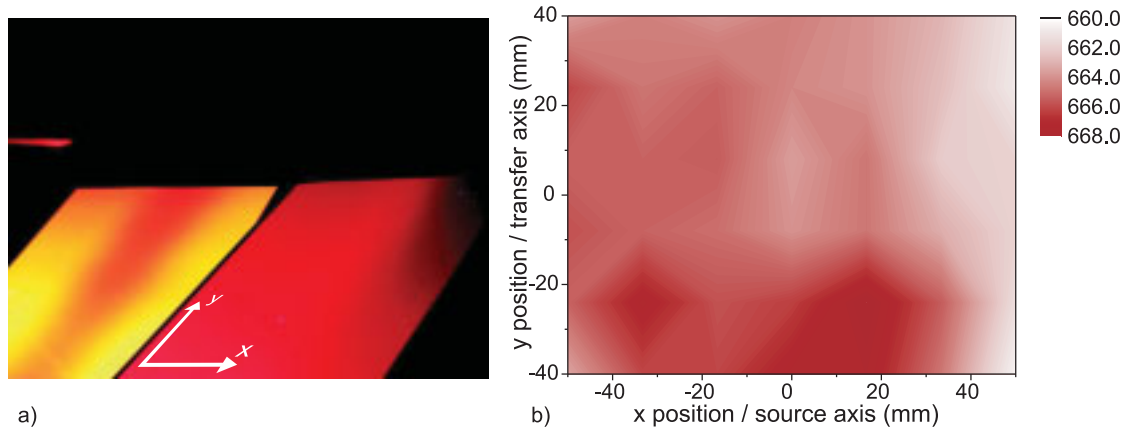


Figure 6.8.: a) Photoluminescence of doped $\text{Alq}_3\text{:DCM2}$ thin films deposited onto Si-wafers. b) Peak emission wavelength of PL spectra of a doped $\text{Alq}_3\text{:DCM2}$ thin film.

affects the emission spectra but also interference effect. The thickness of the $\text{Alq}_3\text{:DCM2}$ layer was approximately 150 nm, so that a substantial fraction of the emitted light is guided in optical thin films modes. As the dispersion of these modes is very sensitive to the thickness of the thin film, thickness variations across the substrate may cause significant shifts of the PL spectrum.

Concluding, a novel type of linear evaporation source, which can be applied for doping of emission and also transport layers, was demonstrated. As the thickness profile of the deposited Alq_3 film along the source axis does not satisfy the uniformity demand, the manifold should be checked for angular or dimensional errors of the gas outlet holes. To avoid this problem in the future, the design of additional linear sources was changed, so that the gas outlet holes were replaced by exchangeable nozzles, which can be fitted into the manifold. By this design, the deposition profile can easily be altered under virtually no assembly effort. Even intentionally corrupted gradient deposition profiles shall be possible. This may be useful as combinatorial technique of depositing a huge number of OLEDs, which gradually differ in the thickness of one certain layer or more. The doping profile qualitatively reproduces the thickness gradient for the Alq_3 layer, exhibiting the lowest respectively highest doping concentration, where the highest respectively lowest Alq_3 deposition rate is observed. So far the cool down rate was very low. As the evaporation rate was maintained at significant levels for more than 15 min after the heating was set to stand-by temperature, large post-process loss of source material is recognized. This implies that the thermal coupling between the cooled shielding and the heated containers was too low and has to be improved for further evaporation sources.

6.3. micropatterning of organic materials

There are mainly three different approaches for realizing full-color OLED-displays (OLED: organic light emitting diode). One of these is color from white by applying a color-filter-matrix to a white-light emitting OLED-display. Another approach is to convert blue light into green and red by a color-converting phosphor matrix (color from blue). Micro-patterning of red, green and blue OLEDs on one substrate is to be favored for reasons of lower costs and higher efficiency.

Shadow masking is the most common patterning technique for vacuum-deposited OLEDs. For this technique a metal mask is placed in a short distance from the substrate. The organic material is deposited only where the substrate is not shadowed by the mask. The major disadvantage of shadow masks is the limited scalability of the mask itself. Thin metal lines of larger shadow masks may oscillate or thermally expand and thereby cause a limited resolution. Currently, shadow masks larger than 1 m^2 cannot be manufactured with high resolution standards [164].

In a solution-based process chain, inkjet printing (IJP) is widely used as patterning technique for mainly polymer light emitting diodes (PLEDs). IJP can be applied to large substrates and allows for a high resolution. As this technique is limited to soluble materials, a fewer number of layers can be utilized, so that the device efficiency will be lower compared to devices prepared under high vacuum conditions.

Researchers from 3M and Samsung lately developed the laser-induced thermal imaging (LITI) process utilizing a CW-laser and galvanometer scanning system for a high-resolution solid-to-solid transfer of thin polymer [165] or molecular [166] films and layer stacks. As the process is a solid-to-solid transfer and needs for intimate contact of the emissive area to the donor film, this may cause problems concerning a lower production yield due to particle contamination.

In 2004, Forrest's group demonstrated a novel patterning technique: Organic vapor jet printing (OVJP) [167]. A hot carrier gas is saturated with the desired material and then led through a microscopic nozzle towards the substrate. They succeeded in printing dots and lines of Alq_3 and pentacene with a resolution of up to 1000 dpi. Within a production system an array of nozzles has to be applied for a realistic throughput. By applying such an array, the production system is limited to one single pattern and changing of this pattern cannot be handled easily.

Prior to this work, a local sublimation method [168] was demonstrated, for which a Mo-film was deposited onto a carrier and patterned by photolithography giving thin stripes. The to be patterned organic material was deposited by organic molecular beam deposition (OMBD)

onto an additional polyimide foil (PI) and brought into intimate thermal contact to the heating element. By heating the Mo-stripes with short high current pulses the organic material could be sublimed locally, which then deposits onto an OLED substrate placed in a short distance from the PI-foil. One of the benefits of this method was the intermixing of different layers of organic material, so that doped systems can be realized without co-deposition of these films. Because of its complex handling and the mechanical alignment, the process will not be suitable for production.

For more flexibility and a more accurate alignment a focused laser beam can be employed as heating source for local sublimation methods. This has already been realized for metal or ceramic thin films, which were removed from a transparent support by short laser pulses and deposited onto a substrate placed within a short distance to the original thin film. The described process is known as laser induced forward transfer (LIFT) [169–172]. The following section describes a local sublimation method technique, which employs a continuous wave (CW) infrared laser.

6.3.1. laser induced local transfer - LILT

The motivation for developing the laser induced local transfer (LILT), is to provide a micropatterning technique for organic materials which satisfies the demands of next-generation production systems. The aim was to realize a patterning system which allows small and precise features at high processing speeds and which is scalable for larger substrate sizes.

Figure 6.9a depicts schematically the working principle of the LILT process [173]. The substrate represents the OLED display substrate onto which the three different emitting materials for red, green and blue emission are to be deposited. The target consists of a transparent support, for example a float glass sheet or polymer foil and is coated with an infrared absorbing material, for example a metal with low reflectivity. Prior to the LILT process the emitting material is deposited on top of the absorbing layer of the target and the hole transporting layer is deposited onto the OLED substrate. If the emitting layer consists of a host and a dopant, these two layers can be deposited sequentially onto the target. The concentration of the dopant can be easily controlled by the ratio of the dopant and host material thicknesses. During the LILT process, a spacer separates the target and the substrate by a distance l_d . As the target feature size is lower than $80\text{ }\mu\text{m}$, the distance l_d should be well below. Therefore, the spacer consists of a thin patterned photoresist layer. When the focused IR laser is scanned along the backside of the target, the absorbing layer locally heats up and the organic material sublimates. If the emitting layer consists of two or more materials, which previously were deposited sequentially onto the target, these materials mix up before condensing on the OLED substrate, so that the emitting material is doped

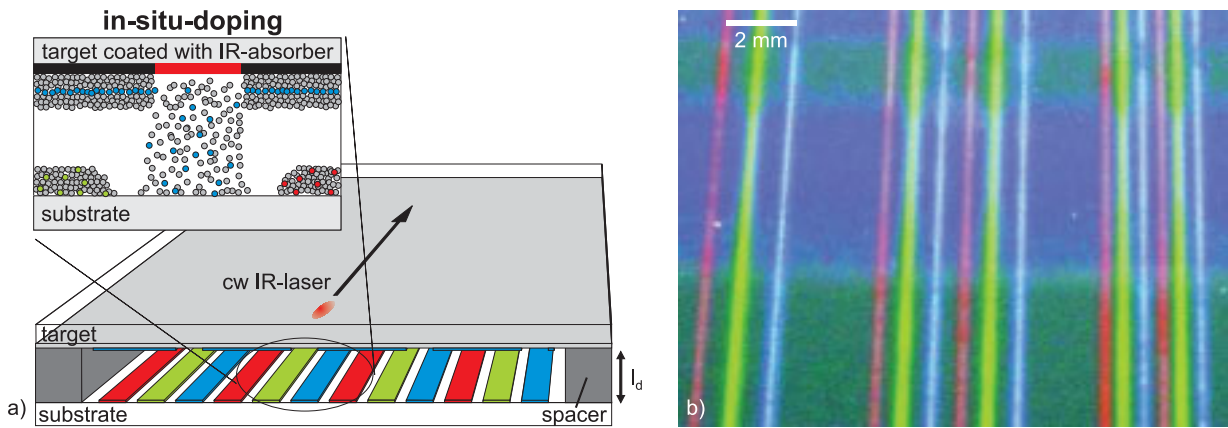


Figure 6.9.: a) Schematic of the laser induced local transfer. b) Photoluminescence image of a substrate, with three different materials patterned by LILT.

in-situ into the host material. The LILT process has to be performed for red, green and blue emitting materials. Afterwards, the electron transporting layers and the metal cathode are to be deposited without patterning, completing the RGB-OLED. For an introductory demonstration, the laser induced local transfer has been employed for the patterning of red green and blue PL stripes, shown in figure 6.9b.

6.3.2. LILT - experimental setup

In general, the setup of laser based micro-machining tools consists of a pulsed or continuous-wave (cw) high-power laser which is directed onto the workpiece. By moving the laser spot relative to the substrate patterns can be generated. The relative movement of the laser spot is either controlled by a fixed laser position and a moving target support or by a fixed target position and a moving laser spot. Former uses high precision optical positioning tables and is for example employed for cutting of plastic circuitry boards (PCB). In the field of OLED displays such a solution has been chosen for the laser patterning of the cathode in polymer passive matrix displays [174]. In applications where the workpiece itself is heavier than the laser system, part of the laser system is moved along the workpiece. For this case, laser welding robotics in the automotive industry gives a good example. Due to the movement of rather high masses, both solutions are inertia-limited and -compared to the demands of the display industry- only low processing speeds and low accelerations are possible.

To demonstrate the feasibility of the LILT process and to qualify the process parameters a galvanometer scanner based solution (ScanLab HurryScan II 10), in which the substrate support is fixed has been chosen. Compared to a fixed laser spot scanned along a moving

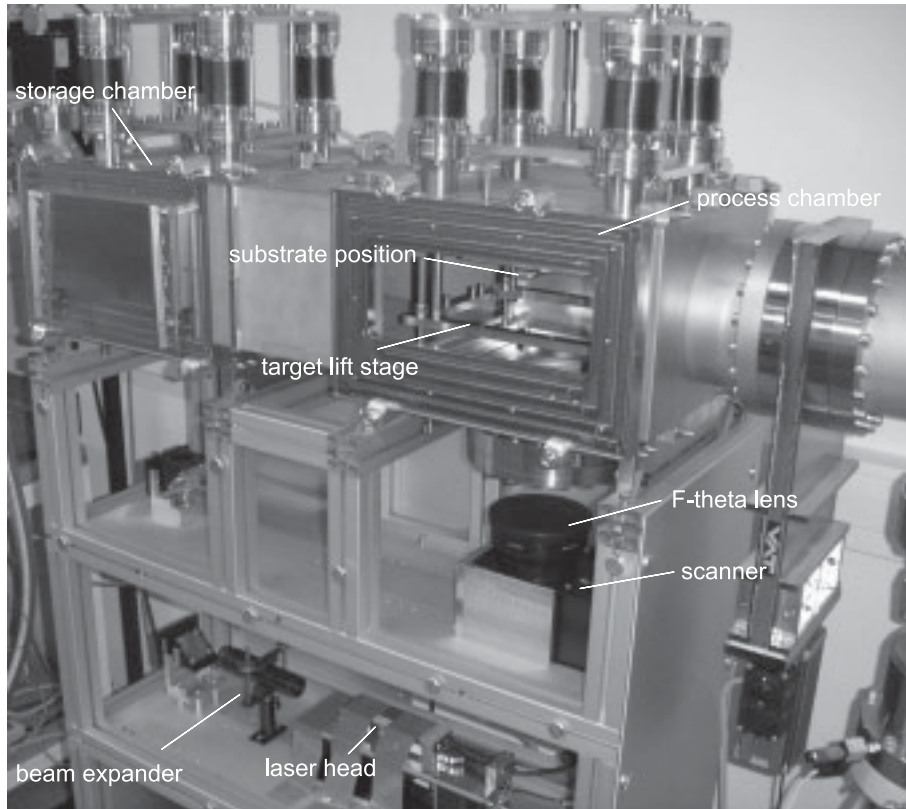


Figure 6.10.: Components of the LILT experimental setup.

substrate, a galvanometer scanner enables extremely high dynamics, a high precision and typical scanning speeds of up to 3-4 m/s as the mirror units within the scanner are the only moving parts and their mass is neglectable in comparison to the mass of optical high precision tables. As the target describes a plain, a so-called F-Theta lens has been employed to map the focus of the laser beam onto the target. The optical system including a Nd:YAG, diode pumped solid state (DPSS) laser (Coherent Compass 2500-4000) is shown in figure 6.10.

For ensuring highest beam quality the laser source is operating in the TEM_{00} mode at a wavelength of 1064 nm. The optical output power is controlled by a feedback loop and can be adjusted from 100 mW up to a maximum output of 4 W. Furthermore a collimating and beam expanding lens has been used to properly adjust the diameter of the laser beam and the working distance between the surface of the F-Theta lens and the target. Two fine-tunable Ag mirrors allow to exactly match the beam position and parallelism with the entry axis of the scanner. The focal length f of the F-Theta lens determines the working distance, the area of the working field and the minimum beam diameter. The chosen lens with a focal length of 254 mm has a working distance of about 290 mm and provides a working area of

160 x 160 mm². The minimum beam diameter D_{min} can be calculated from the focal length f , the beam diameter D_0 (here: 10 mm) on the focusing F-theta lens and the wavelength λ and is described by the following equation:

$$D_{min} = \frac{4f\lambda}{\pi D_0} \quad (6.1)$$

The configuration chosen for the process development allows to achieve a focus diameter of approximately 35 μ m.

As the process shall later be integrated into an inline deposition system, custom vacuum chambers, which may serve as inline process modules, have been designed. Figure 6.10 shows a picture of two of these modules, connected via their side flanges. In an inline deposition tool one chamber serves as target storage for at least three different targets which can be selected independently and transferred into the LILT process chamber. The latter is equipped with a fixed substrate position and a glass window at the bottom under which the scanner is placed. It has been calculated, that disturbances of the image quality due to longer optical paths or a higher reflection under different angles, can be neglected. As this system displays only one process module of a future inline system, no evaporation sources for the transport materials or metal contacts are present, so that the during the preparation of LILT-patterned OLED devices two vacuum breaks occur.

6.3.3. physical description of the LILT process

Before the experimental results are to be discussed, a physical description of the LILT process shall be given. The dominating physical processes are displayed in figure 6.11, and shall be explained in detail.

I) absorption

The organic layers do not sufficiently absorb the laser light at 1064 nm to generate enough heat for sublimation. Therefore an absorption layer has been employed to convert the radiation into heat. It showed that among several metals and semiconductors, thin films of Ti proofed a sufficient light absorption, superior thermal properties and a very good adhesion to the target support (float glass) during the process. Freshly sputtered Ti surfaces rapidly oxidize upon exposure to ambient air, so that the surface should be chemically inactive. As all investigations presented in section 6.3.4 were undertaken by targets employing Ti absorbing layers, in all model calculations the physical properties of sputtered Ti thin films will be

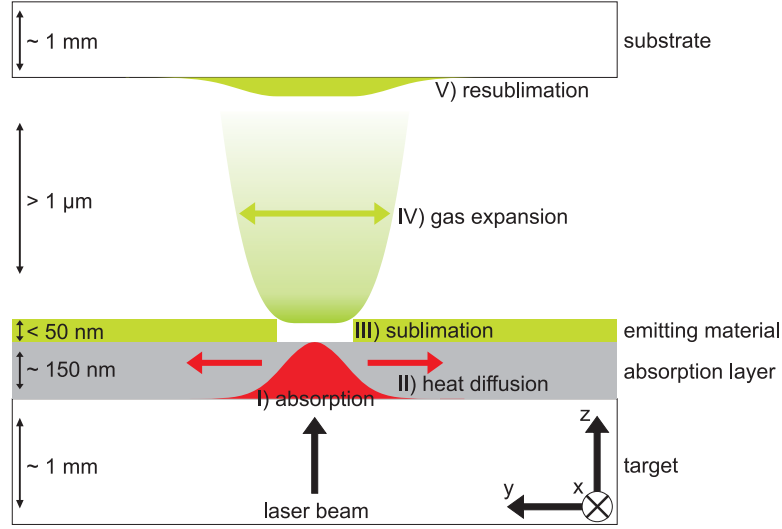


Figure 6.11.: Schematic of the physical phenomena dominating the LILT process.

considered.

First the absorbed laser intensity should be estimated. As the lenses within the beam expanding telescope and the F-Theta lens are coated with optical anti-reflection layers and the dielectric mirrors of the scanner are designed to provide a reflectivity of nearly 100 % only the limited reflectivity of the two positioning mirrors, the fresnel reflections at the bottom viewing port of the vacuum chamber and at the bottom side of the target account to the estimated optical power losses of about 15 % before the laser beam hits the absorption layer². As the thickness of the Ti absorption layer was 150 nm and sufficient to not allow significant light transmission, the absorption ratio A equals the difference between the reflection coefficient R and 100 % and can be calculated by the following equation:

$$A = 1 - R = 1 - \frac{|n_1 - (n_2 - jk_2)|^2}{|n_1 + (n_2 - jk_2)|^2}. \quad (6.2)$$

Here, n_1 indicates the refractive index of the target glass sheet and is assumed to equal 1.5. The optical properties of the absorption layer are represented by the refractive index n_2 and the extinction coefficient k_2 . Considering literature values for Ti thin films of n_2 equaling 3.46 and k_2 given as 4.01 [175], A is calculated to equal nearly 50 %. Taking the optical losses of the path towards the substrate an overall ratio η_{abs} of 42 % of the laser radiation

²The laser beam is deflected by two Ag-coated mirrors, each of which possesses a typical reflectance R of 98 %. The technical data sheet of the standard grade viewing port gives a value of 92 % for transmission. The refractive index n of the target glass sheet was assumed to be 1.5, giving a transmission coefficient at the interface of about 96 %.

emitted is converted into heat.

As mentioned before, the infrared laser is operated in the TEM₀₀ mode which can be described by a gaussian intensity profile I given by

$$I(x, y) = \frac{4P}{D_0^2\pi} e^{-4\frac{(x-x_0)^2+(y-y_0)^2}{D_0^2}}. \quad (6.3)$$

In equation 6.3, x and y represent orthogonal coordinates within the working plain of the f-Theta lens, x_0 and y_0 determine the center position of the profile within the working field, P is the laser output power, and D_0 represents the beam diameter, which may be different to D_{min} , due to optical misalignment of the system. Now a scan along the x-axis with a constant scanning speed v_x shall be assumed. This means that x_0 becomes time-dependent and y_0 is set to be zero. Then the time-dependent intensity profile $I(x, y, t)$ can be expressed as

$$I(x, y, t) = \frac{4P}{D_0^2\pi} e^{-4\frac{(x-x_0(t))^2+y^2}{D_0^2}} = \frac{4P}{D_0^2\pi} e^{-4\frac{(x-v_x t)^2+(y)^2}{D_0^2}}. \quad (6.4)$$

The integration of equation 6.4 over time - limits set to infinity - yields the fluence profile along the y -axis:

$$\Phi(y) = \frac{2P}{D_0 v_x \sqrt{\pi}} e^{-4\frac{y^2}{D_0^2}}. \quad (6.5)$$

When equation 6.5 is linked to the thermodynamic properties of the composite target the heat distribution can be derived.

II) heat diffusion

The heat diffusion in the target is described by the three dimensional time dependent heat equation:

$$c\rho \frac{\delta T}{\delta t} = \frac{\delta U}{\delta t} + K \left(\frac{\delta^2 T}{\delta x^2} + \frac{\delta^2 T}{\delta y^2} + \frac{\delta^2 T}{\delta z^2} \right). \quad (6.6)$$

In the given equation T represents the temperature, c the specific heat, ρ the density, K the thermal conductivity and the term $\frac{\delta U}{\delta t}$ takes internal heat sources into account. For the described problem equation 6.6 can only be solved numerically as the Gaussian heating profile and discontinuities at the layer boundaries do not allow an analytical solution. A numerical solution of a problem close to the given one has already been reported [174]. As the cited solution did not include phase transitions and thermal impedances at interfaces between different layers, it may not be suitable to display the heat diffusion during the LILT process. Therefore a different approach of determining the temperature profile by approximating the physical model will be described.

To include a possible broadening of the local heat distribution in the target's absorption

Table 6.2.: Physical properties of the materials employed for the target: specific heat c , heat conductivity K and density ρ , thermal diffusivity κ ; materials: Alq₃, Ti, glass (Pyrex 7740).

material	c [$Jg^{-1}K^{-1}$]	K [$Wm^{-1}K^{-1}$]	ρ [gcm^{-3}]	κ [m^2s^{-1}]	references
Alq ₃	1.03	0.107	1.282	$8.1 \cdot 10^{-8}$	[178]
Ti	0.57	5.02	4.507	$2.4 \cdot 10^{-6}$	[177, 179]
	-bulk-	-bulk-	-bulk-	-thin film-	
glass	0.85	1.25	2.23	$6.6 \cdot 10^{-7}$	[180]

layer, it has to be checked whether the timescale of thermodynamic relaxation processes in the target are in the same order of magnitude as the duration of the laser induced heating. The heating period t_h is estimated by the beam diameter D_0 and the scanning speed v_x to be $t_h = D_0/v_x$. For example, the duration of the heating period for a scanning speed of 1 m/s and the discussed optical setup is 35 μ s. The thermodynamic relaxation within the target is determined by the thermal properties of the participating materials. Table 6.2 gives thermodynamically relevant physical properties of the materials which constitute the target. As the thermal properties of only a few organic materials are referenced, Alq₃ has been chosen as model material for the emission layer. Above, the energy density, which is absorbed during a scan along the x-axis, has been shown to be independent of the x-coordinate. Therefore only two-dimensional heat flow within the y-z-plane shall be discussed. Sputtered Ti layers show a polycrystalline growth in (100) and (001) orientations with very small grain sizes [176], so that an isotropic heat transport is assumed not only for the amorphous Alq₃ layer and the glass sheet but also for the absorption layer. For metals the heat flow is mainly carried by conducting electrons which are excited by the laser and then thermalize due to lattice scattering. The thermal diffusion length l_{th} in this case can be approximated to [177]:

$$l_{th} \approx \sqrt{\kappa t}. \quad (6.7)$$

Due to the lack of free charge carriers in the glass sheet and the organic layers, the heat transport in these materials has to be explained by phonon coupling. Although a different mechanism accounts for the heat transport in these layers, the given approximation for L_{th} will be accepted for the further discussion for all layers.

First the heat diffusion perpendicular to the substrate plane should be regarded. The laser intensity is absorbed within the optical skin depth, which correlates with the extinction coefficient k and equals 21 nm for Ti at a wavelength of 1064 nm. During a certain period of

time t_d the heat diffuses a length which equals the layer thickness l_t of the absorption layer or of the organic layer. Taking equation 6.7, the diffusion time can be expressed as $t_{d,z} = l_t^2/\kappa$. The layer thickness was 150 nm for the absorption layer and will be lower than 100 nm for the organic emission layer (depending on OLED) resulting in diffusion times of approximately 9 ns for the absorbing layer and 124 ns for the organic layer. Even for very high scanning speeds of several m/s the heating time t_h is in the μ s-range and exceeds the diffusion time $t_{d,z}$ for both Ti absorption and Alq₃ emission layer by several orders of magnitude. Therefore the diffusion times for thermal diffusion across the thickness of the layers can be neglected and will not be considered for the further discussion. Instead, instant heating and equal temperatures for the absorption layer and the emission layer are assumed.

As explained before, the discussion of the in-plane heat diffusion is limited to the y-coordinate. During the period of time the laser moves along a certain spot part of the thermal energy diffuses into the surrounding material. The thermal diffusion length for the different materials is approximated by setting the diffusion time in equation 6.7 equal to the heating time t_h :

$$l_{th} \approx \sqrt{\kappa t_h} = \sqrt{\frac{\kappa D_0}{v_x}}. \quad (6.8)$$

Table 6.3 indicates the thermal diffusion lengths within the materials which were employed for the target for different scanning speeds. Because the thermal diffusion length within the Ti absorption layer is greater than those of the underlying glass sheet and the organic layer, thermal diffusion along the y-axis is dominated by the thermal properties of the Ti layer. It is most likely that the temperature distribution along the y-axis during the heating period will also follow a gaussian function, but significantly broadened compared to the fluence profile. Therefore, the following equation represents a valid assumption for the local temperature rise during the heating period:

$$\Delta T_{local}(y) = \Delta T_0 e^{-4 \frac{y^2}{(D_0 + 2l_{th,Ti})^2}}. \quad (6.9)$$

The amplitude factor ΔT_0 is yielded when equation 6.5, which describes the fluence profile Φ , is linked to the local temperature rise, given by equation 6.9. The amount of energy added to the system can either be expressed by the integrated fluence Φ weighed with the absolute ratio of absorbed light η_{abs} , or by the integral of the local temperature rise ΔT_{loc} multiplied with the thermal capacity $c\rho$. The integration limits for the x-coordinate are set to $\pm\Delta x/2$ and are set to $\pm\infty$ for the y- and z-coordinate:

Table 6.3.: Diffusion length l_th dependent of the scanning speed along the x-axis v_x for materials employed for the target.

v_{scan} [m/s]	$l_{th,Alq}$ [μm]	$l_{th,Ti}$ [μm]	$l_{th,glass}$ [μm]
0.5	2.4	13.0	6.8
1.0	1.7	9.2	4.8
2.0	1.2	6.5	3.4
3.0	1.0	5.3	2.8

$$\begin{aligned}
\Delta E &= \int_{-\frac{\Delta x}{2}}^{\frac{\Delta x}{2}} \int_{-\infty}^{\infty} \eta_{abs} \Phi dx dy = \int_{-\frac{\Delta x}{2}}^{\frac{\Delta x}{2}} \int_{-\infty}^{\infty} \int_{-\infty}^{\infty} c\rho \Delta T_{loc} dx dy dz \\
\Delta x \stackrel{\Delta x \ll l_{th}}{\Rightarrow} \Delta x \int_{-\infty}^{\infty} \eta_{abs} \frac{2P}{D_0 v_x \sqrt{\pi}} e^{-4\frac{y^2}{D_0^2}} dy &= \Delta x \int_{-\infty}^{\infty} \int_{-\infty}^{\infty} c\rho \Delta T_0 e^{-4\frac{y^2}{(D_0+2l_{th,Ti})^2}} dy dz.
\end{aligned} \tag{6.10}$$

For $\Delta x \ll l_{th}$ the assumption that ΔT_{loc} does not depend on the x-coordinate is true, and the integral is solved to a constant Δx on both sides of equation 6.10. The z-dependence of the temperature distribution can be estimated to be a constant within the thermal diffusion length and to be zero above.³ As the thermal diffusion length for the organic and for the absorption layer is greater than the actual layer thickness, only the layer thickness has to be considered for the thermal capacity. Compared to the thermal diffusion length within the glass support, these layers are very thin, so that their contribution to the thermal energy of the whole system can be neglected. This leads to the following simplification:

$$\begin{aligned}
\int_{-\infty}^{\infty} c\rho \Delta T_{loc} dz &= (c_{glass}\rho_{glass}l_{th,glass} + c_{Ti}\rho_{Ti}l_{t,Ti} + c_{Alq}\rho_{Alq}l_{t,Alq})\Delta T_{loc} \\
&\stackrel{l_{th,glass} \gg l_{t,Ti}, l_{t,Alq}}{\approx} c_{Glass}\rho_{glass}l_{th,glass} \Delta T_{loc}.
\end{aligned} \tag{6.11}$$

The integration of the gaussian function on both sides of equation 6.10 and applying the simplification given by equation 6.11 delivers the value of the amplitude factor ΔT_0 :

³Describing the z-dependence by an exponential decay would be formally more correct, but as in the end the same result is yielded, a simpler description is preferred.

$$\begin{aligned}
\Delta T_0 &= \frac{2\eta_{abs}P}{\sqrt{\pi} v_x c_{glass} \rho_{glass} l_{th,glass} (D_{min} + 2l_{th,Ti})} \\
&= \frac{2\eta_{abs}P}{\sqrt{\pi} v_x \kappa_{glass} D_{min} c_{glass} \rho_{glass} (D_{min} + 2\sqrt{\frac{\kappa_{Ti} D_{min}}{v_x}})}. \tag{6.12}
\end{aligned}$$

III) sublimation

When the local temperature T_{loc} rises above the critical temperature T_{crit} , the organic emission layer sublimates. Although there may be a difference for materials which sublime on the one side and those which melt and evaporate on the other, both cases are generalized to direct flash sublimation, as the timescale on which the sublimation/evaporation happens is in the μs -range. Within a certain width $W_0 = 2y_{crit}$ the local temperature rise ΔT_{loc} exceeds the critical temperature rise ΔT_{crit} . The width of the sublimed stripe can be derived from the local temperature difference ΔT_{loc} , given by equation 6.9:

$$\begin{aligned}
\Delta T_{crit} &= \Delta T_0 e^{-4 \frac{y_{crit}^2}{(D_0 + 2l_{th,Ti})^2}} \\
\Rightarrow W_0 = 2y_{crit} &= (D_0 + 2l_{th,Ti}) \sqrt{\ln \frac{\Delta T_0}{\Delta T_{crit}}}. \tag{6.13}
\end{aligned}$$

It has to be pointed out, that during the development of the heat distribution not all assumptions, which were made, are literally indicated. Furthermore some of these may not comply with the physical reality. Two examples shall be given. First, the heat diffusion across the absorption layer does not stop after the laser pulse passed that certain position. This leads to a further broadening of the temperature profile. If now the energy density is high enough that the local temperature rises above the critical temperature a broader line width W_0 will be observed. This effect will influence W_0 more for a higher energy density, meaning a higher laser power. Secondly, the specific heat was -without notice- assumed to be constant. In reality the specific heat is a function of temperature, and rises with higher temperatures. This leads to an overestimation of the calculated temperature profile.

IV) gas expansion

The flash sublimation of the organic material leads to a drastically increased pressure close to the target. As the gas expands the sublimation plume and thereby the deposition profile

on the substrate is broadened with increasing distance d between target and substrate. First the local pressure and the mean free path of the molecules shall be estimated. The ideal gas law states

$$pV = Nk_B T, \quad (6.14)$$

where p is the absolute pressure, V the volume, N the number of molecules, T the temperature and k_B Boltzmann's constant. During the heating period t_h the sublimation plume expands to a mean distance $d_m = t_h v_m$, where v_m is the mean velocity of gas molecules, which follows from the kinetic theory of gases as a function of temperature and molecular mass m_M :

$$v_m = \sqrt{\frac{3k_B T}{m_M}}. \quad (6.15)$$

As an example, the mean velocity of Alq₃ molecules at 500 K, which is assumed to be slightly above the sublimation temperature T_{sub} , is about 50 m/s. This means that during the heating period t_h the sublimation plume would expand to a distance of more than 1 mm. As this is several orders of magnitude higher than the distance between target and substrate, only l_d shall be considered. For a rough estimation of the local pressure p_{loc} between target and substrate equation 6.14 can be approximated by setting the temperature T to the sublimation temperature T_{sub} , substituting V by $\Delta V = \Delta x \Delta y d$, and expressing N as $N = \Delta x \Delta y l_{t,org} \frac{\rho_{org}}{m_M}$:

$$p_{loc} = \frac{l_{t,org} \rho_{org} k_B T_{sub}}{l_d m_M}. \quad (6.16)$$

For Alq₃ a molecular mass of 459.44 and 1.282 g/cm³ as thin film density have to be applied. Further a distance l_d of 5 μ m, and a layer thickness of 50 nm are assumed, so that the local pressure P_L can be roughly estimated to be in the order of 1000 mbar. This result is not intended to be completely correct, but should demonstrate, that the local pressure during the flash sublimation is several orders of magnitude larger than the background pressure within the vacuum system and two conclusions can be drawn from this fact. First, the local temperature on the target will be higher than the temperature applied for high vacuum sublimation from quartz crucible effusion cells. Second, the mean free path between two collisions of Alq₃ molecules is in the range of a few nanometers. This means, the molecules experience so many collisions before they resublime on the substrate, so that the deposition is dominated by diffusion and is expected to be normally distributed. Under these conditions host and dopant material, which were deposited as separate layers, completely mix up during the deposition. The broadening of the sublimation plume is described by a distribution f_s for a hypothetical one-dimensional source along the x-axis as a function of distance l_d between

target and substrate:

$$f_s(y) = \frac{l_t}{\omega_0 l_d \sqrt{\frac{\pi}{2}}} e^{-2 \frac{y^2}{(\omega_0 l_d)^2}}. \quad (6.17)$$

In equation 6.17, ω_0 refers to the broadening of the sublimation plume and is dependent on several process parameters. Among these the background pressure, the scanning speed, the laser power and the material, which is to be sublimed, are expected to exert a dominant influence. Due to the complex interaction, which by far would exceed the scope of this section, and unknown material properties for most of the organic materials, the gas expansion factor ω_0 cannot be derived from physical models and will therefore be derived from the experimental data in section 6.3.4.

V) resublimation

The substrate is kept at room temperature. Organic molecules hitting the surface are instantly absorbed. Due to the low temperature of the substrate, reflection and movement of the surface molecules can be neglected. Then, the deposition profile on the substrate only reflects the line width of the sublimated stripe on the target and the diffusion induced broadening of the sublimation plume. The superposition of the distribution function f_s along the width of the sublimated stripe, which can be described by a rectangular function $g_t(y) = l_{t,org} \text{rect}(\frac{y}{W_0})$, leads to

$$l_{sub}(y) = (f_s * g_t)(y) = \int_{-\frac{W_0}{2}}^{\frac{W_0}{2}} \frac{l_{t,org}}{\omega_0 l_d \sqrt{\frac{\pi}{2}}} e^{-2 \frac{(y-\tau)^2}{(\omega_0 l_d)^2}} d\tau. \quad (6.18)$$

In the further context, the integral will be approximated by a limited number N of distribution function f_s equally distributed along the y-axis, leading to

$$l_{sub}(y) = \sum_{i=-\frac{N}{2}}^{\frac{N}{2}} \frac{l_{t,org} W_0}{(N+1) \omega_0 l_d \sqrt{\frac{\pi}{2}}} e^{-2 \frac{(y-i\frac{W_0}{N})^2}{(\omega_0 l_d)^2}}. \quad (6.19)$$

For $N \rightarrow \infty$, the progression develops into equation 6.18. Two extremes shall be discussed. In the first case, the gas diffusion factor $\omega_0 l_d$ is much broader than the width of the sublimated stripe W_0 . Now the profile of the deposited stripe on the substrate reflects the broadening of the sublimation plume and can be approximated by a gaussian function. If on the other hand $W_0 \gg \omega_0 l_d$ is valid, the deposition profile is expected to resemble the profile of the sublimated stripe on the target, having a flat top but with blurred edges compared to a rectangular function. This case is to be favored, as a homogeneous thickness distribution

across single pixels is desired for reasons of uniformity, efficiency and lifetime. In high-resolution applications W_0 will be limited by the customer's demands, ω_0 is a characteristic of the patterning process which cannot be changed, so that only the distance between target and substrate l_d can be adjusted to meet the specifications. For the process development, l_d has been chosen to be $1\mu\text{m}$, which in production can easily be achieved by using the passivation layer of the active matrix-backplane as spacer.

6.3.4. LILT - process development

Goal of the process development is to gain information about how the characteristics of the deposited organic materials evolve upon parameter variation. Parameters which can be varied are the scanning speed, the laser power and the distance between target and substrate. The experimental details will be related to the approximated physical model, which was introduced in the previous section.

6.3.4.1. Alq_3 as archetype material

Due to the early and widespread use of Alq_3 during two decades of OLED research, it is the most explored material employed for organic light emitting diodes. Therefore it serves well as model material to evaluate the laser induced local transfer. Figure 6.12 shows microscopic images of the target and the substrate after both were patterned. The laser beam was scanned along the target with 2.5 m/s , the optical output power of the laser was 3 W . As the thin stripe deposited onto the substrate is highly transparent, the contrast under visible light illumination is very poor. Upon UV-light illumination, the pattern on the substrate can be clearly identified by the characteristic green photoluminescence of the Alq_3 molecules. Therefore, for all microscopic measurements on substrate and target these were UV-illuminated to enhance the contrast ratio. It can be seen, that on the image of the target (figure 6.12.a) a sharp edge defines the pattern and the line width can easily be measured, whereas the pattern on the substrate (figure 6.12.b) does not show a sharp edge. The PL intensity is gradually decreasing with distance from the center, indicating a gradient thickness distribution. This observation gives evidence to the fact that the expansion of the sublimation plume strongly influences the deposition profile even at a very short distance l_d of $1\mu\text{m}$ between target and substrate and a gaussian-like deposition profile is expected. At first sight both observations comply with the model description given in section 6.3.3.

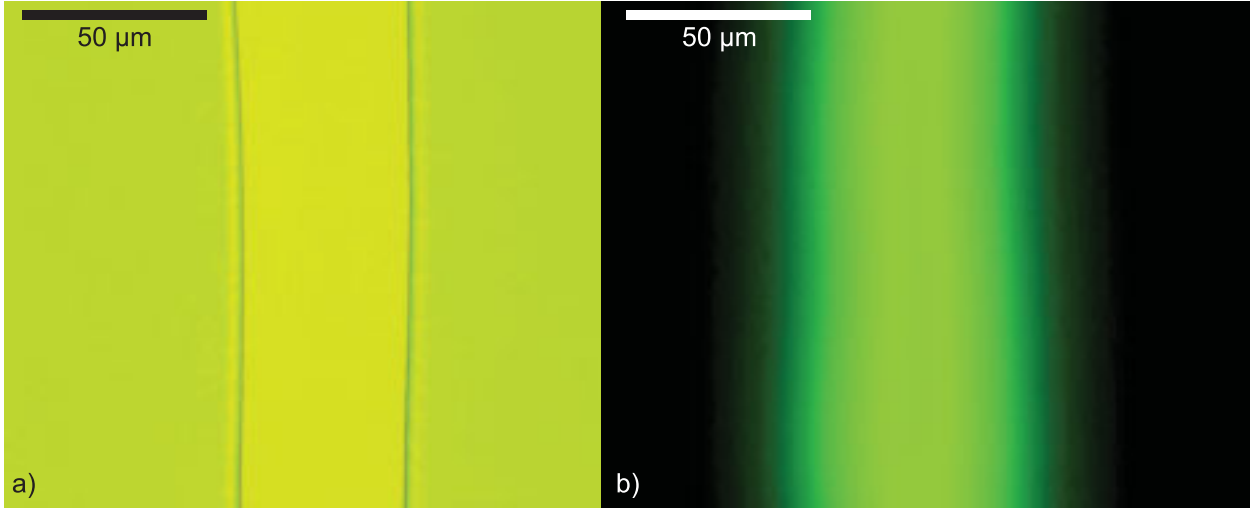


Figure 6.12.: Microscopic photoluminescence images of a) the LILT patterned target and b) the corresponding substrate.

target line width vs. scanning speed and laser power

First the influence of scanning speed v_x and laser output power P should be verified by measuring the line width of the pattern on the target. Therefore several targets were patterned at different scanning speeds and laser output powers. In figure 6.13.a the on-target line width is plotted against scanning speed, taking the optical output power of the laser as a further parameter. The experimental data is fitted by equation 6.13 (solid lines). The unknown parameters D_0 and ΔT_{crit} are employed as fitting parameters. All other parameters are fixed to the values given in section 6.3.3. It can be observed that the approximated physical model accurately reproduces the experimental data. For the given data D_0 is determined to be $47 \pm 4.4 \mu\text{m}$. As displayed in figure 6.13.b, the critical temperature rise ΔT_{crit} is not a constant over laser power and is in the range of 600 K or above. This would mean, that the local temperature rises to more than 600 °C during the sublimation, as the local temperature before the process equals room temperature. This may be confusing, because the sublimation temperature of Alq_3 is well below the given value. Considering that the local temperature is overestimated due to the assumption of a constant specific heat and that the heat diffusion is underestimated for higher laser power, it seems clear, that this must be reflected within ΔT_{crit} as the remaining fit parameter. Therefore it has to be pointed out, that ΔT_{crit} shall not be taken as the actual temperature above which Alq_3 sublimates under flash conditions, but can be used to quantify the dependence of the target line width on scanning speed and laser power. The characteristic of ΔT_{crit} over laser power follows a second order polynomial,

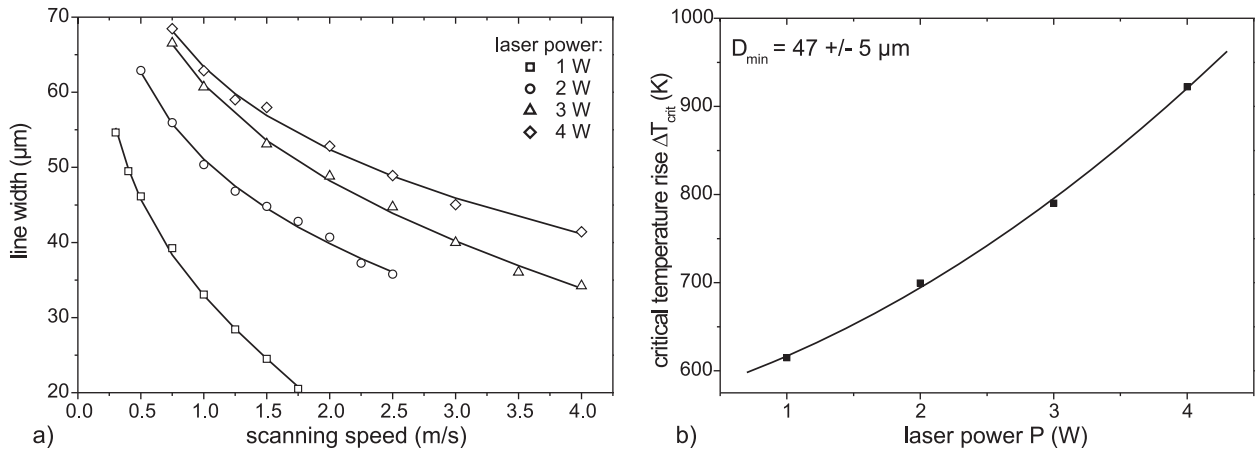


Figure 6.13.: a) Width of the patterned stripes on the target vs. scanning speed for various laser output powers (open symbols). b) ΔT_{crit} vs. laser output power.

which is displayed in figure 6.13.

The experimental results suggest, that equation 6.13 perfectly describes the pattern width on the target as a function of scanning speed and output laser power. From equation 6.13 several conclusion for the current and future LILT configurations can be drawn. Firstly, as the thermal diffusion length depends on the thermal diffusivity ($\kappa = \frac{K}{\rho c}$), materials with lower thermal conductivity allow for higher resolution when patterned. Due to the low thermal conductivity, Ti thin films are under this aspect perfectly suited as absorption layer. When Ti thin films are used as absorption layer, the thermal diffusion length $l_{th,Ti}$ is low, compared to the given beam diameter W_0 . This leads to the second conclusion. Reducing the beam diameter by means of a more proper optical adjustment and a shorter wavelength, will lead to a drastically reduced pattern dimension. According to equation 6.1 the minimum beam diameter D_{min} for a green Nd:YAG with 532 nm emission wavelength is $17.4 \mu m$. As the local temperature coefficient ΔT_0 is directly proportional to the laser output power and antiproportional to the actual beam diameter plus the thermal diffusion length, a reduction of the beam diameter would also lead to less laser power needed for the LILT process. This is not an important feature for the demonstrated laboratory setup, but in production systems, where the laser beam can be splitted for parallelized patterning, the installed laser output power will be a cost factor, which -by chance- has to be reduced.

In equation 6.11 the thermal energy stored within the composite target is approximated by the thermal energy stored within the underlying glass support. This approximation also strikes the value of the local temperature coefficient ΔT_0 , so that ΔT_0 shows an antiproportional dependence of the thermal properties of the underlying glass sheet. If now the target

support is exchanged by a material with a lower thermal conductivity -for example a thin polymer sheet-, the laser output power can be downscaled even more.

substrate thickness distribution

In section 6.3.3 the thickness distribution on the target is approximated by a superposition of Gaussian distribution functions f_s . Although the microscopic PL image in figure 6.12 supports this prediction in a qualitative manner, it is not suitable to determine the thickness distribution. Therefore, the deposition profiles of stripes patterned onto the substrate were measured by coherent interferometry [181]. The results are presented in figure 6.14. Within the two-dimensional scan the thickness is indicated by the color from blue to red representing low to high thickness. As expected the width of the deposited stripe decreases for increasing scanning speed, while keeping the output laser power constant at 3 W. This corresponds to the decreasing line width observed on the target. This observation is quantified by the thickness profile along the y-axis, also shown within each of the scans in figure 6.14. The profile represents the average value of the first 200 lines of the experimental data. The experimental data is fitted by a Gaussian distribution. For higher scanning speeds, a Gaussian distribution resembles the thickness profile very well, but for lower scanning speeds a single Gaussian function does not fit the experimental data satisfyingly. This has been predicted in the previous section. To illustrate this observation, the thickness profile of three different scanning speeds, equivalent to three different source line widths on the target, have been picked and are displayed in more detail in figure 6.15a.

It has been pointed out previously, that the thickness profile on the substrate is affected by the broadening of the sublimation plume and by the width of the sublimated stripe on the target. Latter is calculated from equation 6.13 to be $61.03 \mu\text{m}$, $48.21 \mu\text{m}$ and $40.21 \mu\text{m}$ for a scanning speed of 1 m/s, 2 m/s and 3 m/s, respectively. For the highest scanning speed, a Gaussian fit matches the experimental data very well. This indicates that the broadening of the sublimation plume dominates the deposition profile. For slower scanning speeds a significant discrepancy between the experimental data and the corresponding fit arises. It is obvious that the increasing line width on the target is reflected in the thickness profile on the substrate. Therefore a multi Gaussian fit according to equation 6.19 may be more precise and was performed for each of the thickness profiles shown in figure 6.14. The broadening factor ω_0 and the organic layer thickness on the target $l_{t,org}$ were taken as fit parameters to minimize the gap to the experimental data. All other parameters were fixed and can be derived from table 6.4. To compare the multi Gaussian fit to a single Gaussian distribution, figure 6.15.b shows the same set of experimental data, but now the solid lines represent the corresponding multi Gaussian fit. At slower scanning speeds a difference between the two

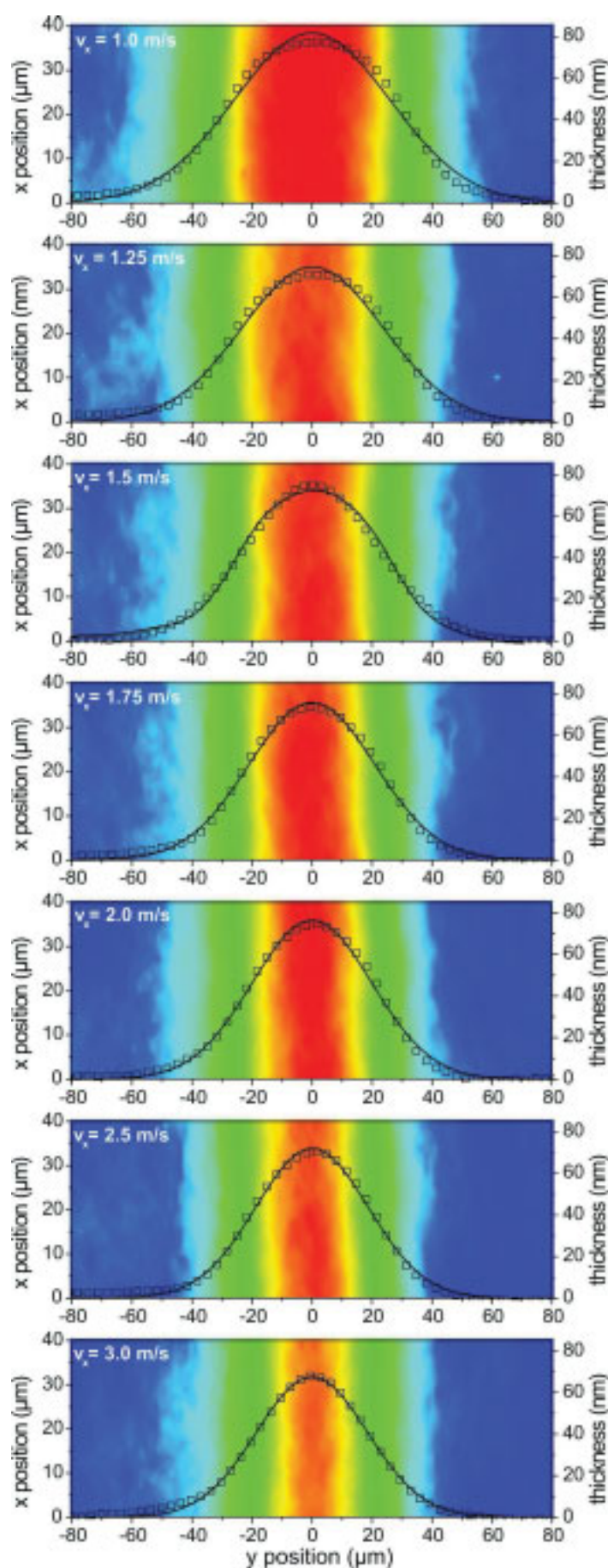


Figure 6.14.: Interferometric scan of the thickness distribution on the substrate for varying scanning speeds. The scanning speed is indicated in the top left corner of each scan image. The laser output power was 3 W. Within each of the scans the thickness profile along the y axis is shown. Open symbols represent the experimental data integrated over 200 lines. The solid line represents a Gaussian distribution fitted to the experimental data.

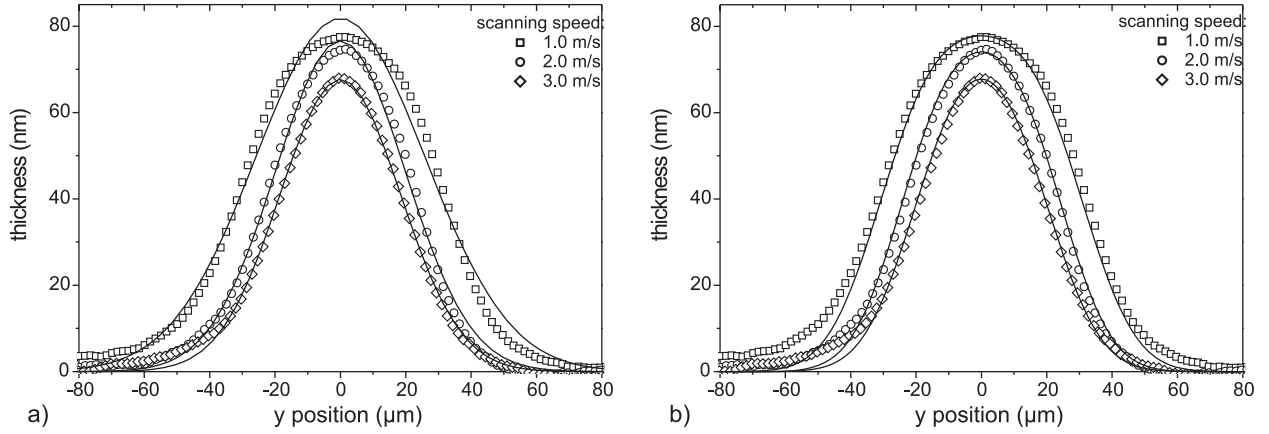


Figure 6.15.: Thickness profile of patterned stripes on the substrate. The experimental data is displayed as open symbols, solid lines represent a) a single Gaussian distribution, b) a superposition of several Gaussian distributions, fitted to the experimental data.

fitting functions arises, where the multi Gaussian distribution very closely approximates the thickness profile and the single Gaussian function fails to reproduce the experimental data. The fitting parameters ω_0 and $l_{t,org}$ are included in Table 6.4. As the values of these parameters are very close for different scanning speeds and the fitted thicknesses $l_{t,org}$ comply with that determined by surface profilometry⁴, the model description given by equation 6.18 gives a very close approximation within the observed parameter range. The mean value of the gas expansion factor ω_0 accounts for 26.4 and will be used for further model calculations.

6.3.4.2. materials

Today, highly efficient OLEDs mostly employ phosphorescent emitter materials which are doped into wide band gap transport materials like TCTA or TPBi. It has to be checked whether the LILT process can be applied to a variety of host materials, or if restricts the choice of applicable materials. Therefore a comparison between four different materials, namely Alq₃, α -NPD, TPBi and TCTA is drawn. The materials can be divided by their transport characteristics and by their sublimation characteristics. Alq₃ shows mainly electron transporting properties and does not melt before it sublimates under high vacuum conditions. The results for Alq₃ have already been discussed in section 6.3.4.1. Since very early reports on OLEDs, α -NPD or other diamine-derivatives were employed as hole transporting material [3].

⁴An average value of 72 nm was measured for the organic layer thickness on the target (measured with Dektak 8).

Table 6.4.: Fit parameters for multi Gaussian fit for different scanning speeds: target line width W_0 , target substrate distance l_d , Number N of Gaussian distributions, thickness of the organic layer on the target $l_{t,org}$, gas expansion factor ω_0 .

v_{scan} [m/s]	W_0 [μm]	l_d [μm]	N	$l_{t,org}$ [nm]	ω_0
1.0	61.0	0.96	100	80	27.1
1.25	57.3	0.96	100	74	27.1
1.5	53.6	0.96	100	75.5	26.0
1.75	50.9	0.96	100	78	26.6
2.0	48.2	0.96	100	78.5	25.5
2.5	43.9	0.96	100	77	26.0
3.0	40.2	0.96	100	77	25.5

When heated in high vacuum, α -NPD melts, before it evaporates. The mainly electron transporting material TPBi has -due to its wide band gap and low lying HOMO level- been employed as hole blocking material or host material for phosphorescent emitter molecules, for example Ir(ppy)₃. It also directly sublimes. Thin films of the carbazol-triamine TCTA exhibit a very high temperature stability and mainly hole transporting characteristics [113]. It is mainly used as a host material for a wide range of phosphorescent emitter materials [107, 182]. TCTA also evaporates, meaning that it has to melt before molecules overcome the surface bond energy.

It can be expected, that the transport properties do not affect any material's suitability for being micropatterned by the LILT process. Therefore the intermolecular bond energy of the surface molecules exercises the main influence on the sublimation characteristics. As two of the materials sublime from the solid and two other evaporate from the liquid, there may be a difference concerning the suitability or the physical description of the LILT process. Figure 6.16 shows experimental data sets for the different materials. Again, the target line width W_0 is determined as characteristic value in dependence of the scanning speed and the laser output power. The experimental data is depicted by open symbols, straight lines represent values fitted according to equation 6.13. The values of ΔT_{crit} for each fit and the mean values of D_0 are also indicated in figure 6.16. It shows, that for all sets of experimental data the mean beam diameter was determined to be about 45-47 μm , which is a good indicator for equal process conditions during the experiments. The values of the critical temperature difference ΔT_{crit} are very similar for Alq₃, α -NPD and TPBi and significantly lower than the values for TCTA. This resembles the situation, when the sublimation

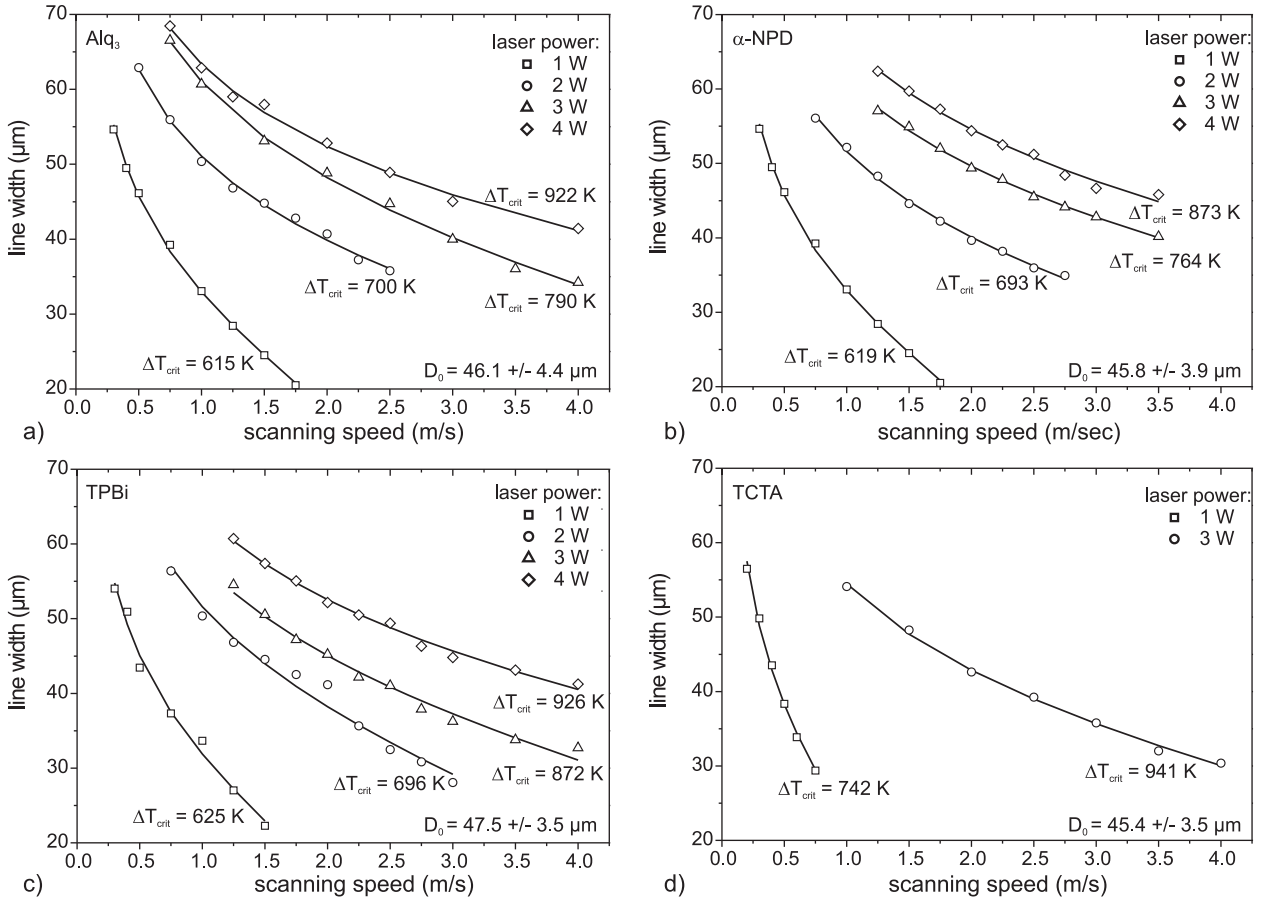


Figure 6.16.: Comparison of several organic materials micropatterned by the LILT process. Width of the patterned stripes on the target vs. scanning speed for various laser output powers (open symbols).

temperatures from quartz crucibles during OMBD processes are compared. Depending on the effusion cell design, Alq₃, α-NPD and TPBi exhibit very similar sublimation (respectively evaporation) temperatures in the range of 170 °C to 190 °C, whereas the evaporation temperature for TCTA is more than 240 °C, so that the general trend reflects the physical properties of the materials and the presented results once more validate the proposed model description (section 6.3.3).

6.3.4.3. reproducibility and homogeneity

For commercial applications of the LILT process, the reproducibility and homogeneity of the pattern is one of the key factors for the technology's acceptance. Using the described lab-

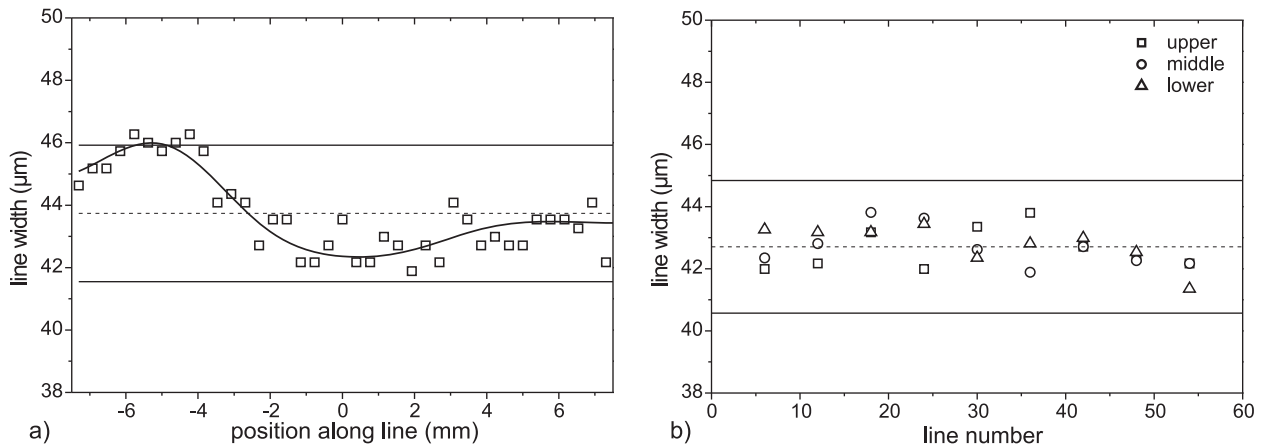


Figure 6.17.: Homogeneity and reproducibility of the LILT pattern: a) Line width measured on the target along a single line, which was 15 mm in total length. The dashed line represents the mean value of all measurements, the straight lines above and below mark $\pm 5\%$ of the mean value. The curved line shows a smoothed dataset and serves as guide to the eye. b) Line width of several lines measured on the target. The lines were aligned perpendicular to the scan direction of a single line. The dashed line represents the mean value of all measurements, the straight lines above and below mark $\pm 5\%$ of the mean value.

oratory setup, reproducibility and homogeneity tests were conducted on test patterns of 60 straight lines. Due to the maximum substrate size, which can be applied to the LILT setup in its current configuration, the pattern was limited to an area of about $20 \times 20 \text{ mm}^2$ ⁵. The laser power was set to 3 W the scanning speed accounted for 3 m/s. Figure 6.17.a plots the line width measured on the target along a single line of 15 mm length. Aside the mean value and $\pm 5\%$ bars a smoothed data set has been included as guide to the eye. Although a small oscillation of the line width can be observed, the smoothed data does not exceed the $\pm 5\%$ frame. It has already been noted, that the adjustment of the optical system was limited, so that even a small misalignment may cause a small but noticable deviation from the mean value. Compared to D_{min} , this is also reflected in the larger beam diameter determined in the previous sections. Under these aspects, the homogeneity along a single line is more than satisfying.

To check, if the line pattern reproduces well across the substrate, the line width of several stripes was measured at an upper, middle or lower position. The results are shown in figure 6.17b. Again, the dashed line represents the mean value, the straight lines indicate a deviation of $\pm 5\%$ from the mean value. The former is slightly smaller than the mean line

⁵The sample holder was designed to fit to a lab-wide standard substrate size of $35 \times 50 \text{ mm}^2$.

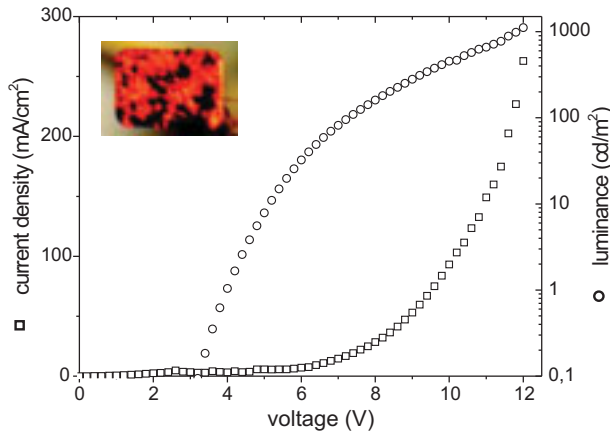


Figure 6.18.: Current density (squares) and luminance (circles) plotted against voltage for an OLED, partially deposited by LILT. The inset shows an image of the device after testing (degraded).

width measured along a single stripe, but under consideration of the observed line width oscillation very close within the given acceptance interval. Furthermore, the mean values indicated in figure 6.17 are very close to the value predicted by the model fit in figure 6.13. When the line widths across several lines are compared an even smaller deviation from the mean value is observed, indicating a superb reproducibility under the same process conditions. In conclusion, the homogeneity and reproducibility under identical process conditions are very satisfying for the projected substrate size.

6.3.4.4. OLED devices

As mentioned, the LILT process has been developed for patterning of organic light emitting diodes for full color display applications. Simple OLED devices were prepared to check the influence of the LILT process onto the devices characteristics. The structure of these devices can be derived from the inset of figure 6.19. Onto the cleaned ITO substrate, 40 nm of α -NPD were deposited as hole transporting layer by vacuum sublimation from quartz crucibles. The electron transporting and emitting layer consisted of DCM2 doped Alq_3 and was deposited by LILT. The target was sequentially coated with of 100 nm of Alq_3 and 10 nm of DCM2, meaning a target dopant concentration of 10 %. The intention was to demonstrate the intermixing of host and dopant, when being sublimed. For a homogeneous film deposition across the OLED area of $3 \times 4.5 \text{ mm}^2$, the target was scanned in several lines, which were positioned in a distance of $50 \mu\text{m}$ from each other. By this way, a relatively homogeneous deposition of the doped layer should be possible. Finally, the device was capped with a LiF/Al cathode.

The current density and luminance characteristics plotted against voltage are shown in

figure 6.18. At a driving voltage of 12 V a maximum luminance of 1200 cd/m² is measured. The luminance onset is observed at a voltage of 3.2 V. The current density which has to be applied for a luminance of 100 cd/m² was 18 mA/cm², resulting in a rather low current efficiency of 0.56 cd/A and power efficiency of 0.25 lm/W. As there was no chance to transfer the samples under vacuum conditions into the LILT process chamber, the vacuum chain was broken twice. Further, no clean room conditions were applied, so that a possible particle contamination led to defects and low efficiencies. The inset of figure 6.18 shows, that the device strongly degraded during the measurement. Under these conditions the efficiencies are within the expectance range. Further investigations on the influence of the LILT process are therefore not useful until closed vacuum processing can be guaranteed.

A higher emphasis should be placed onto the bias dependent electroluminescence spectra, shown in figure 6.19. It shows, that the emission spectra show a slight shift to smaller wavelengths for increasing driving voltage. The peak EL wavelength decreases from 660 nm for 6 V down to 650 nm for 12 V driving voltage. It is known that the emission spectrum of DCM2 depends on its concentration. For organic light emitting diodes, this has been described as solid state solvation effect [163]. The shift upon rising driving voltage shall be illustrated by figure 6.19b. When the driving voltage rises, injected holes penetrate deeper into electron transporting layer, shifting the recombination zone away from the NPD/Alq₃:DCM2 heterointerface. Under consideration of the solid state solvation effect this means, that the observed shift of the EL spectra with driving voltage originates from a graded doping con-

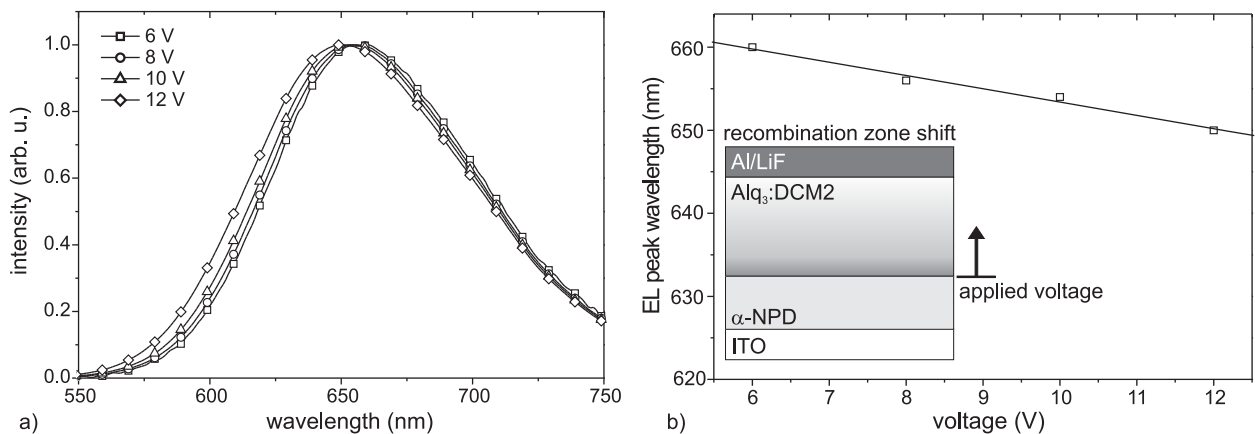


Figure 6.19.: Bias-induced shift of electroluminescence spectrum for an OLED deposited via LILT. a) Electroluminescence spectra for varying driving voltage. b) Shift of EL peak wavelength plotted against driving voltage. The inset shows a schematic of the in-situ doped OLED. An assumed doping concentration of DCM2 molecules is displayed in gray scales.

centration within the Alq₃:DCM2 layer [163]. Extrapolating the results of Forrest *et al.* a shift from 660 nm to 650 nm corresponds to a change in the doping concentration from 17 % to 9 %. The presented data suggests, that the diffusion does not lead to a perfect mixing of dopant and host molecules and the observed gradient reflects the position of the dopant on the target. This effect does not only mark a drawback but can also be employed as important feature for the deposition of graded emission layers. OLEDs with graded emission layers were reported to show higher efficiencies and lifetimes compared to conventional heterostructure devices [183, 184].

6.3.5. possibilities and limitations

In the previous sections, the laser induced local transfer has been described by a model description, which was validated by the presented experimental data. The LILT process is still subject to certain limitations, which have to be overcome, but offers advantages over established patterning technologies. Therefore, the limitations and possibilities of the laser induced local transfer shall be discussed.

resolution

The minimum feature size, which can be achieved on the substrate, is determined by the minimum line width on the target and by the gas expansion during the deposition. The smallest line width, which could be reproduced, was 20 μm . As mentioned in section 6.3.4.1 this can be reduced by employing a shorter laser wavelength, which would lead to a smaller minimum beam width D_{min} . As an example a frequency doubled Nd:YAG laser with an emission wavelength of 532 nm was given. The reduction of the laser wavelength also affects the minimum line width on the target. Therefore it seems reasonable, that the minimum feature size on the target can reach 10 μm or even slightly lower. This requires a very precise optical alignment of the components.

On the other hand, a very small line width on the target, does not instantly mean, that the minimum feature size on the substrate will be reduced in the same way. It was observed, that for very thin lines the thickness distribution on the substrate is close to a Gaussian distribution, which is far away from perfectly suited for AM OLED displays, where a flat steep-edged distribution is preferred. It is questionable whether the distribution changes, when the process is applied to AM OLED backplanes, on which the passivation layer forms a kind of a funnel for each pixel. If not, steeper edges can either be achieved by patterning

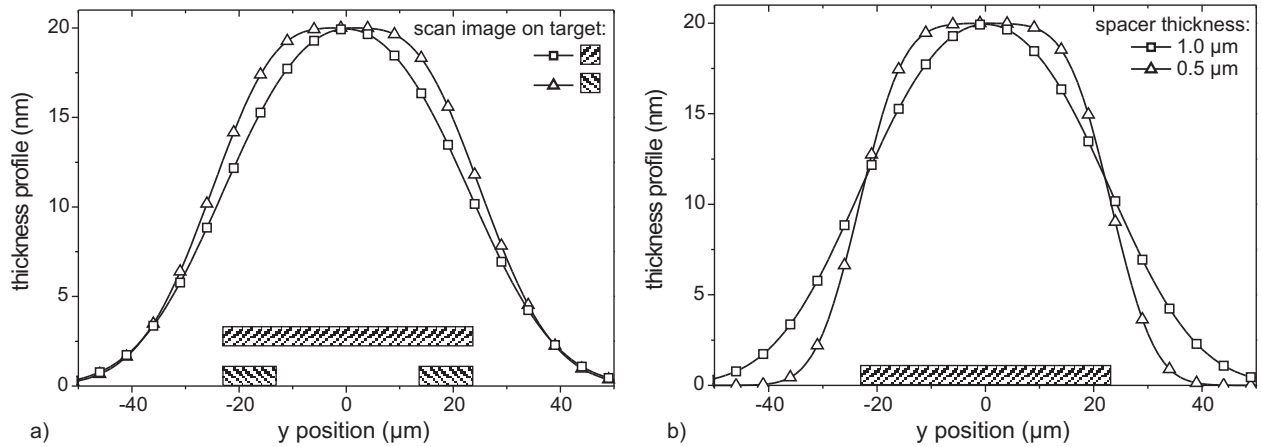


Figure 6.20.: Model calculations of the thickness distribution according to equation 6.19. a) Comparison between a single and a double line scan. The target source profile is indicated by hatched boxes. b) Comparison between different target substrate distances l_d .

two thin lines within a short distance of each other instead of one single broad line, or by reducing the target substrate distance. This is illustrated by model calculations, shown in figure 6.20. The calculations are based on the discussed multi Gaussian approach for the thickness distribution. A comparison between a single line scan (case I) and a double line scan (case II) is displayed in figure 6.20a. The width of the sublimated stripes on the target is indicated by hatched boxes, which are also shown within the diagram. For the calculations of the single line profile, the line width and thickness of the organic layer on target was assumed to be $46 \mu\text{m}$ respectively 21.6 nm . In the double line scan case, two lines were employed, for which a center to center distance of $26 \mu\text{m}$, a line width of $10 \mu\text{m}$ and a layer thickness of 55 nm were presumed. For both cases, the edge of the thickness distribution is not very steep. To avoid cross-contamination of neighboring subpixels, the center to center distance between these has to be at least $100 \mu\text{m}$. The double line scan profile shows a flat top from $\pm 10 \mu\text{m}$ from the center position, giving an advantage over the single line scan, as the useful width for each subpixel is higher. This has to be paid off with a lower material utilization, as the target can most likely not be recycled.

A better way to improve the deposition profile is to reduce the spacer thickness, if possible. Figure 6.20b shows a comparison of two deposition profiles calculated for different target to substrate distances. The line width ($46 \mu\text{m}$) as well as the layer thickness (20 nm) on the target was supposed to be equal for both cases. It shows, that the thickness distribution for a spacer thickness of $0.5 \mu\text{m}$ exhibits steeper edges, compared to the second profile, so that in this case the distance of neighboring subpixels can be decreased to $80 \mu\text{m}$. Furthermore, a

flat top within $\pm 10\ \mu$ from the center is observed, meaning a higher filling factor for thinner spacers. In contrast to the double line scan, this approach gives more advantages and no drawbacks. As the passivation layer of the AM OLED backplane may serve as spacing layer, a target to substrate distance of $0.5\ \mu\text{m}$ is possible.

doping profile

Although, the voltage dependent EL spectra did not allow to determine a depth resolved doping profile, two conclusions can be drawn from the presented data. First, doped emission layers were obtained from the intermixing of sequentially deposited layers during the LILT process. This so called in situ doping simplifies the target preparation process, as now the dopant concentration is determined by the thickness ratio of host and dopant layer. Second, the doping concentration is not constant throughout the emission layer, which may be a drawback or an advantage depending on the device architecture. If uniformly doped emission layers are desired, the position of the dopant layer has to be engineered. Another way of solving this task may be the deposition of several pairs of host and dopant layers, so that the concentration gradient becomes negligible.

working speed and substrate size

Commercial galvanometer scanners show typical maximum scanning speeds of 4-6 m/s. For a 19" XGA display (1024 x 768 pixels), an assumed scanning speed of 5 m/s during the LILT would result in a process time of about 60 s for each color. This does not include positioning and target handling. As in production tools, the substrate size is even bigger, the processing speed would not satisfy the throughput demand. Furthermore a galvanometer scanner based setup is limited by its maximum substrate size, as the working area is specified by the F-Theta lens and the minimum beam and pattern resolution scales with the working area. Therefore, a different configuration of the laser setup has to be pursued. Most promising will be parallelized processing by the employment of several parallel laser beams deflected by a line scanner or customized print heads with fiber-coupled laser diodes, which are already employed in the printing industry.

In conclusion, LILT shows the potential to allow high resolution patterning on large substrate sizes. Although the presented experimental configuration will not satisfy production demands, it serves well as research tool and allows to evaluate the critical process parameters, which can be employed for the development of LILT production tools. Furthermore as

it shows unique features like gradient doped emission layers, the setup can be used for other novel applications.

7. Conclusion

Organic light emitting diodes represent a promising technology for flat panel display applications for reasons of low weight, high brightness, large viewing angle and low power consumption. Despite the given advantages, market penetration on a large scale is yet to come, which is due to a lack of reliability and suitable large area mass production equipment for high-resolution full-color OLED displays. High resolutions can only be achieved by integrating current drivers onto the display substrate. In such an active-matrix driving scheme, top-emitting, or more specified, inverted organic light emitting diodes are preferred for enabling higher filling factors and the use of effective n-channel Si-TFTs. In the presented study, device concepts for highly efficient IOLEDs were investigated and novel, mass-production suitable deposition and patterning technologies were developed.

Two different ways of enhancing the device characteristics of IOLEDs were pursued. First the application of phosphorescent emitter materials was discussed. It was demonstrated, that quenching by sputter-induced recrystallization of the thermally instable host material CBP and non-radiative energy transfer to the metal cathode severely affects the efficiency of phosphorescent OLEDs. The mentioned quenching effects were minimized by using thermally stable host materials for the emission layer and an optimized thickness of the electron transporting layer. Applying these guidelines to IOLEDs with a common layer structure, but employing different phosphorescent emitter materials, yields high current efficiencies of 4.6 cd/A for red, 20.7 cd/A for green and 2.9 cd/A for blue light emission.

Further it was pointed out, that the non-radiative decay of interfacial exciplex states, which are present at the ETL/HTL interface during electrical excitation, leads to a decrease of the device efficiency. The formation of interfacial exciplex states can be avoided by dual-doping of the ETL and the HTL, resulting in an efficiency improvement of 80 %. In connection with doped charge injection layers, a green IOLED with superb efficiencies of 21 lm/W and 59 cd/A and a maximum brightness of more than 100000 cd/m² was realized. The complete AM brightness regime (<500 cd/m²) was covered by operating voltages below 10 V.

Stacking of several emission units in a single device was investigated as a further approach to enhance the current efficiency of IOLEDs. It was demonstrated, that in stacked OLEDs

doped pn-heterojunctions act as interconnecting units between two or more recombination and emission units. Further, it was shown, that both - the HTL and the ETL adjacent to the heterointerface - have to be doped for efficient charge generation. It was derived from low-temperature current voltage characteristics, that no explicit temperature dependence applies for the charge generation process. Further investigations by thickness-dependent current voltage characteristics and Kelvin Probe measurements indicated large band bending at the interface and the presence of a 5 nm wide depletion zone within the electron transport layer. An appropriate model for the charge generating mechanism was presented as direct tunneling from occupied HOMO states within the HTL to unoccupied LUMO states within the ETL. A stacked IOLED, which comprised of two emission units, revealed an excellent current efficiency of 92 cd/A at a brightness level of 600 cd/m². When compared to the initial values obtained for CBP-based IOLEDs, this value means an increase in current efficiency by more than two orders of magnitude. Stacking of (inverted) organic light emitting diodes is also expected to have a major impact on lighting applications. Concerning the lateral resistivity of the ITO anode and lifetime issues, a low current density is even more important for large lighting panels than it is for display applications.

A second part of the presented work focused on process technology. For transferring the IOLED preparation from a cluster-type system to an inline system, a new tool for room-temperature sputtering of ITO was designed and set up. The process development was conducted by specifying the influence of the oxygen content within the sputtering atmosphere and the plasma excitation mode (RF/DC) on the electrical and optical thin film properties. When adding oxygen to the sputtering gas a transition between a metallic and an oxide film was observed at moderate oxygen flow, which coincidences with highest conductivities and high transparency. The transition regime shifted to higher oxygen flows, when the RF power was decreased in favor of a higher DC power. For DC processes, the sputtering plasma is confined close to the target. In this case, the relative density of atomic oxygen species at the substrate's surface is significantly lower compared to RF sputtering. Therefore, a higher oxygen content in the sputtering atmosphere is needed for increasing DC power to incorporate the same amount of oxygen within the growing film. Optimization of the sputtering process led to a high conductivity of 2300 S/cm and a transparency of more than 85 %. These values completely fulfil and even exceed the initial target values.

In inline OMBD systems, a close distance between evaporation source and substrate is preferred for reasons of higher material usage. On the other hand, this reduces the overlap of the molecular beams of two different sources. Phosphor-doping of the emission layer has proven

to be very important for highly efficient IOLEDs. A new inline co-evaporation source was designed to allow deposition of two different materials perfectly aligned on a common axis. A prototype source was assembled and mounted into an inline test vessel to characterize the uniformity of deposition. It showed, that a uniformity of nearly $\pm 5\%$ was obtained on a substrate area of $100 \times 120 \text{ mm}^2$. Deviations exceeding the given limits, were attributed to dimensional and angular errors during machining of the source body. These results were confirmed by areal resolved PL measurements. For further effusion cells, replacable outlet holes, a balanced deposition profile and an improved cooling system for rapid cool-down are proposed.

Due to limited scalability, shadow masking as state-of-the-art micropatterning technique for small-molecule-based devices will not be suitable for future OLED mass production systems with substrate sizes larger than 1 m^2 . A novel approach of micropatterning organic thin films was presented by the laser induced local transfer (LILT). Again, a pilot setup was designed under the aspect of a future application within an inline OMBD system. During the LILT process, a so called target was positioned within a short distance to the OLED substrate. The target consisted of a float glass support, which was coated with an infrared absorbing layer (Ti) and the to be deposited organic material. The local heating of the absorption layer by scanning a focused laser beam along the bottom side of the target resulted in local sublimation of the organic material. The width of the sublimated stripe was described by the Gaussian heating profile induced by the laser and slightly broadened by heat diffusion. On the target, a reproducible minimum pattern size of about $20 \mu\text{m}$ was achieved. Due to the high local pressure during flashing the material to the substrate, the sublimated molecules rapidly expanded. This significantly broadened the width of the image pattern on the substrate with minimum feature sizes on the substrate of about $60 \mu\text{m}$. It showed, that the experimental data fits well to the derived model descriptions. The LILT process was successfully applied to several organic materials, which are commonly used as host or transport materials in OLEDs. The presented results allows to conclude, that the LILT process shows the potential to enable high resolution patterning for full-color AM-OLED displays on large substrate sizes.

In the near future, the developed deposition and patterning technology will be merged within a second generation inline OMBD tool, which will feature several linear co-evaporation sources, a linear magnetron cathode for RT-sputtering of ITO, a LILT module, a magnetically levitated linear drive for uniform movement of the substrates and loading and unloading stages at both ends of the system, which allows a continuous feed of substrates and process-

ing under conditions close to production. When completed, the system will be the first inline OMBD system strictly dedicated to research on the fabrication of high-resolution full-color OLED displays.

A. molecular structures

Organic materials employed for this work are mentioned by their commonly cited abbreviations throughout the thesis. The following survey gives the correct chemical formulae and displays the corresponding molecular structures.

1-TNATA	: 4,4',4''-Tris(<i>N</i> -(1-naphthyl)- <i>N</i> -phenylamino)triphenylamine
α -NPD	: <i>N,N'</i> -Di-(1-naphthyl)- <i>N,N'</i> -diphenylbenzidine
Alq ₃	: Tris(8-quinolato)aluminium
BPhen	: 4,7-Diphenyl-1,10-phenantroline
btp ₂ Ir(acac)	: Bis(2-(2'-pyridyl)benzo[<i>b</i>]thiophenato- <i>N,C</i> ⁸)iridium(III)acetylacetonate
CBP	: <i>N,N'</i> -Dicarbazolyl-4,4'-biphenyl
DCM II	: 4-(Dicyanomethylene)-2-methyl-6-(julolidin-4yl-vinyl)-4 <i>H</i> -pyran
F ₄ -TCNQ	: 2,3,5,6-Tetrafluoro-7,7,8,8-tetracyanoquinodimethane
FIrpic	: Bis((4,6-difluorophenyl)2-pyridinato- <i>N,C</i> ²)iridium(III)picolate
Ir(ppy) ₃	: Tris(2-phenylpyridin)iridium(III)
PEDOT	: Poly(3,4-ethylenedioxy)thiophene
PSS	: Poly(styrenesulfonate)
TAPC	: 1,1-Bis(di-4-tolylaminophenyl)cyclohexane
TCTA	: 4,4',4''-Tris(<i>N</i> -carbazolyl)triphenylamine
TPBI	: 1,3,5-Tris(phenyl-2-benzimidazole)benzene

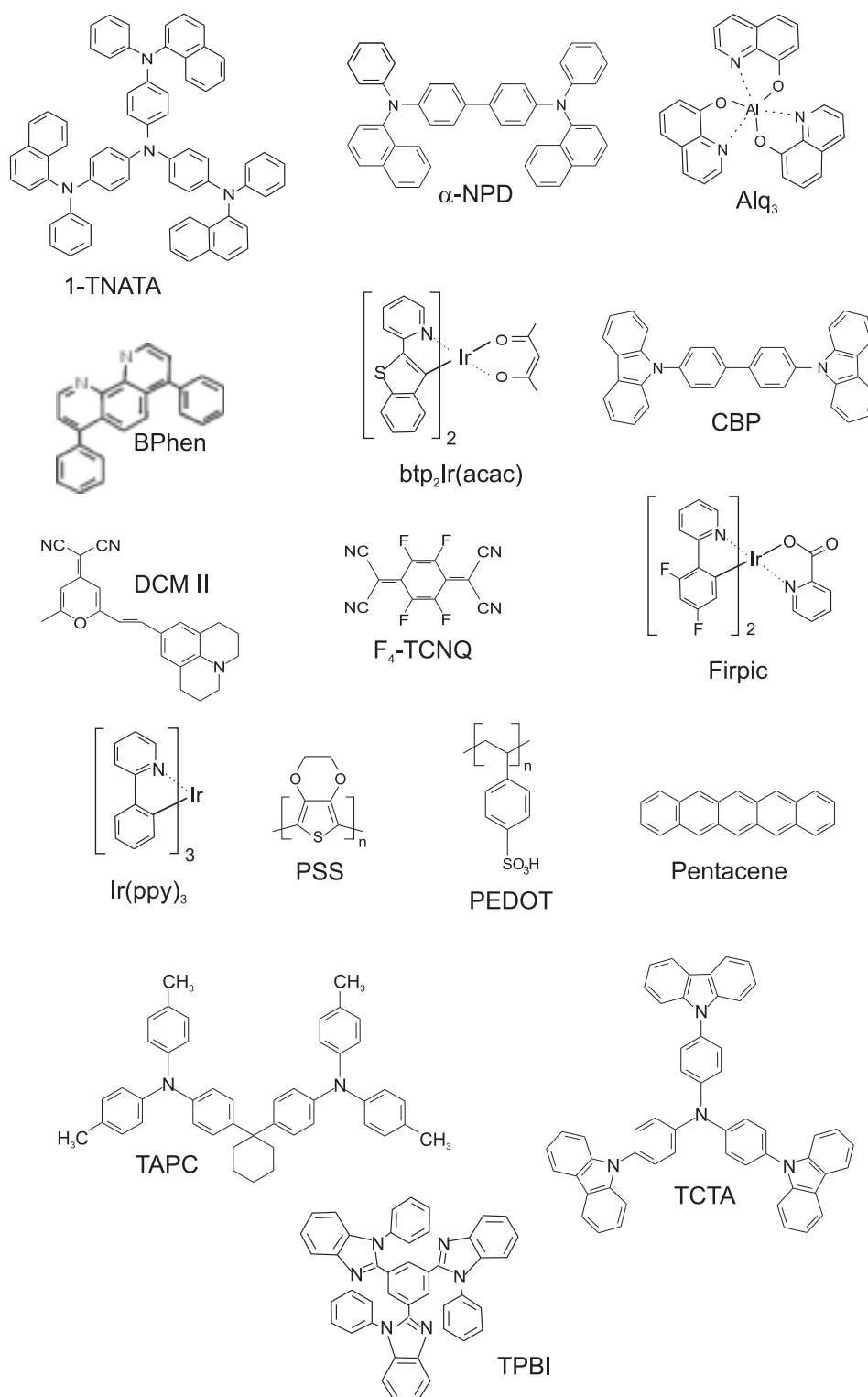


Figure A.1.: Molecular structures of the organic materials used for this work.

Bibliography

- [1] J. N. Bardsley: *International oled technology roadmap*. IEEE J. Sel. Top Quant. Elec. **10** (2004), 3.
- [2] J. R. Brodrick, C. E. Christy: *Accelerating the development of next-generation solid-state lighting sources*. Proc. of SPIE **5530** (2004), 1.
- [3] C. W. Tang, S. A. VanSlyke: *Organic electroluminescent diodes*. Appl. Phys. Lett. **51** (1987), 913.
- [4] J. H. Burroughes, D. D. C. Bradley, A. R. Brown, R. N. Marks, K. MacKay, R. H. Friend, P. L. Burn, A. B. Holmes: *Light-emitting diodes based on conjugated polymers*. Nature **347** (1990), 799.
- [5] W. Helfrich, W. G. Schneider: *Recombination radiation in anthracene crystals*. Phys. Rev. Lett. **14** (1965), 229.
- [6] D. Tanaka, H. Sasabe, Y.-J. Li, S.-J. Su, T. Takeda, J. Kido: *Ultra high efficiency green organic light-emitting devices*. Jpn. J. Appl. Phys. **46** (2007), L10.
- [7] T. Dobbertin, E. Becker, T. Benstem, G. Ginev, D. Heithecker, H.-H. Johannes, D. Metzdorf, H. Neuner, R. Parashkov, W. Kowalsky: *Oled matrix displays: in-line process technology and fundamentals*. Thin Solid Films **442** (2003), 132.
- [8] D. Metzdorf: *Organische Passiv-Matrix Displays*. Göttingen: Cuvillier 2003.
- [9] D. Pribat, F. Plais: *Matrix addressing for organic electroluminescent displays*. Thin Solid Films **383** (2001), 25.
- [10] J. C. Strum, F. Pschenitzka, T. R. Hebner, M. H. Lu, C. C. Wu, W. Wilson: *Patterning approaches and system power efficiency considerations for organic led displays*. Proc. of SPIE **3476** (1998), 208.
- [11] D. L. Mathine, H. S. Woo, W. He, T. W. Kim, B. Kippelen, N. Peyghambarian: *Heterogeneously integrated organic light-emitting diodes with complementary metal-oxide-silicon circuitry*. Appl. Phys. Lett. **76** (2000), 3849.
- [12] Y.-J. Tung, R. Hewitt, A. Chwang, M. Hack, J. Brown, K.-M. Kim, D. S. Kim, J. H. Hur, J. Jang: *A 200-dpi transparent a-si tft active-matrix phosphorescent oled display*. SID 05 Digest, 2005, 1546.

-
- [13] N. Frühauf: *Active matrix drive circuit*. Patent US 2004/0100430 A1, United States Patent and Trademark Office, 2004.
 - [14] M. Köger, E. Becker, C. Schildknecht, S. Hartmann, H.-H. Johannes, W. Kowalsky: *Monolithic integration of ofets driving organic light emitting diodes*. Proc. of SPIE **5940** (2005), 59401I.
 - [15] E. Becker: *Technologien für organische Feldeffekttransistoren in der Displaytechnik*. Göttingen: Cuvillier 2006.
 - [16] M. Kitamura, T. Imada, Y. Arakawa: *Organic light-emitting diodes driven by pentacene-based thin-film transistors*. Appl. Phys. Lett. **83** (2003), 3410.
 - [17] M. S. P. Görrn, J. Meyer, M. Kröger, E. Becker, H.-H. Johannes, W. Kowalsky, T. Riedl: *Towards see-through displays: Fully transparent thin-film transistors driving transparent organic light-emitting diodes*. Adv. Mater. **18** (2006), 738.
 - [18] G. Gu, V. Bulovic, P. E. Burrows, S. R. Forrest: *Transparent organic light emitting devices*. Appl. Phys. Lett. **68** (1996), 2606.
 - [19] G. Parthasarathy, P. E. Burrows, V. Khalfin, V. G. Kozlov, S. R. Forrest: *A metal-free cathode for organic semiconductor devices*. Appl. Phys. Lett. **72** (1998), 2138.
 - [20] G. Parthasarathy, C. Adachi, P. E. Burrows, S. R. Forrest: *High-efficiency transparent organic light-emitting devices*. Appl. Phys. Lett. **76** (2000), 2128.
 - [21] P. E. Burroes, G. Gu, S. R. Forrest, E. P. Vicenzi, T. X. Zhou: *Semitransparent cathodes for organic light emitting devices*. J. Appl. Phys. **87** (2000), 3080.
 - [22] L. S. Hung, C. W. Tang, M. G. Mason, P. Raychaudhuri, J. Madathil: *Application of an ultrathin lif/al bilayer in organic surface-emitting diodes*. Appl. Phys. Lett. **78** (2001), 544.
 - [23] V. Bulovic, P. Tian, P. E. Burrows, M. R. Gokhale, S. R. Forrest, M. E. Thompson: *A surface-emitting vacuum-deposited organic light emitting device*. Appl. Phys. Lett. **70** (1997), 2954.
 - [24] T. Dobbertin, M. Kroeger, D. Heithecker, D. Schneider, D. Metzendorf, H. Neuner, E. Becker, H.-H. Johannes, W. Kowalsky: *Inverted top-emitting organic light-emitting diodes using sputter-deposited anodes*. Appl. Phys. Lett. **82** (2003), 284.
 - [25] T. Dobbertin: *Invertierte organische Leuchtdioden für Aktiv-Matrix OLED-Anzeigen*. Göttingen: Cuvillier Verlag 2005.
 - [26] T. Dobbertin, O. Werner, J. Meyer, A. Kammoun, D. Schneider, T. Riedl, E. Becker, H.-H. Johannes, W. Kowalsky: *Inverted hybrid organic light-emitting device with*

- polyethylene dioxythiophene-polystyrene sulfonate as an anode buffer layer*. Appl. Phys. Lett. **83** (2003), 5071.
- [27] S. Hartmann: n.n. Dissertation, Fakultät für Elektrotechnik und Informationstechnik, Technische Universität Braunschweig, 2007.
- [28] S. Hartmann, A. Janssen, H.-H. Johannes, R. Caspary, W. Kowalsky, H. Schwab, D. Bertram, H. Blei, N. Meyer, B. Marheineke, M. Heuken: *Stable deposition of organic materials for ir-based red oleds using organic vapor phase deposition*. SID Digest, 2006, 1563.
- [29] U. Hoffmann, M. Bender, M. Campo, E. Sommer: *Vertical inline deposition technology for full-color oled production*. SID 05 Digest, 2005, 1204.
- [30] A. Heeger: *Semiconducting and metallic polymers: the fourth generation of polymeric materials*. Nobel Lecture, Stockholm, Sweden, 2000, 380–417.
- [31] N. Karl, K. K.-H, J. Marktanner, M. Münch, F. Schatz, R. Stehle, H.-M. Uhde: *Fast electronic transport in organic molecular solids*. J. Vac. Sci. Technol. A **17** (1999), 2318.
- [32] E. A. Slinish: *Organic Molecular Crystals - Their Electronic States*. Heidelberg: Springer 1980.
- [33] H. Ishii, K. Sugiyama, E. Ito, K. Seki: *Energy level alignment and interfacial electronic structures at organic/metal and organic/organic interfaces*. Adv. Mater. **11** (1999), 608.
- [34] J. Schöbel: *UV-Photoelektronenspektroskopie zur Untersuchung von Schichtgrenzen und Kontakten in organischen Leuchtdioden*. Cuvillier 2000.
- [35] I. Hill, A. Kahn, Z. Soos, , R. Pascal: *Charge-separation energy in films of pi-conjugated organic molecules*. Chem. Phys. Lett. **327** (2000), 181.
- [36] C. Wu, Y. Hirose, H. Sirringhaus, A. Kahn: *Electron-hole interaction energy in the organic molecular semiconductor ptcda*. Chem. Phys. Lett. **272** (1997), 43.
- [37] E. Lebedev, T. Dittrich, V. Petrova-Koch, S. Karg, W. Brütting: *Charge carrier mobility in poly(p-phenylenevinylene studied by the time-of-flight technique*. Appl. Phys. Lett. **71** (1997a), 2686.
- [38] H. Bässler, G. Schönherr, M. Abkowitz, D. M. Pai: *Hopping transport in prototypical organic glasses*. Phys. Rev. B **26** (1982), 3105.
- [39] W. D. Gill: *Drift mobilities in amorphous charge-transfer complexes of trinitrofluorenone and poly-n-vinylcarbazole*. J. Appl. Phys. **43** (1972), 5033.

-
- [40] P. N. Murgatroyd: *Theory of space-charge-limited current enhanced by frenkel effect*. J. Phys. D: Appl. Phys. **3** (1970), 151.
- [41] C. D. Dimitriakopoulos, P. R. L. Malenfant: *Prganic thin film transistors for large area electronics*. Adv. Mater. **14** (2002), 99.
- [42] C. Hosokawa, H. Tokailin, H. Higashi, T. Kusumoto: *Transient behaviour of organic thin film electroluminescence*. Appl. Phys. Lett. **60** (1992), 1220.
- [43] P. E. Burrows, Z. Shen, V. Bulovic, D. M. McCarty, S. R. Forrest, J. A. Cronin, M. E. Thompson: *Relationship between electroluminescence and current transport in organic heterojunction light-emitting devices*. J. Appl. Phys. **79** (1996), 7991.
- [44] P. E. Burrows, S. R. Forrest: *Electroluminescence from trap-limited current transport in vacuum deposited organic light emitting devices*. Appl. Phys. Lett. **64** (1994), 2285.
- [45] M. Pope, C. E. Swenberg: *Electronic Processes in Organic Crystals*. Oxford: Clarendon Press 1982.
- [46] K. C. Kao, W. Hwang: *Electrical Transports in Solids*, volume 14. Oxford, New York, Toronto, 1981: Pergamon Press 1981.
- [47] W. Gao, A. Kahn: *Electronic structure and current injection in zinc phtalocyanine doped with tetrafluoro-cyanoquinodimethane: Interface vs. bulk effects*. Org. Elect. **3** (2002), 53.
- [48] V. I. Arkhipov, H. von Seggern, E. V. Emelianova: *Charge injection versus space-charge-limited current in organic light-emitting diodes*. Appl. Phys. Lett. **83** (2003), 5074.
- [49] C. Chan, W. Gao, A. Kahn: *Contact potential difference measurements of doped organic molecular thin films*. J. Vac. Sci. Technol. A **22** (2004), 1488.
- [50] I. G. Hill, A. Rajagopal, A. Kahn, Y. Hu: *Molecular level alignment at organic semiconductor-metal interfaces*. Appl. Phys. Lett. **73** (1998), 662.
- [51] S. T. Lee, X. Y. Hou, M. G. Mason, C. W. Tang: *Energy level alignment at alq/metal interfaces*. Appl. Phys. Lett. **72** (1998), 1593.
- [52] Y. Park, V.-E. Choong, B. Hsieh, C. W. Tang, T. Wehrmeister, K. Müllen, Y. Gao: *Electron spectroscopy studies of interface formation between metal electrodes and luminescent organic materials*. J. Vac. Sci Technol. A **15** (1997), 2574.
- [53] Q. Xu, J. Ouyang, Y. Yang, T. Ito, J. Kido: *Ultrahigh efficiency green polymer light-emitting diodes by nanoscale interface modification*. Appl. Phys. Lett. **83** (2003), 4695.

-
- [54] H. Heil, J. Steiger, S. Karg, M. Gastel, H. Ortner, H. von Seggern, M. S. el: *Mechanisms of injection enhancement in organic light-emitting diodes through an al/lif electrode*. J. Appl. Phys. **89** (2001), 420.
- [55] B. N. Limketkai, M. A. Baldo: *Charge injection into cathode-doped amorphous organic semiconductors*. Phys. Rev. B **71** (2005), 085207.
- [56] C. Shen, A. Kahn, J. Schwartz: *Chemical and electrical properties of interfaces between magnesium and aluminum and tris-(8-hydroxy quinoline) aluminum*. J. Appl. Phys. **89** (2001), 449.
- [57] S. Kera, Y. Yabuuchi, H. Yamane, H. Setoyama, K. K. Okudaira, A. Kahn, N. Ueno: *Impact of an interface dipole layer on molecular level alignment at an organic-conductor interface studied by ultraviolet photoemission spectroscopy*. Phys. Rev. B **70** (2004), 085304.
- [58] X. L. Zhu, J. X. Sun, X. M. Yu, M. Wong, H. S. Kwok: *Very bright and efficient top-emitting oled with ultra-thin yb as effective electron injector*. SID 2006 Digest (2006), 1292.
- [59] M. G. Mason, L. S. Hung, C. W. Tang, S. T. Lee, K. W. Wong, M. Wang: *Characterisation of treated indium-tin-oxide surfaces used in electroluminescent devices*. J. Appl. Phys. **86** (1998), 1688.
- [60] S. W. Tong, C. S. Lee, Y. Lifshitz, D. Q. Gao, S. T. Lee: *Conducting fluorocarbon coatings for organic light-emitting diodes*. Appl. Phys. Lett. **84** (2004), 4032.
- [61] C. O. Poon, F. L. Wong, S. W. Tong, R. Q. Zhang, C. S. Lee, S. T. Lee: *Improved performance and stability of organic light-emitting devices with silicon oxy-nitride buffer layer*. Appl. Phys. Lett. **83** (2003), 1038.
- [62] C. Ganzori, K.-J. Kwak, K. Yagi, M. Fujihara: *Fine tuning work function of indium tin oxide by surface molecular design: Enhanced hole injection in organic electroluminescent devices*. Appl. Phys. Lett. **79** (2001), 272.
- [63] L. S. Hung, C. W. Tang, M. G. Mason: *Enhanced electron injection in organic electroluminescence devices using an al/lif electrode*. Appl. Phys. Lett. **70** (1997), 152.
- [64] J. Lee, Y. Park, D. Y. Kim, H. Y. Chu, H. Lee, L.-M. Do: *High efficiency organic light-emitting devices with al/naf cathode*. Appl. Phys. Lett. **82** (2003), 173.
- [65] X. J. Wang, J. M. Thao, Y. C. Zhou, X. Z. Wang, S. T. Zhang, Y. Q. Zhan, T. Xu, H. J. Ding, G. Y. Zhong, H. Z. Shi, Z. H. Xiong, Y. Liu, Z. J. Wang, E. G. Obbard, X. M. Ding, W. Huang, X. Y. Hou: *Enhancement of electron injection in organic light-emitting devices using an ag/lif cathode*. J. Appl. Phys. **95** (2004), 3828.

-
- [66] T. Mori, M. Suzuki, S. Tokito, Y. Taga: *Changes in electronic structure of 8-hydroxyquinoline aluminum/al interface by insertion of thin electron injection layers*. Proc. of SPIE **3797** (1999), 367.
- [67] H. Neuner: Untersuchungen zum Ladungsträgertransport in organischen Halbleiterbauelementen. Dissertation, Fakultät für Maschinenbau und Elektrotechnik, Technische Universität Braunschweig, 2002.
- [68] C.-W. Chen, C.-L. Lin, C.-C. Wu: *An effective cathode structure for inverted top-emitting organic light-emitting devices*. Appl. Phys. Lett. **85** (2004), 2469.
- [69] S. Y. Kim, J.-L. Lee, K.-B. Kim, Y.-H. Tak: *Effect of ultraviolet-ozone treatment of indium-tin-oxide on electrical properties of organic light emitting diodes*. J. Appl. Phys. **95** (2004), 2560.
- [70] K. Sugiyama, H. Ishii, Y. Ouchi, K. Seki: *Dependence of indium-tin-oxide work function on surface cleaning method as studied by ultraviolet and x-ray photoemission spectroscopies*. J. Appl. Phys. **87** (2000), 295.
- [71] H. Y. Yu, X. D. Feng, D. Grozea, Z. H. Lu, R. N. S. Sodhi, A.-M. Hor, H. Aziz: *Surface electronic structure of plasma-treated indium tin oxides*. Appl. Phys. Lett. **78** (2001), 2595.
- [72] X. M. Ding, L. M. Hung, L. F. Cheng, Z. B. Deng, X. Y. Hou, C. S. Lee, S. T. Lee: *Modification of the hole injection barrier in organic light-emitting devices studied by ultraviolet photoelectron spectroscopy*. Appl. Phys. Lett. **76** (2000a), 2704.
- [73] D. J. Milliron, I. G. Hill, C. Shen, A. Kahn, J. Schwartz: *Surface oxidation activates indium tin oxide for hole injection*. J. Appl. Phys. **87** (2000), 572.
- [74] N. Koch, A. Elschner, J. Schwartz, A. Kahn: *Organic molecular films on gold versus conducting polymer: Influence of injection barrier height and morphology on current-voltage characteristics*. Appl. Phys. Lett. **82** (2003), 2281.
- [75] N. Koch, A. Kahn, J. Ghijsen, J.-J. Pireaux, J. Schwartz, R. L. Johnson, A. Elschner: *Conjugated organic molecules on metal versus polymer electrodes: Demonstration of a key energy level alignment mechanism*. Appl. Phys. Lett. **82** (2003), 70.
- [76] T. Minakata, I. Nagoya, M. Ozaki: *Highly ordered and conducting thin film of pentacene doped with iodine vapor*. J. Appl. Phys. **69** (1991), 7354.
- [77] J. Endo, T. Matsumoto, J. Kido: *Organic electroluminescent devices with a vacuum-deposited lewis-acid-doped hole-injecting layer*. Jpn. J. Appl. Phys. **41** (2002), 358.

- [78] C. Ganzorig, M. Fujihara: *Improved drive voltages of organic electroluminescent devices with an efficient p-type aromatic diamine hole-injection layer*. Appl. Phys. Lett. **77** (2000a), 4211.
- [79] A. Yamamori, C. Adachi, T. Koyama, Y. Taniguchi: *Doped organic light emitting diodes having a 650-nm-thick hole transport layer*. Appl. Phys. Lett. **72** (1998), 2147.
- [80] J. Blochwitz, M. Pfeiffer, T. Fritz, K. Leo: *Low voltage organic light emitting diodes featuring doped phthalocyanine as hole transport material*. Appl. Phys. Lett. **73** (1998), 729.
- [81] X. Zhou, M. Pfeiffer, J. Blochwitz, A. Werner, A. Nollau, T. Fritz, K. Leo: *Very-low-operating-voltage organic light-emitting diodes using a p-doped amorphous hole injection layer*. Appl. Phys. Lett. **78** (2001), 410.
- [82] W. Gao, A. Kahn: *Controlled p doping of the hole-transport molecular material n,n'-diphenyl-n,n'-bis(1-naphthyl)-1,1'-biphenyl-4,4'-diamine with tetrafluorotetracyanoquinodimethane*. J. Appl. Phys. **94** (2003), 359.
- [83] W. Gao, A. Kahn: *Controlled p-doping of zinc phthalocyanine by coevaporation with tetrafluorotetra-cyanoquinodimethane: A direct and inverse photoemission study*. Appl. Phys. Lett. **79** (2001), 4040.
- [84] T. Minakata, M. Ozaki, H. Imai: *Conducting thin films of pentacene doped with alkaline metals*. J. Appl. Phys. **74** (1993), 1079.
- [85] J. Kido, T. Matsumoto: *Bright organic electroluminescent devices having a metal-doped electron-injecting layer*. Appl. Phys. Lett. **73** (1998), 2866.
- [86] G. Parthasarathy, C. Shen, A. Kahn, S. R. Forrest: *Lithium doping of semiconducting organic charge transport materials*. J. Appl. Phys. **89** (2001), 4986.
- [87] A. Nollau, M. Pfeiffer, T. Fritz, K. Leo: *Controlled n-type doping of a molecular organic semiconductor: Naphtalenetetracarboxylic dianhydride (ntcda) doped with bis(ethylenedithio)-tetrathiafulvalene (bedt-ttf)*. J. Appl. Phys. **2000** (2000), 4340.
- [88] A. G. Werner, F. Li, K. Harada, T. Fritz, K. Leo: *Pyronin b as donor for n-type doping of organic thin films*. Appl. Phys. Lett. **82** (2003), 4495.
- [89] C. K. Chan, E.-G. Kim, J.-L. Bredas, A. Kahn: *Molecular n-type doping of 1,4,5,8-naphthalene tetracarboxylic dianhydride by pyronin b studied using direct and inverse photoelectron spectroscopies*. Adv. Func. Mater. **2006** (2006), 831.
- [90] A. Werner: N-type doping of organic thin films using a novel class of dopants. Dis-

-
- sertation, Fakultät für Mathematik und Naturwissenschaften, Technische Universität Dresden, 2003.
- [91] A. Böhler: *Organische Elektrolumineszenzdisplays*. Aachen: Shaker Verlag 1999.
 - [92] J. Huang, M. Pfeiffer, A. Werner, J. Blochwitz, K. Leo, S. Liu: *Low-voltage organic electroluminescent devices using pin structures*. Appl. Phys. Lett. **80** (2002), 139.
 - [93] X. Zhou, J. Blochwitz, M. Pfeiffer, A. Nollau, T. Fritz, K. Leo: *Enhanced hole injection into amorphous hole-transport layers of organic light-emitting diodes using controlled p-type doping*. Adv. Funct. Mater. **11** (2001), 310.
 - [94] M.-T. Hsieh, C.-C. Chang, J.-F. Chen, C. H. Chen: *Study of hole concentration of 1,4-bis[N-(1-naphthyl)-N'-phenylamino]-4,4'-diamine doped with tungsten oxide by admittance spectroscopy*. Appl. Phys. Lett. **89** (2006), 103510.
 - [95] C.-W. Chen, Y.-J. Lu, C.-C. Wu, E. H.-E. Wu, C.-W. Chu, Y. Yang: *Effective connecting architecture for tandem organic light-emitting devices*. Appl. Phys. Lett. **87** (2005), 241121.
 - [96] C.-I. Wu, C.-T. Lin, Y.-H. Chen, M.-H. Chen, Y.-J. Lu, C.-C. Wu: *Electronic structures and electron-injection mechanisms of cesium-carbonate-incorporated cathode structures for organic light-emitting devices*. Appl. Phys. Lett. **88** (2006), 152104.
 - [97] J. Kalinowski: *Organic Light-Emitting Diodes*. New York: Marcel Dekker 2005.
 - [98] M. Baldo: *The electronic and optical properties of amorphous organic semiconductors*. Dissertation, Department of Electrical Engineering, Princeton University, 2001.
 - [99] N. C. Greenham, R. H. Friend, D. D. C. Bradley: *Angular dependence of the emission from a conjugated polymer light-emitting diode: Implications for efficiency calculations*. Adv. Mater. **6** (1994), 491.
 - [100] M.-H. Lu, M. S. Weaver, T. X. Zhou, M. Rothman, R. C. Kwong, M. Hack, J. J. Brown: *High-efficiency top-emitting organic light-emitting devices*. Appl. Phys. Lett. **81** (2002), 3921.
 - [101] M. A. Baldo, D. F. O'Brien, Y. You, A. Shoustikov, S. Sibley, M. E. Thompson, S. R. Forrest: *Highly efficient organic light-emitting devices based on electrophosphorescence*. Nature **395** (1998), 151.
 - [102] M. A. Baldo, S. Lamansky, P. E. Burrows, M. E. Thompson, S. R. Forrest: *Very high-efficiency green organic light-emitting devices based on electrophosphorescence*. Appl. Phys. Lett. **75** (1999), 4.

- [103] T. Tsutsui, M.-J. Yang, M. Yahiro, K. Nakamura, T. Watanabe, T. Tsuji, T. Wakimoto, S. Miyaguchi: *High quantum efficiency in organic light-emitting devices with iridium-complex as a triplet emissive center*. Jpn. J. Appl. Phys. **38** (1999), 1502.
- [104] M. Ikai, S. Tokito, Y. Sakamoto, T. Suzuki, Y. Taga: *Highly efficient phosphorescence from organic light-emitting devices with an exciton-block layer*. Appl. Phys. Lett. **79** (2001), 156.
- [105] C. Adachi, M. A. Baldo, M. E. Thompson, S. R. Forrest: *Nearly 100 % internal phosphorescence efficiency in an organic light emitting device*. J. Appl. Phys. **90** (2001), 5048.
- [106] C. Adachi, M. A. Baldo, S. R. Forrest: *High-efficiency red electrophosphorescence devices*. Appl. Phys. Lett. **78** (2001), 1622.
- [107] S.-C. Lo, N. A. H. Male, J. P. J. Markham, S. W. Magennis, P. L. Burn, O. V. Salata, I. D. W. Samuel: *Green phosphorescent dendrimer for light-emitting diodes*. Adv. Mater. **14** (2002), 975.
- [108] I. G. Hill, A. Kahn: *Energy level alignment at interfaces of organic semiconductor heterostructures*. J. Appl. Phys. **84** (1998), 5583.
- [109] M. A. Baldo, S. R. Forrest: *Transient analysis of organic electrophosphorescence. i. transient analysis of triplet energy transfer*. Phys. Rev. B **62** (2000), 10958.
- [110] H. Kuma, H. Tokairin, K. Fukuoka, C. Hosokawa: *Optical simulation of oled devices and its application for determination of emitting zone*. SID 2005 digest, 2005, 1276.
- [111] M. E. Thompson, S. Lamansky, P. Djurovich, D. Murphy, F. Abdel-Razzaq, S. R. Forrest, M. Baldo, P. E. Burrows, C. Adachi, T. X. Zhou, L. Michalski, J. J. Brown: *High efficiency organic electrophosphorescent devices*. Proc. of SPIE **4105** (2001), 119.
- [112] G. Gu, G. Parthasarathy, P. E. Burrows, P. Tian, I. G. Hill, A. Kahn, S. R. Forrest: *Transparent stacked organic light emitting devices. i. design principles and transparent compound electrodes*. J. Appl. Phys. **86** (1999), 4067.
- [113] Y. Kuwabara, H. Ogawa, H. Inada, N. Noma, Y. Shirota: *Thermally stable multilayered organic electroluminescent devices using novel starburst molecules, 4,4',4''-tri(n-carbazolyl)triphenylamine (tcta) and 4,4',4''-tris(3-methylphenylphenyl-amino)triphenylamine (m-mtda), as hole-transport materials*. Adv. Mater. **6** (1994), 677.
- [114] P. R. Chance, A. Prock, R. Silbey: *Advances in Chemical Physics*, 1. New York: John Wiley & Sons, Inc., 1978.

-
- [115] K. Kuhnke, R. Becker, M. Epple, K. Kern: *C₆₀ exciton quenching near metal surfaces*. Phys. Rev. Lett. **79** (1997), 3246.
- [116] D. F. O'Brian, M. A. Baldo, M. E. Thompson, S. R. Forrest: *Improved energy transfer in electrophosphorescent devices*. Appl. Phys. Lett. **74** (1999), 442.
- [117] C. Adachi, R. C. Kwong, P. Djurovich, V. Adamovich, M. A. Baldo, M. E. Thompson, S. R. Forrest: *Endothermic energy transfer: A mechanism for generating very efficient high-energy phosphorescent emission in organic materials*. Appl. Phys. Lett. **79** (2001), 2082.
- [118] R. J. Holmes, S. R. Forrest, Y.-J. Tung, R. C. Kwong, J. J. Brown, S. Garon, M. E. Thompson: *Blue organic electrophosphorescence using exothermic host-guest energy transfer*. Appl. Phys. Lett. **82** (2003), 2422.
- [119] S. Tokito, T. Iijama, Y. Suzuri, H. Kita, T. Tsuzuki, F. Sato: *Confinement of triplet energy on phosphorescent molecules for highly-efficient organic blue-light-emitting devices*. Appl. Phys. Lett. **83** (2003), 569.
- [120] C. Adachi, R. Kwong, S. R. Forrest: *Efficient electrophosphorescence using a doped ambipolar conductive molecular organic thin film*. Org. Elec. **2** (2001), 37.
- [121] N. Matsuse, S. Ikame, Y. Suzuki, H. Naito: *Charge-carrier transport and triplet exciton diffusion in a blue electrophosphorescent emitting layer*. J. Appl. Phys. **97** (2005), 123512.
- [122] N. Matsuse, Y. Suzuki, H. Naito: *Charge carrier transport in neat thin films of phosphorescent iridium complexes*. Jpn. J. Appl. Phys. **44** (2005), 3691.
- [123] P. E. Burrows, A. B. Padmaperuma, L. S. Sapochak, P. Djurovich, M. E. Thompson: *Ultraviolet electroluminescence and blue-green phosphorescence using an organic diposphine oxide charge transporting layer*. Appl. Phys. Lett. **88** (2006), 183503.
- [124] R. J. Holmes, B. W. D'Andrade, S. R. Forrest, X. Ren, J. Li, M. E. Thompson: *Efficient, deep-blue organic electrophosphorescence by guest charge trapping*. Appl. Phys. Lett. **83** (2003), 3818.
- [125] S.-J. Yeh, M.-F. Wu, C.-T. Chen, Y.-H. Song, Y. Chi, M.-H. Ho, S.-F. Hsu, C. H. Chen: *New dopant and host materials for blue-light-emitting phosphorescent organic electroluminescent devices*. Adv. Mater. **17** (2005), 285.
- [126] C. Schildknecht: Carben Emitter in OLEDs. Dissertation, Fakultät für Elektrotechnik und Informationstechnik, TU Braunschweig, 2006.

- [127] X. Zhou, D. S. Qin, M. Pfeiffer, J. Blochwitz-Nimoth, A. Werner, J. Drechsel, B. Maennig, K. Leo, M. Bold, P. Erk, H. Hartmann: *High-efficiency electrophosphorescent organic light-emitting diodes with double light-emitting layers*. Appl. Phys. Lett. **81** (2002), 4070.
- [128] M. Cocchi, D. Virgili, G. Giro, V. Fattori, P. D. Marco, J. Kalinowski, Y. Shirota: *Efficient exciplex emitting organic electroluminescent devices*. Appl. Phys. Lett. **80** (2002), 2401.
- [129] C. Giebeler, H. Antoniadis, D. D. C. Bradley, Y. Shirota: *Influence of the hole transporting layer on the performance of organic light-emitting diodes*. J. Appl. Phys. **85** (1999), 608.
- [130] K. Itano, H. Ogawa, Y. Shirota: *Exciplex formation at the organic solid-state interface: Yellow emission in organic light-emitting diodes using green-fluorescent tris(8-quinolato)aluminum and hole-transporting molecular materials with low ionization potentials*. Appl. Phys. Lett. **72** (1998), 636.
- [131] J. Blochwitz, M. Pfeiffer, M. Hoffmann, K. Leo: *Non-polymeric oleds with a doped amorphous hole transport layer and operating voltages down to 3.2 v to achieve 100 cd/m²*. Synt. Met. **127** (2002), 169.
- [132] J. Kalinowski, W. Stampor, J. Mezyk, M. Cocchi, D. Virgili, V. Fattori, P. D. Marco: *Quenching effects in organic electrophosphorescence*. Phys. Rev. B **66** (2002), 235321.
- [133] L. H. Smith, J. A. E. Wasey, W. L. Barnes: *Light outcoupling efficiency of top-emitting organic light-emitting diodes*. Appl. Phys. Lett. **84** (2004), 2986.
- [134] H. Kanno, N. C. Giebink, Y. Sun, S. R. Forrest: *Stacked white organic light-emitting devices based on a combination of fluorescent and phosphorescent emitters*. Appl. Phys. Lett. **89** (2006), 023502.
- [135] C.-C. Chang, J.-F. Chen, S.-W. Hwang, C. H. Chen: *Highly efficient white organic electroluminescent devices based on tandem architecture*. Appl. Phys. Lett. **87** (2005), 253501.
- [136] F. Guo, D. Ma: *White organic light-emitting diodes based on tandem structures*. Appl. Phys. Lett. **87** (2005), 173510.
- [137] T. Tsutsui, M. Terai: *Electric field-assisted bipolar charge spouting in organic thin-film diodes*. Appl. Phys. Lett. **84** (2004), 440.
- [138] M. Terai, K. Fujita, T. Tsutsui: *Capacitance measurement in organic thin-film device with internal charge separation zone*. Jpn. J. Appl. Phys. **44** (2005), L1059.

-
- [139] T.-Y. Cho, C.-L. Lin, C.-C. Wu: *Microcavity two-unit tandem organic light-emitting devices having a high efficiency*. Appl. Phys. Lett. **88** (2006), 111106.
- [140] L. S. Liao, K. P. Klubek, C. W. Tang: *High-efficiency tandem organic light-emitting diodes*. Appl. Phys. Lett. **84** (2004), 167.
- [141] C. W. Law, K. M. Lau, M. K. Fung, M. Y. Chan, F. L. Wong, C. S. Lee, S. T. Lee: *Effective organic-based connection unit for stacked organic light-emitting devices*. Appl. Phys. Lett. **89** (2006), 133511.
- [142] Y. Park, V. Choong, Y. Gao, B. R. Hsieh, C. W. Tang: *Work function of indium tin oxide transparent conductor measured by photoelectron spectroscopy*. Appl. Phys. Lett. **68** (1996), 2699.
- [143] A. Kahn, W. Zhao, W. Gao, H. Vasquez, F. Flores: *Doping-induced realignment of molecular levels at organic-organic heterojunctions*. Chem. Phys. **325** (2006), 129.
- [144] E. Ito, Y. Wahizu, N. Hayashi, H. Ishii, N. Matsuie, K. Tsuboi, Y. Ouchi, Y. Harima, K. Yamashita, K. Seki: *Spontaneous buildup of giant surface potential by vacuum deposition of alq_3 and its removal by visible light irradiation*. J. Appl. Phys. **92** (2002), 7306.
- [145] D. R. Lide: Handbook of Chemistry and Physics. Boca Ranton: CRC Press 2000.
- [146] L. Yan, N. J. Watkins, S. Zorba, Y. Gao, C. W. Tang: *Direct observation of fermi-level pinning in cs -doped $cupc$ film*. Appl. Phys. Lett. **79** (2001), 4148.
- [147] K. L. Chopra, S. Major, D. K. Pandya: *Transparent conductors - a status review*. Thin Solid Films **102** (1983), 1.
- [148] B.-W. Lee, P. Kunjal, J.-M. Huh, J. Chung, C. Chu, K. Chung: *Large size am -oled technology*. EL 2006, 2006, 30.
- [149] M. Bender, A. Klöppel, U. Hoffmann: *Prozesstechnologien für die großflächige abscheidung von ito -schichten bei niedrigen temperaturen*. FVS Workshop 2002, 2002, 77.
- [150] D. Mergel: *Thin films of ito as conductive, transparent electrodes*. Vakuum in Forschung und Praxis **16** (2004), 58.
- [151] M. Pfeiffer, S. R. Forrest, X. Zhou, K. Leo: *A low drive voltage, transparent, metal-free n - i - p electrophosphorescent light emitting diode*. Organic Electronics **4** (2003), 21.
- [152] H. Chen, C. Qiu, M. Wong, H. S. Kwok: *Dc sputtered indium-tin oxide transparent cathode for organic light-emitting diode*. IEEE Elect. Dev. Let. **24** (2003), 315.

- [153] H.-K. Kim, D.-G. Kim, K.-S. Lee, M.-S. Huh, S. H. Jeong, K. I. Kim, T.-Y. Seong: *Plasma damage-free sputtering of indium tin oxide cathode layers for top-emitting organic light-emitting diodes*. Appl. Phys. Lett. **86** (2005), 183503.
- [154] L. J. van der Pauw: *A method of measuring the specific resistivity and hall effect of discs of arbitrary shape*. Philips Res. Repts. 13 **13** (1958), 1.
- [155] M. Bender, J. Trube, J. Stollenwerk: *Characterization of a rf/dc-magnetron discharge for the sputter deposition of transparent and highly conductive ito films*. Appl. Phys. A **69** (1999), 397.
- [156] D. Mergel, W. Stass, G. Ehl, D. Barthel: *Oxygen incorporation in thin films of $\text{In}_2\text{O}_3:\text{Sn}$ prepared by radio frequency sputtering*. J. Appl. Phys. **88** (2000), 2437.
- [157] R. Mientus, K. Ellmer: *Reactive magnetron sputtering of tin-doped indium oxide (ito): influence of argon pressure and plasma excitation mode*. Surface and Coatings Technology **142-144** (2001), 748.
- [158] G. Frank, H. Köstlin: *Electrical properties and defect model*. Appl. Phys. A **27** (1982), 197.
- [159] M. Bender, W. Seelig, C. Daube, H. Frankenberger, B. Ocker, J. Stollenwerk: *Dependence of film composition and thicknesses on optical and electrical properties of ito-metal-ito multilayers*. Thin Solid Films **326** (1998b), 67.
- [160] K. H. Choi, J. Y. Kim, Y. S. Lee, H. J. Kim: *Ito/ag/ito multilayer films for the application of a very low resistance transparent electrode*. Thin Solid Films **341** (1999), 152.
- [161] R. Hartmann, P. Chow, M. Shibata: *Novel co-evaporation source for large area oled panel manufacturing*. SID 2005 digest, 2005, 1899.
- [162] C. H. C. Hwang: *How to make the 5th generation amoled*. Proc. EL2006, 2006, 421.
- [163] V. Bulovic, R. Deshpande, M. E. Thompson, S. R. Forrest: *Tuning the color emission of thin film molecular organic light emitting devices by the solid state solvation effect*. Chem. Phys. Lett. **308** (1999), 317.
- [164] U. Hoffmann: private communication.
- [165] S. T. Lee, J. Y. Lee, M. H. Kim, M. C. Suh, T. M. Kang, Y. J. Choi, J. Y. Park, J. H. Kwon, H. K. Chung, J. Baetzold, E. Bellmann, V. Savvateev, M. Wolk, S. Webster: *A new patterning method for full-color polymer light-emitting devices: Laser induced thermal imaging (liti)*. SID 2002 digest, 2002, 784.

-
- [166] B. D. Chin, M. C. Suh, M. H. Kim, T. M. Kang, N. C. Yang, M. W. Song, S. T. Lee, J. H. Kwon, H. K. Chung, M. B. Wolk, E. Bellmann, J. P. Baetzold: *High efficiency amoled using hybrid of small molecule and polymer materials patterned by laser transfer*. J. Inform. Display **4** (2003).
- [167] M. Shtein, P. Peumans, J. B. Benziger, S. R. Forrest: *Direct, mask- and solvent-free printing of molecular organic semiconductors*. Adv. Mater. **16** (2004), 1615.
- [168] E. Becker, T. Riedl, T. Dobbertin, D. Schneider, D. Heithecker, D. Metzdorf, H.-H. Johannes, W. Kowalsky: *Spatially selective flash sublimation of small organic molecules for organic light-emitting diodes and display applications*. Appl. Phys. Lett. **82** (2003), 2712–2714.
- [169] E. Fogarassy: *Basic mechanisms and application of the laser-induced forward transfer for high-*tc* superconducting thin film deposition*. Bd. 1394 von *Proc. of SPIE*, 1990, 169.
- [170] T. S. Z. Toth, A. L. Toth: *Ar⁺ laser-induced forward transfer (lift): a novel method for micrometer-size surface patterning*. Applied Surface Science **69** (1993), 317.
- [171] Z. Kanthor, Z. Toth, T. Szörenyi, A. L. Toth: *Deposition of micrometer-sized tungsten patterns by laser transfer technique*. Appl. Phys. Lett. **64** (1994), 3506.
- [172] I. Zergioti, S. Mailis, N. Vainos, P. Papakonstantinou, C. Kalpouzos, C. Grigoropoulos, C. Fotakis: *Microdeposition of metal and oxide structures using ultrashort laser pulses*. Appl. Phys. A **66** (1998), 579.
- [173] E. Becker, D. Heithecker, D. Metzdorf, H.-H. Johannes, T. Dobbertin, D. Schneider, W. Kowalsky: *Verfahren zur mikrostrukturierung mittels ortsselektiver sublimation*. Patent DE 102 46 425 A1, Deutsches Patent- und Markenamt, 2004.
- [174] W. Sarfert: *Laserstrukturierung der Kathode organischer Displays*. Aachen: Shaker 2006.
- [175] P. B. Johnson, R. W. Christy: *Optical constants of transition metals: Ti, v, cr, mn, fe, co, ni, and pd*. Phys. Rev. B **9** (1974), 5056.
- [176] B. M. Clemens, G. L. Eesley, C. A. Paddock: *Time-resolved thermal transport in compositionally modulated thin films*. Phys. Rev. B **37** (1988), 1085.
- [177] C. A. Paddock, G. L. Eesley: *Transient thermoreflectance from thin metal films*. J. Appl. Phys. **60** (1986), 285.
- [178] M. W. Shin, H. C. Lee, K. S. Kim, S.-H. Lee, J.-C. Kim: *Thermal analysis of tris (8-hydroxyquinoline) aluminum*. Thin Solid Films **363** (2000), 244.

-
- [179] W. J. Parker, R. J. Jenkins, C. P. Butler, G. L. Abbott: *Flash method of determining thermal diffusivity, heat capacity, and thermal conductivity*. J. Appl. Phys. **32** (1961), 1679.
 - [180] G. Yang, A. D. Migone, K. W. Johnson: *Heat capacity and thermal diffusivity of a glass sample*. Phys. Rev. B **45** (1992), 157.
 - [181] The coherent interferometry measurements were performed by Dipl.-Ing. Gabor Molnar, Institute of Production Measurement Technology, Technical University Brunswick.
 - [182] M. Kröger, T. Dobbertin, D. Schneider, T. Rabe, E. Becker, H.-H. Johannes, W. Kowalsky: *Highly efficient guest-host-systems for hybrid inverted organic light-emitting diodes with sputtered indium-tin-oxide anodes*. Proc. SPIE **5519** (2004), 143.
 - [183] D. Ma, C. S. Lee, S. T. Lee, L. S. Hung: *Improved efficiency by a graded emissive region in organic light-emitting diodes*. Appl. Phys. Lett. **80** (2002), 3641.
 - [184] A. B. Chwang, R. C. Kwong, J. Brown: *Graded mixed-layer organic light-emitting devices*. Appl. Phys. Lett. **80** (2002), 725.

